2016

NANOSPHERE LITHOGRAPHY AND ITS APPLICATION IN RAPID AND ECONOMIC FABRICATION OF PLASMONIC HYDROGENATED AMORPHOUS SILICON PHOTOVOLTAIC DEVICES

Chenlong Zhang
Michigan Technological University, czhang15@mtu.edu

NANOSPHERE LITHOGRAPHY AND ITS APPLICATION IN RAPID AND ECONOMIC FABRICATION OF PLASMONIC HYDROGENATED AMORPHOUS SILICON PHOTOVOLTAIC DEVICES

By

Chenlong Zhang

A DISSERTATION

Submitted in partial fulfillment of the requirements for the degree of

DOCTOR OF PHILOSOPHY

In Materials Science and Engineering

MICHIGAN TECHNOLOGICAL UNIVERSITY

2016

This dissertation has been approved in partial fulfillment of the requirements for the Degree of DOCTOR OF PHILOSOPHY in Materials Science and Engineering.

Department of Materials Science and Engineering

Dissertation Advisor: *Joshua M. Pearce*

Committee Member: *Yun Hang Hu*

Committee Member: *Paul L. Bergstrom*

Committee Member: *Stephen Hackney*

Department Chair: *Stephen L. Kampe*

To my beloved mother and father

Table of contents

Preface

This dissertation is a manuscript based thesis comprised of three core publications submitted for review. The author's contributions are described hereafter.

Chapter two is submitted as "Chenlong Zhang, Sandra Cvetanovic, Joshua M. Pearce, "Fabrication ordered 2-D nano-structured arrays using microsphere nanosphere lithography". C. Zhang was responsible for all the literature review, experiment design, data collection and analysis, and article writing. S. Cvetanovic helped with interface coating, data collection and editing. J. M. Pearce contributed on experimental design, writing, editing and consultation.

Chapter three is submitted as "C. Zhang, D. O. Guney and J. M. Pearce, "Leveraging plasmonic enhancement on amorphous silicon solar photovoltaic with hexagonal silver arrays". C. Zhang was responsible for composing the hypothesis, establishing the numerical simulation model, analyzing the simulation results and writing the paper. D. O. Guney contributed on theoretical consultation, modeling guidance and mode analysis and editing. J M Pearce contributed on writing, consultation and editing.

Chapter four is submitted as "C. Zhang, Jephias Gwamuri, Sandra Cvetanovic, J. D. O. Guney , J. M. Pearce."Enhancement of Hydrogenated Amorphous Silicon Solar Cells with Front-Surface Hexagonal Plasmonic Arrays from Nanoscale Lithography" C. Zhang was responsible for the simulation and conceived and conduced the experiment and wrote the paper. J. Gwamuri fabricated the cells and edited the paper. S. Cvetanovic helped with interface coating, data collection. D. O. Guney contributed on theoretical consultation, modeling guidance and mode analysis and editing. J. M. Pearce contributed on experimental design, writing, editing and consultation.

Abstract

Solar photovoltaic (PV) devices harvest energy from solar radiation and convert it to electricity. PV technologies, as an alternative to traditional fossil fuels, use clean and renewable energy while minimizing pollution. For decades researchers have been developing thin film solar cells as an important alternatives to the relatively expensive bulk crystal solar cell technology. Among those, hydrogenated amorphous silicon (a-Si:H) solar cells prevails for good efficiency, non-toxic and materially abundant nature. However, a-Si:H thickness must be minimized to prevent light induced degradation, so optical enhancement is necessary. Light manipulation has to be applied and carefully engineered to trap light within the active layer(s) of the cell using an inexpensive processing techniques. Plasmonic nanostructure allows manipulation of light to be fine-tuned at nanoscale by enabling plasmonic induced scattering, near-field effect and supported surface plasmon plariton (SPP). However traditional fabrication techniques for fabricating nanoscale plasmonic structure are expensive and cumbersome. In this research studies have been conducted to explore the inexpensive fabrication technologies. As a result, nanosphere lithography (NSL) is chosen as a masking material to create scalable plasmonic nanoparticles at low cost. With computer aided design and numerical simulation, the physics behind plasmonic resonance and cell performance is revealed and the geometry and parameters of plasmonic nanostructure are optimized. Finally, a proof-of-concept study has been made to show the effective enhancement in a-Si:H using plasmonic nanostructures fabricate with NSL. The research indicates the feasibility of using the proposed method for commercializing plasmonic a-Si:H solar cells.

Chapter 1: Introduction

1.1. Motivation and hypothesis

The growing PV market demand high performance solar cells at lower cost. C-Si silicon solar cells are fundamentally limited on cost and performance by a single bandgap indirect semiconductor material. High efficiency multijunction and concentrator cells are too expensive that they haven't been embraced by the industry. Thin film solar cell, on the other hand, drastically reduces the material cost by using abundant, cheap and easy-to-fabricate material such as hydrogenate amorphous silicon (a-Si:H). To avoid the poor absorption profile of a-Si:H cells in the long wavelength region, and to compensate the loss caused by light-induced degradation, the optical path length must be increased within the absorbing layer. Plasmonic structures in nanoscale provides sophisticated manipulation of light as well as helps solves anti-reflection coating and texturing problem, which cannot be simply copy-paste from conventional solution. A number of published articles proves the efficiency enhancement achieved with plasmonic structure can boost the efficiency to a new record, and the record keeps updating as new plasmonic structures are proposed. However, implementation of plasmonic structure requires further investigation in advanced equipment and development of complex operating protocols, which all together add tremendous burden to commercialization. Nanosphere lithography (NSL), also known as natural lithography, frees the prerequisites of equipment, trained professionals and long term development. For plasmonic application, nanoscale patterning can be accomplished in minutes by people with zero knowledge on nanofabrication. However, plasmonic effect can be either beneficial or harmful depending on the environment, pattern and particle geometry and size. The physics behind has not been clearly understand and whether NSL can provide useful enhancement is not concluded.

The goal of this research is to explore the inexpensive approaches to further drive down the cost per watt for the PV market. The selected direction is to implement plasmonic

structure in a-Si:H solar cell by NSL. The study will not only focus on experimental implementation of the patterned plasmonic nanostructure, but will also theoretically explain the underlying physics that supports the plasmonic effect, explore possible configurations to maximize enhancement and make predictions for a diverse size and geometry using the NSL and a-Si:H cells. To accomplish the objective the following two hypothesis are proposed:

Hypothesis #1

Uniform periodic nanosphere monolayer with over 90 percent coverage can be fabricated by adjusting the physical properties of nanospheres, experimental approaches and fabrication strategies.

Hypothesis #2

Silver nanoparticles deposited on top of front contact can couple the scattered field into absorbing i-layer, resulting in increased enhancement and improved photocurrent.

1.2. Outline of the dissertation

The dissertation has five main chapters. In this first Chapter, the background knowledge and development of plasmonic thin film solar cell, as well as nanosphere lithography are introduced. The motivation and hypothesis of this study are composed. The skeleton of this dissertation is summarized. In the second Chapter, the first hypothesis is addressed by a series of experiments. Two main coating methodologies are proposed to fabricate uniform nanosphere monolayer. The effect of bead size, spin coating speed, beads suspension concentration, angled interface coating and influence of surfactant are discussed. In the third Chapter, the plasmonic solar cell is modeled numerically in simulation software with packages. Theoretical analysis is conducted to clarify the physics behind the plasmonic effect with particular pattern fabricated by NSL. The result is optimized by nanosphere size, silver film thickness, silver particle

size and geometry. The fourth Chapter concentrates on implementing the simulated structure. Various characterization techniques are used to validate the consistence between simulation and experiment. The fabricated solar cell is tested and measured to provide contract to modeled result. Discrepancies are discussed in detail. In the final Chapter, the conclusions are drawn on the aggregate of the results and future work are summarized.

1.3. Photovoltaic and solar cell background

Photovoltaic (PV) devices, also known as solar cells, are a set of electrical devices that convert energy of light into electricity. A typical PV devices is a semiconductor p-n junction, where incoming light is absorbed by the semiconductor to excite its electrons over the gap from valence band to conductive band. As a result, electron-hole pairs are generated as free carriers, and these carriers move toward the electrodes by diffusion and drifting. The separated carriers are collected at the electrodes therefore a potential gradient is created across the cell. The cell behaves as a normal battery and outputs power to wired devices. Solar cells are easily scaled up by bundling a batch of cells into a solar module, and modules can be collected into an array to directly power DC devices or be converted to AC to be incorporated into the grid. The first commercialized solar cell is a crystalline silicon p-n junction cell, developed in 1954 at Bell Laboratories[1]. At the early stage investigation in PV industry is rare, because of the high cost of available high quality silicon. Solar cells only found applications in space as satellites power panels. Starting from the late 1960s, the semiconductor industry blooms worldwide, as the large scale integrated circuit pushed demand in high-quality silicon wafers. This lays the foundation of the development in PV industry. In 1970s, Elliot Berman simplified the processing by replacing antireflection coating layer with roughened silicon surface, using integrated circuit board instead hand-wired circuit. His series improvement significantly reduced the price per watt, However, the cost is still too high to allow consumer level massive production. As the semiconductor industry grew into an ever-larger scale, cheap silicon waste and old

equipment went to PV industry at extremely low cost. PV modules price started to collapse in the early 1980s and today it still continuously declining.

The PV industry enjoys a global investigation and massive installation in the new century. The worldwide photovoltaic market grows exponentially for more decades. According to Solar Power Europe (SPE) the global PV installation in 2015 is 233,000 megawatts (MW) [2], twice the amount of 2013 and 6 times greater the amount in 2010. In over 30 countries the grid parity has been reached by end of 2014[3]. By the time of this dissertation is written, over 40 countries planned to install more than 100 MW in the year. A global short-term projection by International Energy Agency (IEA) and SPE predicts the worldwide deployment reach 400 gigawatts (GW) in 2020[4]. More than 5 countries (states) will be able to have over 10 percent of its annual power generation provided by solar energy.

Nowadays over 90 percent of the solar panels are crystal silicon (c-Si) based. Modern crystalline silicon solar cell can reach to 25 percent conversion efficiency, surpassing all major competitors except multijunction or concentrator cells. Classic c-Si solar cells are based on a silicon p-n junction. Due to the indirect bandgap nature, c-Si solar cell must be designed to have a large thickness to allow light at long wavelength to not escape the cell and to allow the separated electron-hole pairs to diffuse to and be collected at electrodes. The typical thickness of a c-Si solar cell is around 300μm, and more than 40 percent of the cell's cost comes from the thick silicon wafer. This plagues the cell as the price for crystalline silicon is heavily reliant on the semiconductor market. An alternative way to further drive down PV module cost is to attenuate the material while maintaining the efficiency. This is where researcher start to design, develop and engineer the thin film solar cells.

Thin film solar cells are advantageous over c-Si solar cell for 1) the drastic reduction of semiconductor material cost by thinning the cell from hundreds of microns to hundreds nanometers; 2) fabrication can be easily scaled up on inexpensive substrates such as glass and plastics; 3) the flexibility to fabricate cell on soft materials enabling folding or installing cells in textured surfaces. Thin film cells have the potential to drive down

the cost of PV module of well below $1 per watt. The physics behind this cost reduction is that most of the thin film solar cells are direct bandgap solar cells. Unlike c-Si solar cells, which are an indirect bandgap solar cells, the valence-conduction band transition does not need the assistance of phonon to have matched momentum, therefore the optical absorption constant of direct bandgap material much larger, which in turn allow them to absorb most of the light within a very shallow thickess. For instance, amorphous silicon solar cells can achieve full spectrum absorption within 1μm, the equivalent thickness in c-Si cell is approaching 1mm. Thin film solar cell have been researching and developing for about 30 years. The prevailing candidates of thin film solar cell materials are amorphous silicon, cadmium telluride (CdTe) and copper indium diselenide (CIS) , while amorphous silicon solar cells uses earth-abundant, non-toxic elements hence has received the most research attentions[5,6].

The amorphous silicon thin film is a material without long range atomic order. The defect density of the material is of order of 10^{19} cm^{-3}. Such high defect density is caused by silicon atoms that possess dangling bonds with unpaired electrons, those defects are highly active and act as recombination center to greatly reduce carrier life time. Thanks to the emergence of plasma-enhanced chemical vapor deposition (PECVD), amorphous silicon can be incorporated with about 10 percent hydrogen, which drastically reduces the defect density to about 10^{16} cm^{-3}, and allows the material to be doped in p-type or n-type to be useful as a semiconductor device. Hydrogenated amorphous silicon (a-Si:H) solar cells appeared in the early 1980s, fabricated under 200 °C in PECVD system. a-Si:H solar cells have the advantages over c-Si cells, however, only possesses a stable market share of about 6 percent[7]. This is primarily because of the relatively poor cell performance of only 10 percent conversion efficiency. The highest stable conversion efficiency reported is 13.6 percent achieved by LG Electronics in 2013. In addition to the low conversion efficiency, a-Si:H suffers from a light induced degradation generally known as “Staebler-Wronski effect” (SWE)[8–10]. The degradation drops off about 10 to 30 percent of the cell efficiency after a prolonged exposure to sunlight until reaching a degraded steady state. The

physics behind SWE is still unclear but very likely bonded to metastable states inside a-Si:H[11–15]. SWE is completely reversible upon annealing at 150 °C or above, however, under intense (50 suns) illumination the process become irreversible[16].

Amorphous silicon has a bandgap of 1.7eV, making it a good very broad range absorber. Amorphous silicon absorbs from near infrared to ultraviolet and very responsive to weak light. Typical junction configuration for a-Si:H solar cell is a p-i-n junction type. Due to the high defect density, a-Si:H is not a good conductor to support diffusion based charge separation. A p-i-n configuration assists the separation by drifting along the built-in electric field across the intrinsic layer, which turns out to be more efficient than diffusion in a-Si:H cells. Opposite to c-Si, the p-type is put on top to receive the sunlight, so that holes with low mobility can be effectively collected, while electrons can survive a long range drifting to reach the n-type and be collected there.

Due to the very limited thickness of thin film solar cell. Light may not be effectively absorbed within a few hundred nanometers. Moreover, the a-Si:H absorption coefficient as a function of photo energy, is much smaller in the red part compared to it in the blue part of the spectrum. For instance, the absorption coefficient of a-Si:H at 350nm is three orders of magnitude larger than that at 700nm[17], and consequently, the absorption depth at long wavelength is much longer. The high defect density and low diffusion length limit a-Si:H thickness to be within a couple hundred nanometer[18–21] to be electrically optimum. Therefore light trapping is the necessary for thin film PV devices. Light trapping is the concept of engineering cell structure to manipulate light propagation within the cell's active material. The goal is to increase the light optical path length so that photons have a larger chance to be absorbed before they escape the cell. A variety of trapping schemes have been studied and reported in the last two decades[22,23]. The most common approach is to duplicate the antireflection (AR) coating from c-Si solar cells to thin film cells, which in most cases is comprised of a pyramidal surface texture. However, roughening and texturing of thin film cell surfaces is not feasible to reach a useful micron-scale, as they demand pitches

with depth exceeding the cell thickness. In addition, surface roughness increase the recombination sites. Instead, a textured dielectric layer, commonly seen as silicon nitride layer is used as an AR coating. Another approach involves of using a transparent flat dielectric layer. With optimization, such a layer can create destructive interference between incident and reflected light, hence perfect impedance matching is obtained. However, the mechanism only works at a specific wavelength[24]. Traditional light trapping scheme are inadequate for thin film structures, therefore novel light trapping scenarios have to be established to solve the absorption deficiencies.

1.4. Plasmonic light trapping in a-Si:H thin film solar cell

The plasmonic effects are a set of phenomena that occurs as a result of the interactions between electromagnetic waves and small particles. The discovery of plasmonic effects can be dated back to the 18th century. With the development of nanotechnology and nanofabrication, plasmonic effect and related application have been intensely studied in recent decades[25,26]. The interactions between metal surface and the incoming electromagnetic waves can be generalized into two categories: 1) the surface plasmon polariton (SPP) and 2) the localized surface plasmon resonance (LSPR). The former is a non-radiative electromagnetic waves propagating along the metal/medium interface. To meet the requirements that allows SPP to exist, the real part of the dielectric constants of the metal must be negative whilst for the medium it has to be positive. The condition is met for most metal in the infrared/visible region of the electromagnetic spectrum in air or water. LSPR, on the other hand, is a collective oscillations of free electrons induced by light. The resonance is confined within several nanometers away from the metal surface. At resonant frequency the LSPR can enhance the near-field amplitude to be many times higher than the field of incident light, but the field decays exponentially with the distance away from the metal surface. Such significant enhancement of localized electric field provides high spatial resolutions that is critical in many applications. It is well known that both the SPP and LSPR are highly sensitive to the change of geometry and size of the metal particle as well as the surrounding

environment. A great amount of work has been done in plasmonics in enhanced Raman spectroscopy[27], biosensing[28], cancer therapy[29], drug deliver[30] and PV applications[31–33]. Plasmonic effects can also be taken as a new approach to trap light inside the cell. Compared to traditional light trapping scheme, plasmonic structure have two main advantages:

1) the nanoparticles used to excite plasmonic resonance is of subwavelength sizes, which means the absorber needs not to rely on thick pyramidal antireflection coatings;

2) plasmonic structures support multiple ways to light trapping including scattering, nearfield coupling, waveguide mode, Fabry-Perot cavity, and diffraction -- all of which can be optimized to maximize the enhancement.

1.4.1. Light scattering from metallic nanoparticles

Light scattering is a physical process where light is deviated from its original path trajectory by the interaction with the non-uniformities in the medium through which it passes[34]. After the establishment of Maxwell's Equation, the physics behind light scattering can be mathematically resolved. In 1871, Lord Rayleigh introduced the electric dipole model that explains light scattering by small molecules. The model attributes the scattering is a result of light induced polarization process. The theory is further developed and extended by Mie, and is applied to all spherical objects with comparable or larger size of the wavelength of incoming light. The combined solution by Lord Rayleigh and Mie provides fundamental understanding of some common yet interesting problems, such as the origin of skylight, color of the rainbow and origin of solar corona[35].

Two important quantities introduced by Mie's approximation is the scattering and absorption cross-section, defined as the ratio of scattered and absorbed power per square meter to the power of incident light. For dipole moment it can be expressed as

$$\sigma_{sca} = \sigma_{geom} Q_{sca} = \sigma_{geom} \times \frac{8}{3} q^4 \left| \frac{\frac{\epsilon_p}{\epsilon_m} - 1}{\frac{\epsilon_p}{\epsilon_m} + 2} \right|^2 \quad (1.2.1)$$

$$\sigma_{abs} = \sigma_{geom} Q_{abs} = \sigma_{geom} \times 4q\mathrm{Im}\left[\frac{\frac{\epsilon_p}{\varepsilon_m}-1}{\frac{\varepsilon_p}{\epsilon_m}+2}\right] \quad (1.2.2)$$

Where σ_{geom} is the geometrical cross-section, for sphere, the value is equal to πa^2, a is the radius of the sphere. The dimensionless value Q_{sca} and Q_{abs} are the Q factor of scattering and absorption cross-section respectively, where$q = ka$, ε_p and ε_m is the dielectric function of particle and medium respectively. k is the wave vector of the medium.

The cross-section equations imply two things intuitively. First, the scattering cross-section is sensitive to the change of the particle size. Given the medium in which the particle is embedded, the cross-section increase with particle size while scattering cross-section grows faster than absorption cross-section. Second, the resonance occurs when dielectric function of particle is twice the value of the medium's, in the opposite sign, specifically $\varepsilon_p = -2\varepsilon_m$. At the resonance both cross-section become many times of the particle's geometrical size, leading to extraordinary scattering and absorption of incoming photons. This is the origin of surface plasmon resonance (SPR). As can be inferred from the equations, the resonance peak is sensitive to the change of the size of the particle, the dielectric function of the medium. The size effect is can be explained from two aspects. First, increasing the geometry size will weaken the restoring force, which is generated by separated charges at the surface of the particle, to depolarize the particle. Clearly, the longer the distance between the charged surface, the weaker their interaction. As a consequence, the resonance peak shifts red. On the other hand, the distribution of polarized field is affected by size, hence the resonance as well. According to Mie's theory, the cross-section is the sum of all possible resonance in all possible format. i.e.

$$Q_{sca} = Q_{sca}(l) = \sum_l^n Q_{sca}^l \quad (1.2.3)$$

Where l is the order of the SPR. Higher order resonance, it is often found in larger particles, which is in comparable size to the wavelength of incoming light. High order resonance, just like dipole resonance, can be engineered to favor for PV applications.

Matheu and his co-workers spread gold and silica nanoparticle onto c-Si solar cell, and obtained up to 3% and 9% enhancement for gold nanoparticle (diameter = 100nm) and silica nanoparticle (diameter = 150nm) respectively[36]. In their later work, the numerical simulation shows the enhancement comes from the top scatterers which couple the light into the silicon body at 500-1000nm region. The total increased conversion efficiency observed from experiment is about 8.8%[37].

The general configuration of scattered enhanced cell uses a top contact scenario, in which the scatter is deposited, spread or patterned on top of cell, usually on or in the transparent conducting oxides (TCO). Unlike scattering from particle suspended in homogeneous medium, scattering from particle on substrates preferentially direct the light into the dielectric with larger reflective index[38]. The angular distribution acquired through scattering leads to increased optical path length. In addition to the increased optical path length, light scattered at an angle exceeds the critical angle of the medium are subjected to total internal reflection, in that case the scattered light may never escape from the material. Furthermore, when the scattered light is reflected back from the back contactor, it has a chance to interact with the particle again, a secondary scattering process may occur, resulting the light reentering the dielectric medium. In sum, the overall reflectance is dramatically minimized by scattering. This makes the scattering favors PV applications as most of the conducting oxides have larger refractive index, especially for thin film solar cells where light trapping is critically demanded. Catchpole et al. summarize the previous work and proposed design principles for plasmonic solar cells through scattering[39]. Particle material, shape, size and dielectric spacing have been systematically analyzed and discussed. Particles made of silver is considered to be better scatterer over gold particles for its relatively small imaginary part of permittivity, which result in absorption rather than scattering[40]. For given particle size silver nanosphere can excites an enhancement near field 40 times stronger than gold[34]. Gold, on the other hand has enlarged extinction cross-section, making it good candidates for sensing[28].

Besides, the plasmonic resonance peaks for silver and gold are at 360nm and 480nm respectively, the associated absorption occurs at the same position while the scattering can happen 10-100nm longer than that resonant peak and cover a broad spectrum. For amorphous thin film solar cells the ultraviolet can hardly be utilized due to the poor material quality at the top p-layer. The major absorption happens in the i-layer peaks at 550nm, making silver advantageous over gold particles for not competing with i-layer in absorption. Well-optimized silver particles can have a scattering cross-section 10 times larger than the geometrical cross-section, and the resonance peak can be continuously tuned from 300 to 1800nm, covering a broad spectrum from ultraviolet to near infrared[38,39]. However, the plasmonic effect is a double-edged sword can theoretically improve or compromise the cell's performance. Multiple coupling between incident light and scattering light, scattering light and scattering light, scattering light and near field and scattering light and diffracted light can take place all together, making the situation extremely difficult to analyze[41–43]. Such problems are largely eased by advances in modern computational machine and the emergence of various simulation software packages[44,45]. Computed enhancement in short-circuit current through scattering can achieve 45 percent compared to cell without scatterers[46].

1.4.2. Surface plasmon polariton (SPP) and gratings.

Compared to the front contact scenarios with scatterers, the back contact scenarios are more widely adopted. Multiple light trapping schemes can be implemented by engineering the interface at dielectric/metal or metal/semiconductor. The traditional approach is to increase the roughness at the interface, so that light reach the interface experience scattering and is directed back to the semiconductor. This is widely used in many thin film solar devices and it remains a robust and easy-to-implement method for solar cell. The discovery of surface plasmon polariton (SPP) creates another approach for light trapping using back contact scenario. SPP is an electromagnetic waves propagating along the metal/semiconductor or metal/dielectric interface. The origin of

the SPP is the excitation from electron or photon (photon only for PV) with matching the momentum and frequency. In order to excite SPP the dielectric function for the two interfacing medium must be in opposite sign, which is satisfied for most metal/dielectric, metal/semiconductor interfaces. The SPP will propagate along the interface until the energy is dissipated via other mechanisms such as scattering back to the semiconductor, coupling into guided modes and/or absorbed by the semiconductor or metal. Those mechanism can be engineered in favor of PV applications. Coupling incident light into SPP requires momentum matching, which is difficult for light travel in free space because a free-space photon has less momentum due to dispersion relations[47,48]. A coupling is needed to assist momentum matching and it can be achieved by implementing a periodic structure at the interface, which adjusts the tangential component of the wave vector related to the grating period.

One of the advantages of SPP is that it turns the direction of light propagation by 90˚, this drastically increases the optical path length. A metal back contact is common for most of solar cells and the metal of chosen such Ag or Al has a plasmonic response. Hence the implementation SPP can be integrated on natural cell configuration without further introducing other material. The excited SPP frequency can be expressed by Equation 1.2.4

$$\omega_{sp} = \omega_p / \sqrt{1 + \epsilon_m} \tag{1.2.4}$$

Where, ϵ_m is the dielectric function of the medium, ω_p is the plasmonic resonant frequency of bulk material, which is around 360nm for silver. The propagation of SPP can be prolonged to 100nm into 800-1500nm spectral range[49–52]. The light that is poorly absorbed by direct incidence at longer wavelength can now be coupled into SPP and reutilized by the semiconductor. This can leads to drastically reduction in cell thickness. In a recent study lead by Giannini and co-workers, a conventional silicon cell thickness can be reduced to 100nm while maintaining the same performance as bulk cell, the study showed all the scattered light that is not initially absorbed are converted into SPP[53]. Atwater et al. demonstrate an ultra-thin amorphous silicon cell

using textured metal back reflector showing 26 percent enhancement in short-circuit current[54]. Back contact scenario is often associated with the implementation of photonic structures, which acts as both light coupler and individual scatterer/gratings. Tan et al. engineered an a-Si:H cell by incorporating Ag nanoparticles at back reflectors and observed an enhancement of J_{sc} from 13.1 mA/cm^2 for flat cell to 15.1 mA/cm^2, which is the recorded highest J_{sc} for plasmonic a-Si:H solar cell[55]. Chen et al. created a broadband back reflector by incorporating Ag nanoparticle of different sizes and obtained a 23 percent enhancement in conversion efficiency[56]. Fan et al. provide a theoretical analysis of periodic structure in optical enhancement and conclude that the actually enhancement by periodic grating can well exceed the classical $4n^2$ limit[57]. In addition, the theory is confirmed by experiments conducted in many groups[58–60]. As to how the plasmonic and grating enhanced cell compared to random textured cell, Battaglia did a series comparison using the same material and state-of-art configurations for both approaches, the observed short-circuit current reach a remarkable 17.1 mA/cm^2, undoubtedly rivals the J_{sc} in random textured cells[61].

Despite the success of the back-contact scheme, it inevitably increases the surface contact area, which in turn create more surface recombination sites as the defects increase. Therefore currently no commercialized back-contact PV is available on the market. And creating the plasmonic structure using conventional methods usually cannot be scaled up to industry level. The price for implementation is also too high for both industry and consumer.

1.4.3. Embedded plasmonic concentrators

Upon interaction with light the small nanoparticles made of silver or other noble metal can generate highly localized electric field over ten times of the magnitudes of incident field, such that the nanoparticles behave as light concentrator and nano antennas. The near field effect decays fast with the distance from the surface. To effectively harvest energy from the near field, the nanoparticle has to be placed as close to the semiconductor as possible, preferably to be embedded inside the semiconductor to

maximize the effect. This is the third scheme of plasmonic enhanced solar cell configuration. Increased photocurrent in organic solar cells, CdSe/Si heterojunction solar cells and c-Si cells have been reported[62–65]. However, the embedded structure has its own limitation. First, the particle sizes cannot be large to exceed the absorbing layer, which limits its application in thin film solar cells. Second, the absorbing material must have a high absorption rate higher than that of metal nanoparticles, otherwise the cell experience ohmic loss from inside. Third, the embedded nanoparticle must be passively coated to prevent it from diffusing into the semiconductor, however, coating the nanoparticle unavoidably creates a potential barrier for the near field. As a result only a fraction of the near field can penetrate into the semiconductor. In order to overcome the listed issue the method has to be carefully engineered to achieve enhancement.

1.5. Nanosphere lithography and applications

Nanosphere lithography (NSL) is an inexpensive, easy to implement and high throughput fabrication technique that is often used to fabrication well-ordered, periodic, large-scale 2D microstructure. NSL works on the concept of free diffusion and self-assembly, the nanospheres diffuse freely across the substrate, seeking their lowest energy configurations, and thus self-assemble into a 2D array. Methods that enable formation of 2D colloidal crystal matrices include spin coating[66], interface coating[67] and shadow coating[68]. Amongst this options, spin coating allows fine adjustment on acceleration and spin velocity hence the resultant matrix can be fabricated in a controlled manner. Interface coating approaches the second popular coating technique. Compared to spin coating, interface is insensitive to substrates hence can prepare the monolayer regardless of surface roughness, thickness and material.

Using a traditional spin coating technique to fabricate polystyrene (PS) nanosphere masks often comprise three stages. First the solvent droplets containing PS nanospheres are dropped onto a stationary substrate. Second, the spin starts and during the acceleration stage, some solvent is spun out. In the third stage, the spin speed reaches the

preset value and remains static, as the solvent evaporates, and PS nanosphere begin to self-assembly due to the capillary effect. The full substrate coverage is difficult to achieve, but depends on the concentration of beads in solvent, solvent surface tension, solvent saturation vapor pressure, and beads diameter[69]. Wafer scale monolayer coverage is a balance of art and science and thus rarely achieved, thus typical defect-free domain sizes are in the 10-100 μm^2 range. Most of the studies focused on preparation of mono- and bi-layer films with greater order degree and larger coverage. Pierre Colson and Rudi Cloots[69,70] have reported ~200 μm^2 defect-free monolayer coverage with considerable order degree. Jian Chen et al. systemically studied spin coating based large-scale colloidal crystal films self-assembly mechanism, showing that wafer-scale PS nanosphere colloidal crystal films can be obtained using nanospheres with sizes ranging from 200 nm to 1300 nm by adjusting experiment parameters such as spin speed and acceleration[70]. A recent survey on nanosphere-related publications, however, reveals that researchers who use spin coating are still randomly developing empirical protocols in spite of the theory has even been established[71,72]. This is because the conditions that the theory relies on can hardly be met in experiment. Factors such as humidity and pressure affect the result and varies from laboratory to laboratory. Colson et al. did a survey on published spin coating parameters and then try to approach the problem statistically. They established mathematic model to categorize each published data and make predictions based on the model. As a result, they claimed 200μm^2 defect free area[69]. It however must be noted, that the success of the model is built on 490 nm nanospheres and it's not been tested with other type of nanospheres.

Spin coating, though very successful in creating controllable monolayer or bi-layer colloidal mask, is high selective to the substrates. Surface properties affects the monolayer formation drastically and those properties cannot be easily sifted out or normalized in experiment. This major drawback makes spin coating works only on selected substrate with low surface roughness and high hydrophilicity. Alternatively the monolayer can be coated by interface coating, which rivals the spin coating on many

aspects, for example, it can be applied to various substrate such silicon, mica, ITO or even plastic, making it very versatile for numerous applications.

Plasmonic nanofabrication for controlled size and shape often involves using sophisticated, expensive nanolithographic equipment such as: 1) photolithography, 2) electron beam lithography, 3) focused ion beam milling, and 4) X-ray lithography and 5) NSL, often known as natural lithography, is not comparable in flexibility with traditional lithography techniques, however, wins out in simplicity, parallelism and cost. Typical nanosphere lithography yields a hexagonal close packed structure (HCP), depending on the concentration of the nanospheres in solvent it can also generate multi-stack HCP structures while mono- and bi-layer are most commonly formed with spin coating. As for as mono- and bi-layer structure are concerned, two types of plasmonic microstructures can be fabricated using NSL, with the mono-layer periodic array when plasmonic metal materials such as silver are deposited through the mask, an array of triangularly shaped nanoparticles with P_{6mm} symmetry (hexagonal lattice) is created. Increasing the concentration of the suspension leads to the formation of a colloidal crystal bi-layer mask, in which the second layer assembles onto the bottom layer, leaving a smaller hole density as to the mono-layer as half of the holes are masked by second layer nanospheres. Subsequently deposited metal particles are hexagonal shaped instead of having triangular geometry. Experimental results showed that, the more stacked the HCP structure, the more lattice defects occur. With mono-layer structures, dislocations and vacancies are two major defects, but a second layer of isolated spheres or islands can also be created.

It worth mentioning that the aperture size of the colloidal crystal mask is continuously controllable by annealing. The change in aperture size is faster as the temperature increases. Hence Kosiorek[73] suggested using microwave pulses to provide fine-tuned aperture areas from as-deposited to zero. The result can be verified by the change in diffraction viewable with a naked eye. A non-close packed colloidal crystal mask is hard to achieve due to the fact that nanospheres preferentially sit in their lowest energy configuration during the assembly process. Non-close packed PS monolayers are

fabricated using a template. However, template has to be made in-prior which increases the overall cost and complexity thus goes against the purpose of using NSL in this proposal. Agustín et al. discovered that using a modified solvent mixture, fabrication of multistack colloidal crystals in [100] and [110] orientation becomes possible[74]. They suggest that faster evaporation may lead to the non-hexagonal shape as the nanospheres as they do not have enough time to be located in their lowest energy configuration. However, the non-close packed colloidal crystal need at least three layer to achieve and the bottom layer is always close packed. A non-close packed mask fabricated with this scheme will have no holes through which the plasmonic material can be deposited onto the substrate.

NSL has been widely used in fabricating plasmonic microstructures and recently research group start to migrate the technology to PV devices. Chen et al. used a hybrid nanosphere/polymer technique and successfully fabricate plasmonic back-reflector for a-Si:H solar cell. In their work a silica nanodome is created inside each nanohole, which is then covered by silver using e-beam evaporation. 17.9% higher Jsc and 39% higher efficiency is observed against flat a-Si:H solar cell[75]. NSL plasmonic was also applied in creating a large-scale sensing array. Andreas Horrer fabricated plasmonic nanocones from combined masking of NSL and aluminum oxide. The surface-enhanced Raman spectroscopy (SERS) produced at the gold cone tip shows a factor of 10 times stronger Raman signal than flat gold surface[76]. Research on using NSL as a-Si:H superstrate absorber enhancer has not been investigated for now.

2. Fabricating Ordered 2-D Nano-Structure Array Using Nanosphere Lithography[1]

2.1. Motivation

There is substantial interest in the use of plasmonic metal nanostructures to form metamaterials for improving light absorption in thin-film solar photovoltaic (PV) devices[77]. Sophisticated light management in thin-film solar PV devices has become increasingly important in that they ensure absorption of the entire solar spectrum while reducing semiconductor absorber layer thicknesses, which in turn reduces deposition time, material use, embodied energy and greenhouse gas emissions, and economic costs[32]. This has created a demand for a scalable method of patterning large areas with metal nanostructures deposited in an ordered array. Common methods to fabricate such arrays (e.g. e-beam lithography) are expensive and not practical for such large areas. Nanosphere lithography (NSL) has been considered an alternative way of fabricating scalable plasmonic arrays[45] in an inexpensive and scalable fashion. With careful maneuver in subsequent etching and evaporation processes, geometries from simple triangle arrays to more complex structures such as rings, dots, disks, and bowls[73,75,78] can be fabricated. In the past two decades several nanosphere coating techniques have been developed to acquire nanosphere masks, including spin coating[79,80], dip coating[81,82], and interface coating[83], all aimed at attaining high order uniformity and fewer defects. Spin coating currently prevails at the lab-scale due to its high productivity and efficiency in producing self-organized particle monolayers, as well as its flexibility in controlling the process, allowing sophisticated manipulation on colloidal crystal geometry, double- or multi-layer colloidal crystals, and even non-closed packed crystals can be obtained by tuning spin coating parameters[74,84]. However, the spin coating process is not simple as it involves fine tuning several parameters, which have interdependent effects on the evaporation

[1] This chapter is submitted as "Chenlong Zhang, Sandra Cvetanovic, Joshua M. Pearce, "Fabrication ordered 2-D nano-structured arrays using microsphere nanosphere lithography" to *MethodsX* (2016)

process. Finding these parameters is a balance of art, and is largely dominated by empiricism. For researchers who want to use spin coating in their nanosphere lithography related research they often have to develop their own recipes, and generally the optimal recipe varies depending on sphere size[70].

Interface coating, also known as the Langmuir-Blodgett method, refers to the process of forming a monolayer on the liquid-air interface, which is then transferred to a solid substrate. With the assistance of surfactants[83,85], 2-D colloidal spheres self-assemble into monolayer domains. Interface coating is attractive to industry because of its insensitivity to substrate materials and relative ease of implementation. However, additional processes like surface modification are often necessary to acquire well-ordered patterns[86].

Using 500nm and 1000nm polystyrene nanospheres, the research aims at novel approach using either spin coating or interface coating to best achieve well-order, robust and large scale colloidal monolayer, which can then serves as a mask in metal deposition processes. Because plasmonic structure is extremely sensitive to the environment change, molecular residual can alter the resonance significantly[28]. The approach also puts in high priority to obtain contamination-free surface. This pushes a demand to minimize the chemical surface modification. Scanning microscope images are acquired and processed in using the free and open-source image-processing software ImageJ (https://imagej.nih.gov/ij/). Hexagonal close-packed (HCP) percentage are plotted at each methods optima. The study targets in over 90 percent monolayer coverage in order to provide high quality for deposition.

2.2. Methodology and discussion

2.2.1. Spin coating

Spin coating is a widely used, easy, and fast coating technique. Spin coating involves dropping a colloidal suspension on a hydrophilic substrate, followed by an accelerated evaporation process in a spin coater. Several parameters affect the spin coating process such as the spin velocity and acceleration, the size and concentration of the nanospheres, the substrate wettability, and ambient pressure and humidity. In applications involving the use of spin coating for nanosphere lithography, the goal is to form large-scale, well-ordered arrays. For decades, researchers have had to empirically find the best recipes for their own applications since the published recipes have so far been largely non-reproducible by others[87]. Chen et al. illustrates the mechanism of the spin coating evaporation process and develops recipes by mapping the spin speeds for various nanosphere sizes[70]. A recent survey on nanosphere-related publications, however, reveals that researchers who use spin coating are still randomly developing empirical protocols. The study is based on 500nm and 1000nm nanospheres, the optimization is performed for suspension solution contents, spin speed and nanosphere concentration. One should be noted that the study is not aimed at developing a general recipe, but instead aims to show the trend of changing parameters, and, more importantly, to compare spin coating with the alternative methodology of interface coating. This could act as a useful guideline for researches in many applications. In the end, more than 98% coverage of the close-pack hexagonal microsphere monolayer is obtained using a single step spin coating protocol.

For spin coating polystyrene nanospheres, the following steps are used:

1. A 6 inch (~154mm) silicon wafer was cut into 1 inch by 1 inch (25mm x 25mm) pieces.

2. The c-Si substrates are cleaned using a modified RCA solution (H_2O_2: NH_4OH: H_2O = 1: 1: 5) at 110 ˚C for 40 minutes. The solution oxidizes organic residuals and renders the surface hydrophilic.
3. Cleaned wafer substrates are kept in deionized water before use.
4. The substrate is dried under nitrogen flow and then transferred to the spin coater sample holder.
5. Polystyrene nanospheres 500nm and 1000nm in diameter are purchased from Fisher Scientific Inc.
6. The nanosphere suspension is centrifuged at 7500rpm for 10 minutes, which disperses the suspension into solutions with different water/ethanol ratios.
7. The solution undergoes ultrasonication for 1 hour in order to ensure that the beads in the suspension are uniformly dispersed throughout the suspension and not clumped together.
8. A 200µl nanosphere suspension is dropped onto the horizontal substrate and allowed to expand freely in order to cover the entire surface of the substrate for 2 minutes.
9. Spin coating starts with a pre-set rotation speed. The initial rotation speed is 1500 and 2000 for the 500nm and 1000nm nanospheres respectively. Spin speed varies from 1500rpm to up to 10500rpm in a series optimization experiment.
10. The rotation duration is varied from 2 to 5 minutes depending on the solvent evaporation rate.
11. Coated colloidal crystal masks are dried in air and stored in a desiccator for no more than 1 week before morphology examination.
12. The morphology analysis is carried out on JEOL S4700 field emission scanning electron microscope (FE-SEM). For the analysis, the coated silicon wafer is

sputtered to grow a 2nm thick Pd film in order to provide good conductivity and to prevent direct electron exposure that burns the polymer.

Table 2.2.1 Spin coating parameters and settings for each experiment group.

Sample #	Nanosphere diameter (nm)	Rotation Speed (RPM)	Ethanol content (% volume))	Nanosphere concentration (% wt)
A1	500	6000	0	2
A2	500	6000	0	5
A3	500	6000	0	10
A4	500	6000	0	30
B1	500	1500	0	10
B2	500	3000	0	10
B3	500	6000	0	10
B4	500	10500	0	10
C1	500	3000	30	10
C2	500	3000	50	10
C3	500	3000	70	10
C4	500	3000	100	10
D1	1000	2000	0	10
D2	1000	4000	0	10
D3	1000	6000	0	10
D4	1000	8000	0	10

First it was found that the nanosphere concentration affects the distribution and uniformity significantly. Nanosphere mono-layers can hardly form with low concentration (~2% wt). As can be seen in Figure 2.3.1 a), Sample A1 leaves about 75 percent of the surface uncovered. Nanospheres are packed in small clusters, each has 1 to about 100 spheres with irregular shapes. It is obvious the nanospheres cannot form uniform mono-layers due to insufficient concentration. Increasing the nanosphere content to 5 percent (wt) leads to a higher surface coverage of ~45 percent, as shown in Figure 2.3.1 b), small islands in A1 starts joining each other into larger domains, grain boundaries at the joint can be clearly identified in SEM images. The voids still occupies ~71 percent of the surface, hence the monolayer is far from being suitable for metal deposition. Further increasing the concentration yields improved coverage and uniformity, as an example A3 (10% wt) forms a uniform, highly ordered monolayer that can cover the entire surface, more than 95% surface area is covered with improved uniformity extends from center to boarder, no double or multilayer observed from SEM images. The primary defects found at this stage is grain boundaries, vacancies and interstitials , colloidal crystal domains ranges from 5 μm^2 to 1000 μm^2, average vacancy density is 1 per 10 μm2. At 30 percent (wt), double and multi-layer colloidal films are found almost everywhere from the center to the boarder. More interestingly, at higher concentration the top layer seems not to completely obey the rule of hexagonal orientation, instead, more than 40 percent of the top layer is square orientated, the mixed orientation is a result of quasi-stable configuration, where the top layer forms in prior to the formation of the bottom layer. Therefore the underlying foundation of HCP haven't been established at the onset of the formation of top layer, the orientation of the top layer is dictated by the lattice defects of the bottom (in this case it's huge) and the incoming nanosphere flux from the exterior, the combined forces gives rise of the mixed orientation in A4 . A charging effect shown in the SEM images may raise from multilayer spheres, the thicker the layer, the less conductive the substrate.

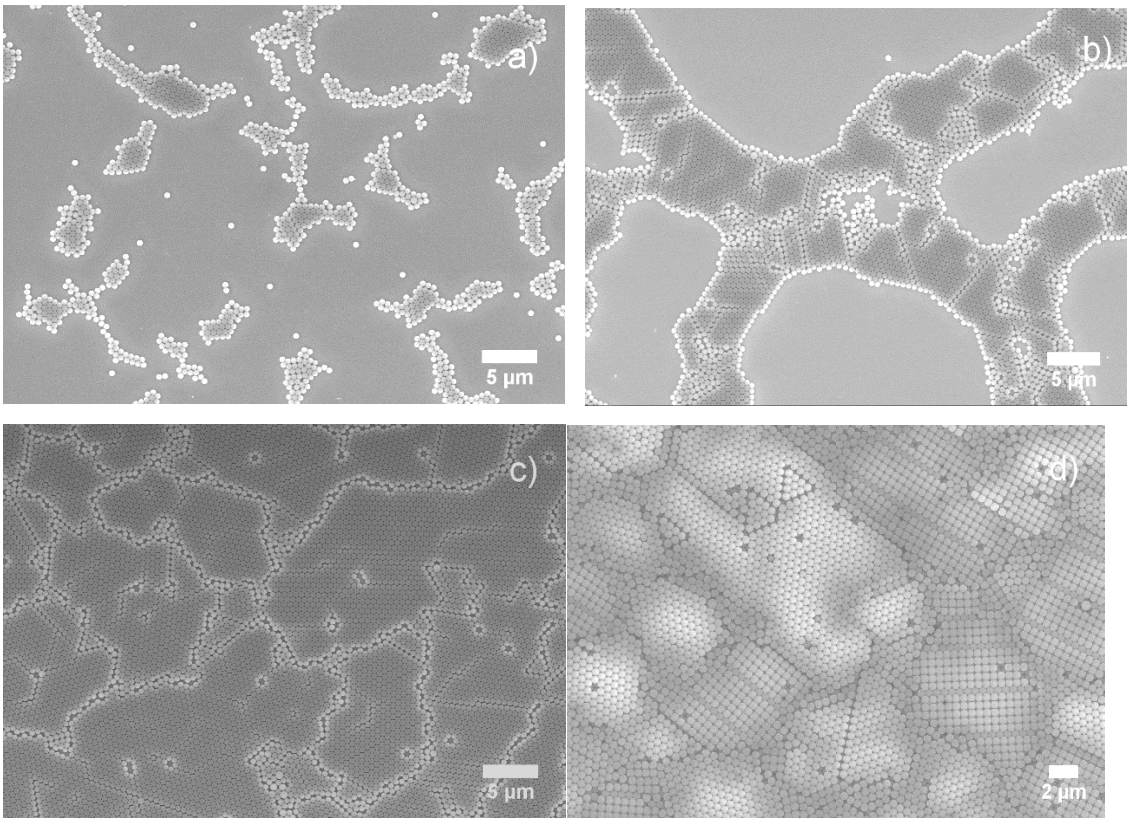

Figure 2.3.1. SEM images of polystyrene nanosphere of 500 nm in diameter spin coated on Si (100) wafer at 6000 rpm with (a) 2% wt, (b) 5% wt, (c) 10% wt and (d) 30% wt in suspension concentration, magnification = 2500

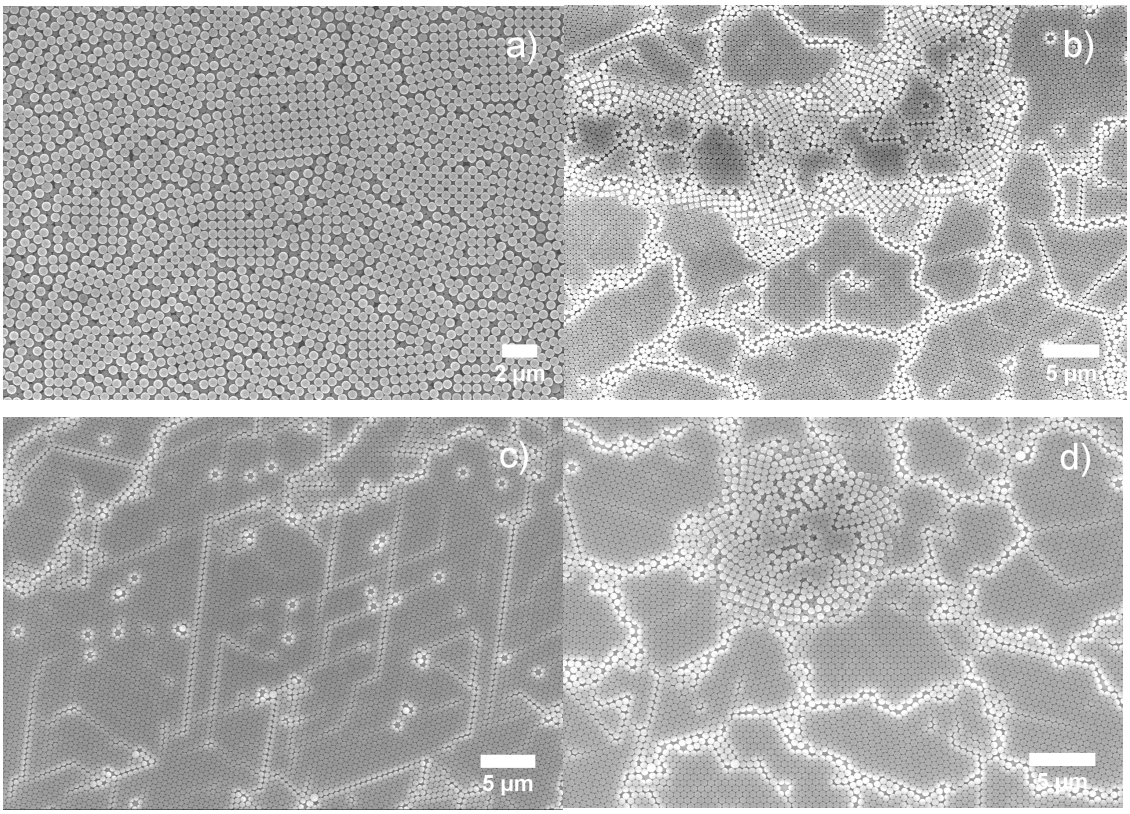

Figure. 2.3.2. SEM images of polystyrene 500 nm nanospheres in 10wt% aqueous solution spin coated on an Si (100) wafer at rotation speed = 1500 rpm (a), 3000 rpm (b), 6000 rpm (c) and 10500 rpm (d), acceleration speed = 600 rpm/s (a-d).

Spin coating on polystyrene spheres with diameters less than 500 nm has been widely studied and the recipes well established. The theoretical studies by Denkov and Zhao[71,72] show that inter-particle capillary forces are the driving forces for the ordering process. Capillary forces arise as a result of the increasing curvatures of the liquid surface between particles. As evaporation of the solvent continues, capillary forces squeeze the nanospheres into a crystal domain since the nanospheres seek the lowest energy configuration and consequently tend to maximize contact with neighbors, leading to a HCP structure. The process continues with flux from the border to compensate for the evaporated liquid, supplying more nanospheres to the domain until all the liquid has evaporated. In this way, the spheres self-assemble. When spin coating under high speeds, the suspension is spun away from the center, leaving the

central part less wet. The ordering hence starts from the center and extends towards the exterior, a phenomenon confirmed through observation of the spreading white ring from center to border during the spin coating process.

Past studies have shown that the high evaporation rate is the key to yielding high HCP coverage, which in turn requires faster spinning speeds during the spin coating process[88]. The results presented here are in agreement with these theoretical conclusions. As can be seen in Figure 2.3.2 a) and c), increasing the rotation speed minimizes the bilayer coverage and yields a more ordered HCP. At a rotation speed of 6000 rpm, the bilayer disappears, leaving the whole surface covered by the HCP. The calculated HCP coverage is ~98%, with only a tiny area at the corner uncovered. Further increasing the rotation speed does not further increase the HCP coverage – on the contrary, small bilayer clusters were observed at center of the structure. The emergence of these clusters is attributed to the rapid evaporation rate of the solvent while the radial centrifuge force is relatively weak at center. Spheres on top have therefore not yet had a chance to be spun out before the solvent evaporates. Irregularity in non-close-packed, bilayer, and multilayer structures are often found in fast evaporation systems, such as the water/ethanol system[74].

The C group focuses on variation of the solvent. By introducing ethanol the solvent become more volatile and less viscous. Figure 2.3.3 shows the SEM images acquired for ethanol content ranging from 30 to 100 percent (volume fraction). At 30 percent ethanol (C1) large bare silicon surface were found throughout center to border, average surface coverage is 47.5 percent. C2 gives a relatively uniform mono-layer covered all surface area with 400 μm^2 bi-layer domains observed at center and border, further increasing ethanol percentage leaves larger bi-layer area and interestingly, although the bottom layer is always hexagonal close packed, the top layer has the freedom to pack into square [100] configuration and co-exists with the hexagonal lattice (Figure 2.3.3 c). In all ethanol cases the lattice defects, both grain boundaries and vacancies, are greater than those in aqueous samples. Mixed solvent evaporate faster, leading to more scattered smaller clusters rather big lattice domains. The irregularity in the bottom

layer caused by small domains provide different energy traps for the top layer and hence the co-existing of square and hexagonal format observed in SEM images. The larger bottom domain is more likely to support a hexagonal top format, while smaller and scatter bottom domains are likely to hold a different set of configurations including the square ones. Pure ethanol suspension is not able to create any ordered microstructure (Figure 2.3.3 d), the evaporation rate is high enough that the surface is dried before nanopheres finding their lowest energy configuration site. As a consequence, nanospheres would likely stay at the same position before and after the solvent evaporated, leaving an unordered colloidal film as can be seen in Figure 2.3.3. d).

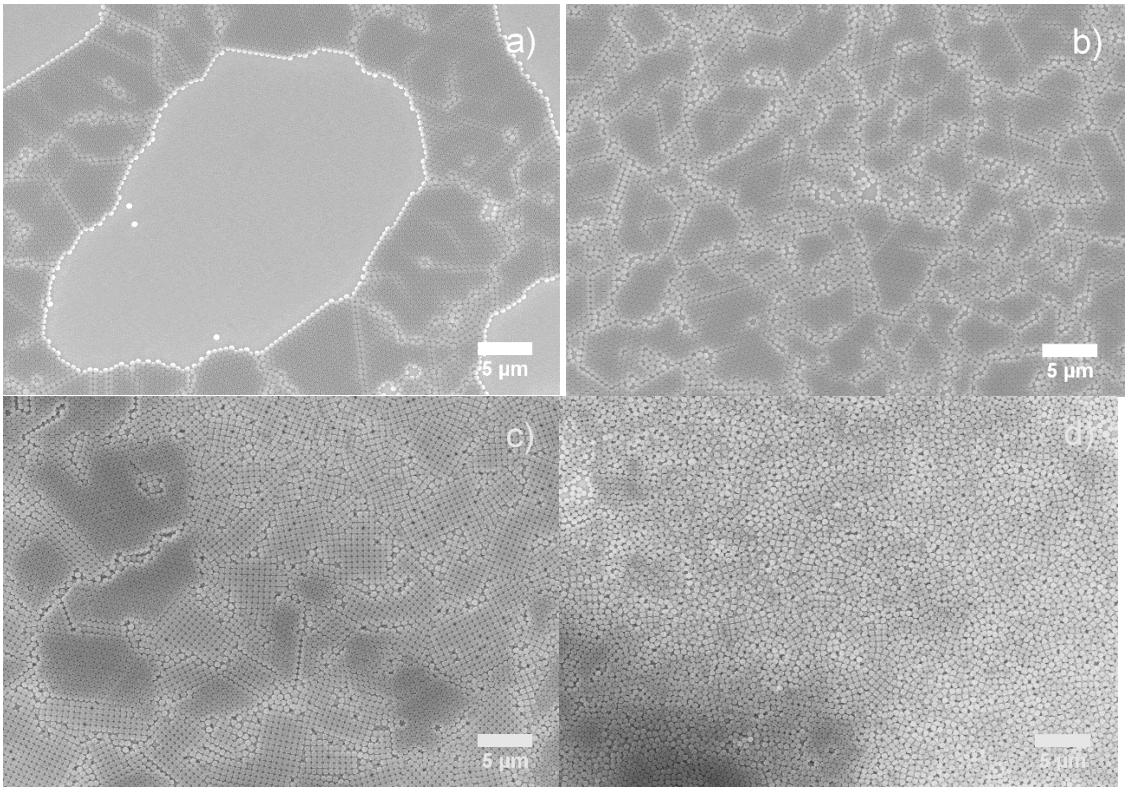

Figure 2.3.3. SEM images of polystyrene 500 nm nanosphere in 10% wt spin coated on Si (100) wafer at 3000 rpm, solution content is EtOH:water = 30:70, 50:50, 70:30 and 100:0 for a-d respectively

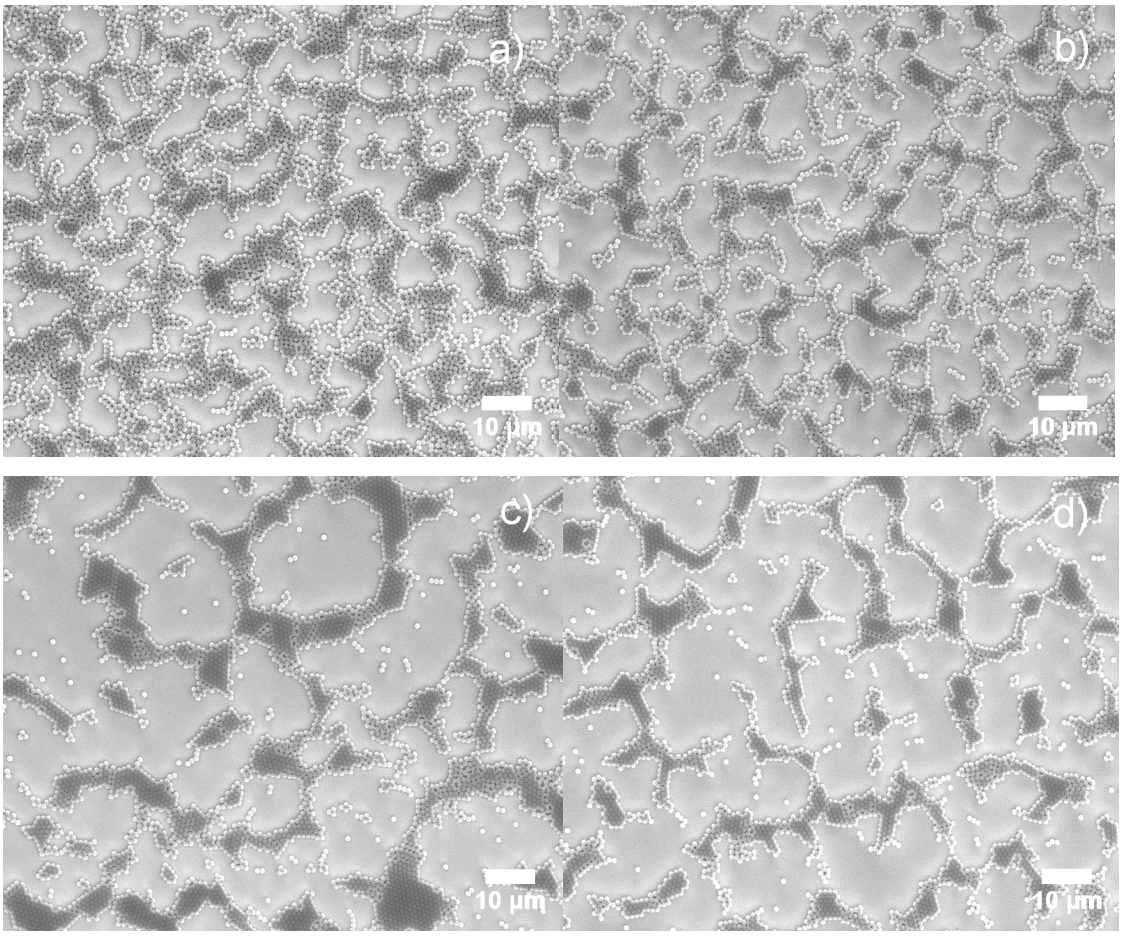

Figure 2.3.4. SEM images of polystyrene 1000 nm nanospheres in 10% wt aqueous solution spin coated on Si (100) wafer at rotation speed = 2000 rpm (a), 4000 rpm (b), 6000 rpm (c) and 8000 rpm (d), acceleration speed = 1500 rpm/s (a-d)

Spin coating on nanospheres with diameters of 1000 nm or above have seldom been reported successfully. Chen et al. report that their optimum settings for 1300 nm PS microspheres are about 4000 rpm rotation speed and 1600 rpm/s in acceleration. As can be seen from their optical images[70], the 1300nm sample has noticeable voids when compared to other samples with PS beads of less than 510nm. In this study, similar results were found (Figure. 2.3.4). As the rotation speed increases, the beads form discrete irregular HCP domains with the presence of free individual beads and bead clusters increasing. The overall HCP coverage decreases with the rotation speed. Using image processing software, the best coverage is given by the low rotation speed

group. It must be noted, however, that the best candidates have 41% HCP yield, and only 24% HCP coverage obtained in 8000 rpm group (D4). According to Denkov's theory, the continuous ordering process relies on two major factors: 1) the capillary forces due to inter-particle liquid evaporation, which pushes beads together, and 2) water flux compensation, which supplies more beads to the ordered domain, so that the domain grows. The SEM analysis reveals that the inter-particle capillary force are weakened in low speed samples, as the beads are loosely attached to each other and there is no long range HCP, the force is strengthened as the rotation speed increases, as a result, more close-packed structure forms gives arise to the dark area on SEM images (Figure 2.3.4 c) and d). Moreover, the overall coverage reduced with rotation speed, indicating the diameter of the bead plays an important role in HCP formation. In Denkov's theory, the onset of ordering process starts earlier and the evaporation-induced horizontal capillary forces in the central area draw suspension flux from the boarder aggressively while the centrifuge force is pushing beads away from center. As a consequence, there is insufficient compensation flux and less sphere supplies to the ordered domain. This results in more voids added to the ordered area. The speed influence on small beads, like those 500 nm in diameter, can be generalized in Figure 2.3.5 a). while for larger beads (D > 1000nm), high rotation speed facilitating the evaporation process creates more and larger voids on the surface for large nanospheres (Figure 2.3.5 b).

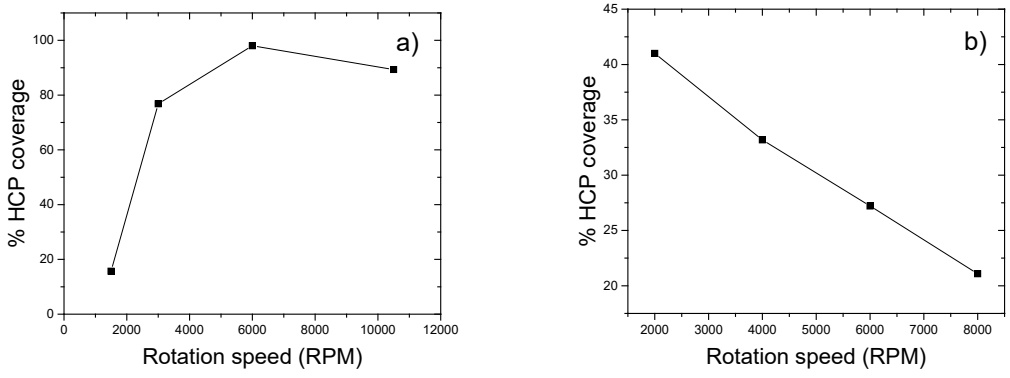

Figure 2.3.5 500nm (a) and 1000nm (b) rotation speed vs HCP coverage

On the other hand, increasing the mass of the beads increases the friction between beads and the wafer surface. Once the beads are attached to the surface due to the increased friction, larger beads are immobilized before they can reach and join the ordered domain, thus increasing unordered areas. This mechanism is also supported by investigating smaller beads deposited on rough surfaces. Figure 2.3.6 shows 500 nm beads on soda lime glass surface (a) and on polished silicon surface (b), both coated using the same recipe. The voids and disorders on the soda lime glass surface are similar to those found in 1000 nm silicon samples. By speeding up the evaporation, the horizontal attracting capillary force increases, which is a good for smaller beads as they move faster toward the ordered domain, but for larger beads the increase in the evaporation rate also increases the vertical component of the capillary force, which presses them against the glass surface. The increasing friction between the beads and the surface immobilizes a greater number of beads and thus results in more voids in the colloidal mask.

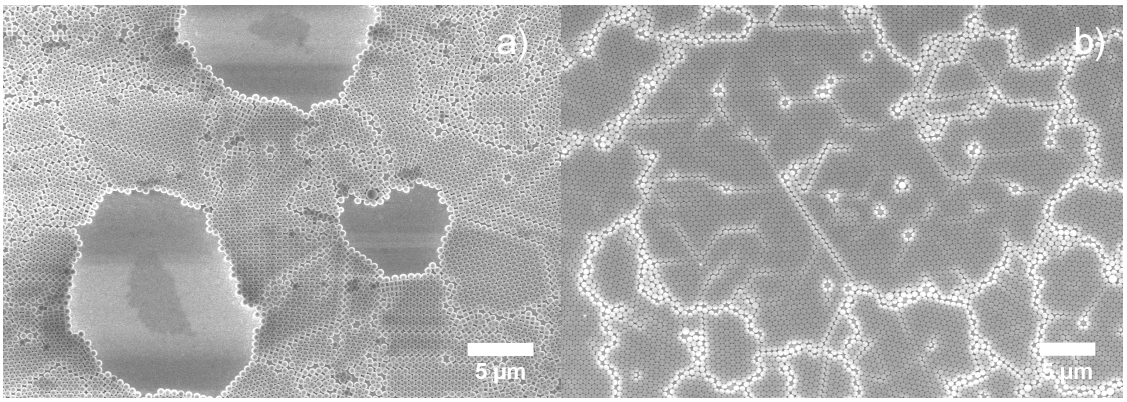

Figure 2.3.6. SEM images of nanosphere (diameter = 500nm) spin coated on glass surface (a) and silicon surface (b) at rotation speed = 6000rpm, acceleration speed = 600rpm/s

2.2.2. Angled interface coating

The failure of NSL implementation of larger polystyrene nanosphere pushes the research to find another cost efficiency way to fabricate uniform nanosphere monolayer. Moreover, the substrate insensitive nature also makes it flexible and adaptable to solar cell built on a large number of substrates. In case of a-Si:H, the substrate can be stainless steel, fused glass, sapphire, plastic, mica or silicon. In addition to substrate type, the cell thickness and substrate properties also varies. For instance, traditional spin coating tool cannot handle soft material such as plastic, and also the thickness and weight of the wafer must be within a certain range otherwise the spinner cannot drive it to desired spin speed. Interface coating has zero prerequisition on the substrate as long as it does not dissolve in the solution being used. The monolayer formation is driven by self-assembly on the interface. The merit is that the monolayer is the only configuration, any quasi-stable configurations such as bi-layer or multi-layer won't be able to form in interface coating. Interface coating does require careful manipulation of the surface tension and solvent pH, with the withdrawal angle and velocity being major concerns when producing high quality colloidal film. In the past, these protocols demanded additional modification of the solvent with chemicals, such as surfactants[89], alkaline[85], and other devices or tools[83,90]. Introducing a surfactant is widely accepted to help acquire larger areas of ordered colloidal film with considerable mechanical strength, since surfactant molecules occupy the interface and push the incoming beads together, ceasing the Brownian motion of individual bead or small bead clusters. This forces them to join and form larger domains, increasing monolayer order[89]. Surface tension at the interface is largely reduced due to the presence of the surfactant, which in turn facilitates bead movement along the interface to find their lowest energy configuration. The result is a more ordered HCP monolayer[91]. Adding the surfactant, however, introduces contamination to the interface. These contaminates can be transferred to substrate in the lift-up process and are especially difficult to remove, thus creating imperfections in the nanosphere lithography.

This study targets mainly on larger nanosphere (1000nm) interface coating, 500nm nanosphere were used as contrast. We hope to develop a convenient method to fabricate large scale arrays using angled interface coating without using any surfactant. Detailed steps are listed as following (Figure 2.4.1 a-d):

1. The nanosphere suspension is centrifuged at 7500 rpm for 10 minutes
2. It is then redispersed in a solvent (H_2O/ethanol, v/v=1:1) to have 10% solid weight.
3. For substrates, microscopic glass slides were purchased from VWR Corp.
4. The glass substrates are cleaned in piranha solution (98% H_2SO_4 and 30% H_2O_2, v/v=3:1) at 100˚C for 30 minutes. It should be noted, that this process can be scaled to larger pieces of glass using the same approach.
5. The cleaned glass slides are stored in deionized water for no more than a week before use.
6. At room temperature, the microscopic glass substrate is dried under N_2.
7. A glass Petri dish is filled with deionized water.
8. The glass slide is positioned at a 45˚ angle in the Petri dish as shown in Figure 5a. This angle is chosen since it optimizes that speed at which the suspension droplet enters the water/air interface.
9. 20µl of the newly made nanosphere suspension is pipetted onto the glass slides and moves freely along the slides into the water/air interface. It should be noted that each time only a tiny drop (~2µl) is pipetted, with the next drop not being added to the glass slide until the prior drop has completely diffused and there is no visible movement identifiable by naked eye on the water/air interface. By doing so, the new drop will not interfere with the diffusion process of the prior drop and turbidity is thus minimized. It should also be noted that the pipetting can be done by hand or automated with an open source syringe pump[92].

10. Pipetting the suspension is continued at a constant speed until the entire interface is covered by colorful gratings caused by the diffraction from the ordered nanosphere array.

11. The array is transferred to a 1’ by 1’ hydrophilic silicon or glass substrate at an angle of 10˚ with respect to the water/air interface using a 3D printed wafer holder as shown in Figure 2.4.2. The merit of 3-D printing is that one can design and fabricate labwares in a fast and easy way[93,94].

12. Finally, the lifted wafers are air dried – placed leaning against an object or 3-D printed holder so that they form an angle with the ground, ensuring that all the water is optimally evaporated.

To demonstrate and test this methodology, the samples are analyzed in FE-SEM after depositing 2 nm of platinum, which is sputtered in order to provide good conductivity for FE-SEM analysis.

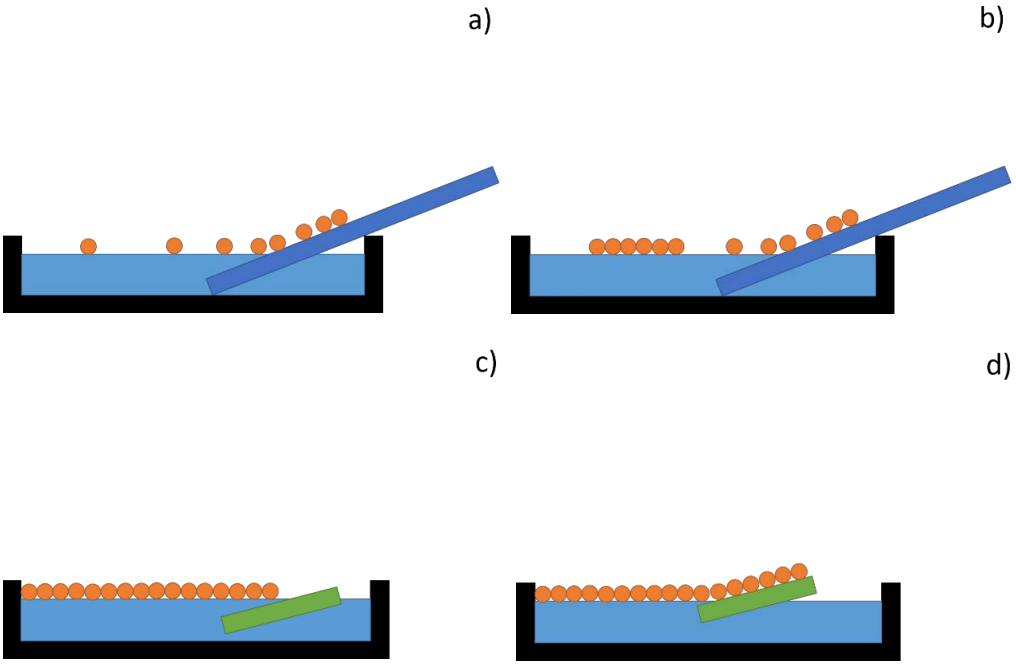

Figure 2.4.1. Schematics of interface coating. (a) Nanosphere suspension pipetted onto an angled glass substrate and move onto water/air interface. (b) Nanosphere start assembling on water interface. (c) As more suspension join the monolayer, a full coverage over the surface is obtained. (d) Substrate entered the water phase at a shallow angle (~10˚) to transfer the monolayer.

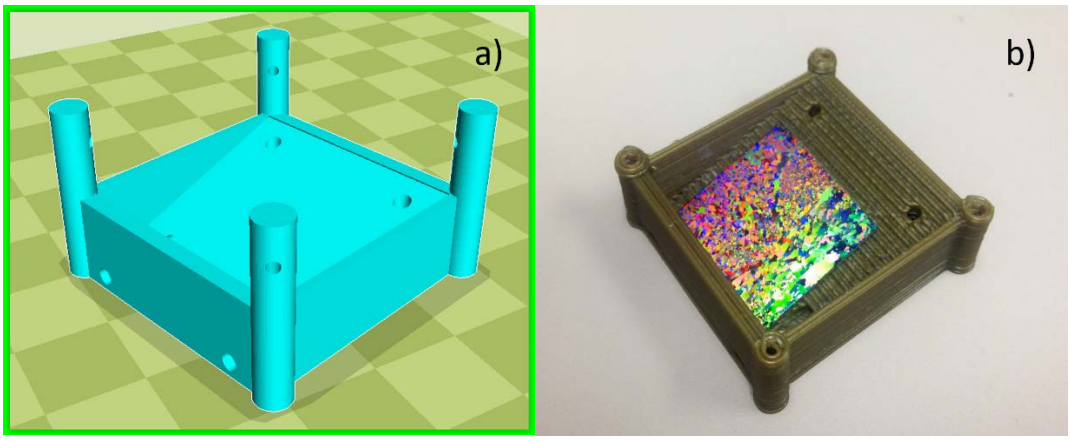

Figure 2.4.2, a) Rendered OpenSCAD file as an STL file in the open source slicer Cura showing design of angled wafer holder for 3-D printing, b) a printed holder holding a wafer on angled surface.

Uniform coverage of monolayer beads is obtained by gently adding the beads suspension to the glass dish through angled slide. Beads that are free for diffusion across interface require time to become stable. Quickly pipetting the beads suspension results in clusters or agglomerates appearing as white residues in the water phase. In the initial state, the beads suspension droplets at the edge of the angled glass slide gradually release the beads into the water/air interface. The 1000 nm beads slide onto the interface without aggressive diffusion, instead forming a uniform monolayer at the moment they engage the water. The process is similar to that of making an omelet where the whisked egg slowly poured onto a hot pan immediately forms a flat crust. In contrast, the 500 nm beads diffuse rigorously and soon reach the border of the glass dish. A small fraction of the 500 nm beads rush into the water phase and cause an optically white suspension. With the assistance of ethanol, the lighter beads, the faster they move. This results in more freestanding beads at the interface and suspending beads in the water phase. For the 500 nm beads, no noticeable monolayer forms at the beginning, but when more bead suspension is added to the water phase, the beads start to form scattered monolayer domains. The area of these domains increases as they receive new beads and join with other proximal domains. Towards the end of the pipetting stage, full surface coverage can be achieved (Figure 2.4.3). In both the 500 nm and 1000nm bead cases, full surface coverage can be achieved by continuously pipetting the beads suspension until white turbidity at the glass/water intersection can be observed by naked eyes, indicating that there's no more room on the interface for new beads to join the monolayer and further adding will force the beads to run into the water phase hence the cause of the whites.

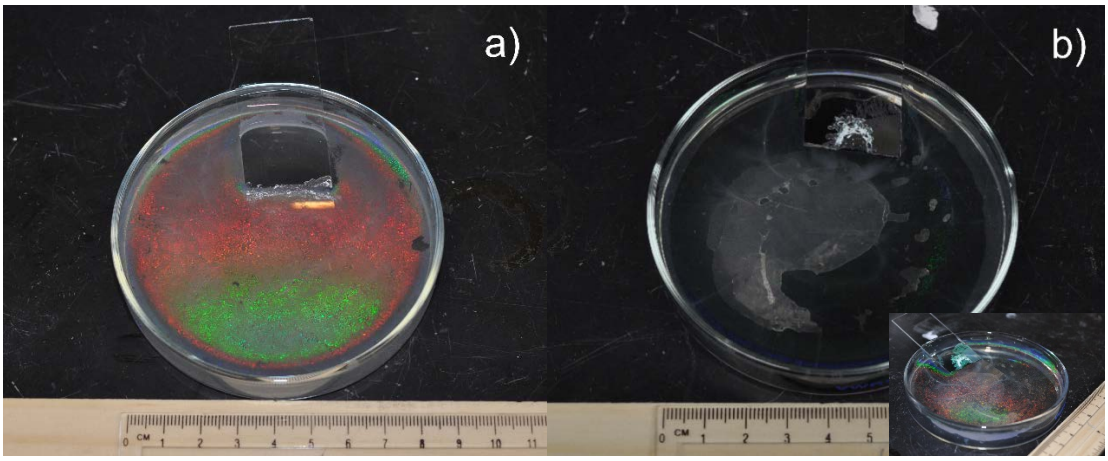

Figure 2.4.3. Full coverage of nanosphere monolayer on water surface without using SDS, nanosphere diameter = 1000nm (a) and 500nm (b). The photos were taken using digital camera with built-in flash on. Due to the optical property difference, the 500nm nanosphere sample does not show diffraction at the same angle of observation as the 1000nm nanosphere does. The inset image of (b) shows the photo of the same sample taken at a different angle.

To provide a contrast between surfactant-aid and surfactant-free coating, the interface coating is divided into two groups: in Group A, no surfactant is added and the colloidal coating is transferred to the substrates 30 minutes after full coverage has been identified by naked eye; in Group B, an anion surfactant, sodium dodecyl sulfate (SDS), is added to the self-assembled monolayer. It is observed that the monolayer is rigorously pushed by the surfactant molecules when the SDS solution (2wt %) is pipetted into the interface. SDS molecules occupy the interface aggressively, and the colloidal film is pushed away to leave room for the SDS. For full surface coverage, since introducing SDS doesn't push the colloidal film much, it is believed the nanospheres on a fully covered surface have already formed the close-packed structure and their mechanical properties are strong enough to resist the spreading SDS modules.

Figure 2.4.4 shows 1000 nm of colloidal film transferred onto a silicon substrate using a surfactant-free recipe. The 2-D crystalline blocks can be easily distinguished by their distinct diffraction orientations, which lead to different colorations at the same angle of

observation. Large and uniform diffraction regions indicate large, ordered crystalline domains. The largest domain observed here is about 3 mm^2, which seldom reported by other groups. For 1000 nm colloidal films, FE-SEM analysis barely shows any difference between Group A and Group B samples except that Group A has a slightly higher content of bead triplets due to the stress release mechanism when two crystalline domains join[90] (Figure 2.4.5 a) and b). For the 500nm samples, SEM analysis reveals the importance of using a surfactant. With the assistance of SDS, a uniform and a well-ordered HCP structure is obtained with interface coating (Figure 2.4.5 c) and d). Fewer triplets and dislocations are found in the SDS samples. In non-surfactant samples, significant voids and unordered domains and large numbers of triplets and vacancies are observed.

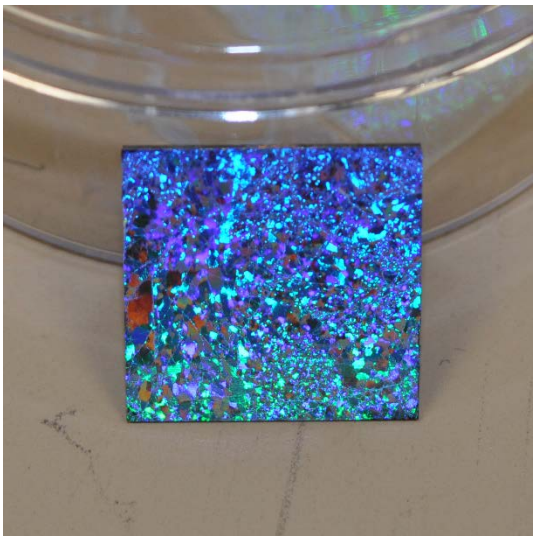

Figure 2.4.4. Transferred colloidal monolayer (1000nm nanospheres) on silicon substrate (1’ x 1’). Observed area of single crystalline block reaches 3 mm^2.

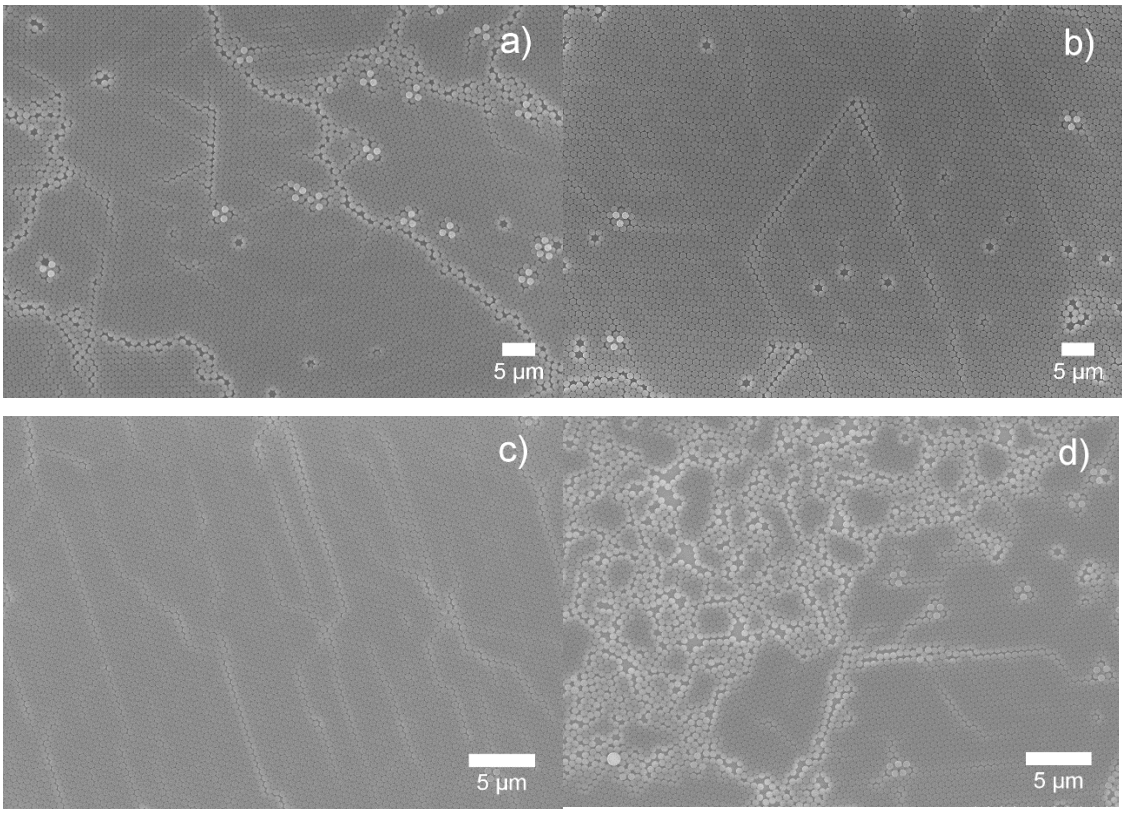

Figure 2.4.5 1000nm (a,b) and 500nm (c,d) nanosphere monolyer via interface coating with (a,c) and without (b,d) the assistant of 2 wt% SDS.

A possible explanation for the observation is that for larger beads, the mutual attraction is greater. In order to balance the bead weight, the water's surface must be curved in order to provide a surface tension force with a large enough vertical component to support the beads (Figure 2.4.6 a). The larger the beads, the greater the supporting force needed, and hence a larger curvature on the interface underneath. The curvature cross-section is slightly larger than the bead cross-section, and for larger beads this curvature has larger cross-sections which can interact with other beads nearby. When a bead is caught in Brownian motion, the two beads join into a small cluster to rebalance the horizontal component of the surface tension (Figure 2.4.6 b) and c). The clusters in turn capture more beads. This process can be analogously understood by imagining throwing a volleyball on a large flat sheet of fabric. The bending sheet caused by the weight of one volleyball draws other volleyball passing by. The process repeats as

more beads are pipetted to the interface until there's no more space for incoming beads to join the monolithic monolayer domain. Introducing the surfactant as interconnector is not necessary. It is worth mentioning that the process is strongly influenced by the size of the droplets as well as the angle at which the assisting glass slide is placed, both of which control the initial speed of the droplet as it engages the water/air interface. Figure 2.4.7 and Figure 2.4.8 shows the angle and droplet size effects. The larger the droplets or slope, the faster the engaging speed, leading to an increase in turbidity and a more scattered crystal domain (Figure 2.4.7 b) and Figure 2.4.8 b). Even though the scattered domains may join into larger domain eventually, the domain boundary density increases, hence the defects increases. When using smaller droplets (~1μL) and inserting them at shallow angles, the beads are much more likely to form a crystalline monolayer immediately after engaging the water/air surface (Figure 2.4.7 a) and Figure 2.4.8 a). Continuously adding the beads in this manner will only increase the area of the monolayer. It is good practice to produce high quality film by pipetting the smallest droplet on a slide that is at a shallow angle (optimally around 24˚).

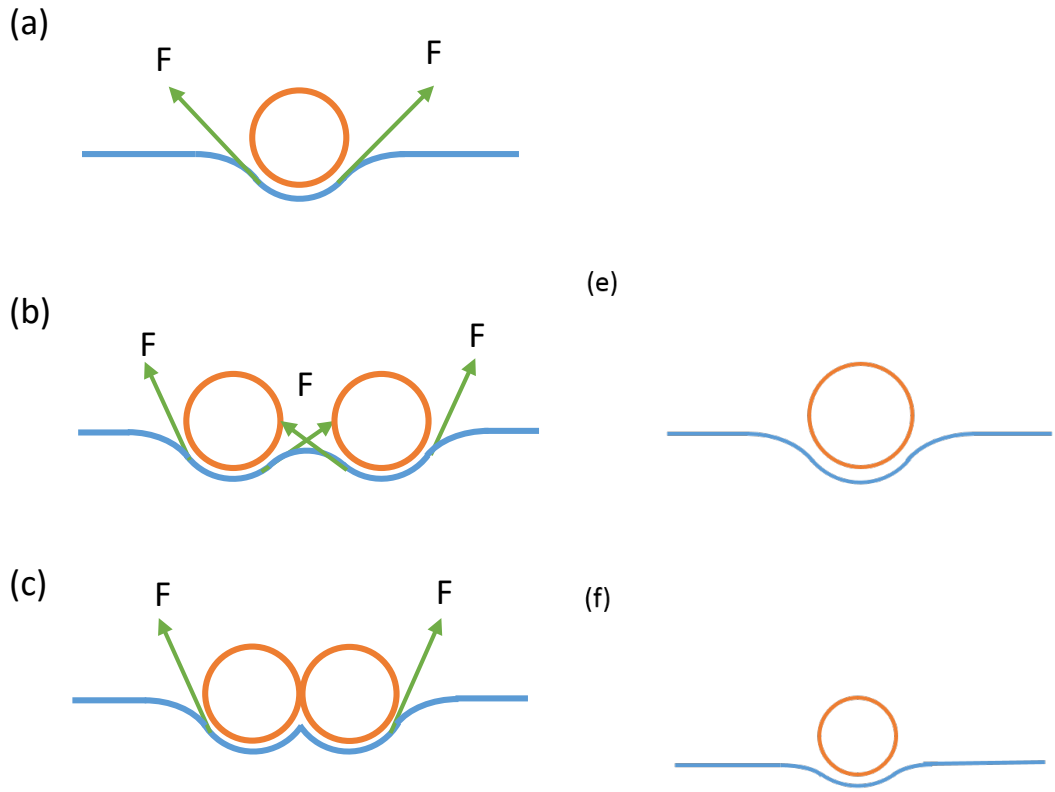

Figure 2.4.6, (a) individual bead is balanced by the surface force (b) when another beads is approaching, the balance of the horizontal component of the surface force is broken and mutual attraction of the two beads is demanded to rebalance the force, (c) the two beads end up with sticking to each other and the force is rebalanced.(e-f) Unlike larger bead, smaller beads need less surface force to balance its weight and therefore less likely to attract free nearby beads, they undergo Brownian motion until there is less room left and the interaction with surrounding beads increases. This process occurs when the whole surface reaches full coverage

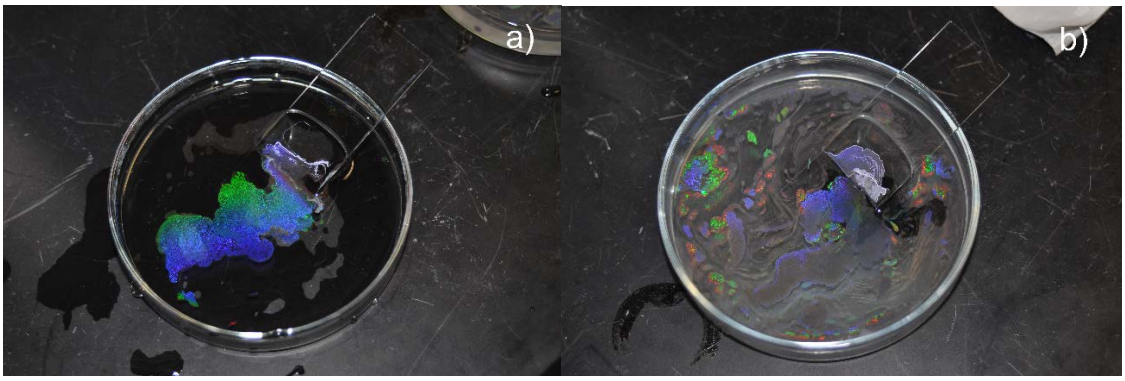

Figure 2.4.7. Digital images show result of colloidal film made from pipetting (a) 5 droplets of beads suspension, each contains ~1μL suspension and (b) 1 droplet of 5μL suspension.

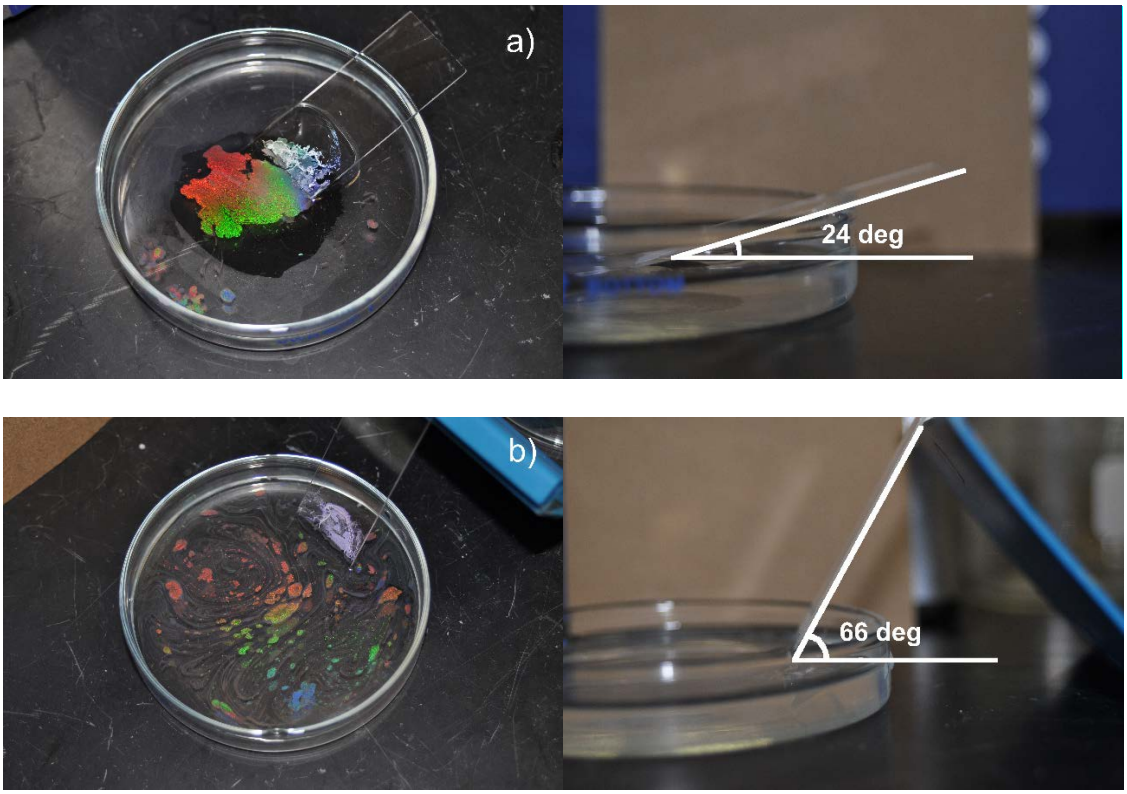

Figure 2.4.8 Colloidal film made from pipetting ~2μL 1000nm nanospehre suspension at (a) 24 degree and (b) 66 degree angled glass slides.

If the bead weight is too small, the induced surface tension may not be able to bend the water surface enough to draw in the nearby beads (Figure 2.4.6 e) and f). The beads remain in Brownian motion until the surface tension is modified by other processes (e.g. by introducing a surfactant to the interface). At the same temperature, smaller particles additionally tend to move faster and are less easily captured by other beads or bead clusters. Consequently, more voids and vacancies are found in 500 nm bead samples without SDS. During film transfer, it is also found that for Group A samples, the monolayer is fragile and breaks apart when trying to transfer it onto a substrate. This is possibly due to the weaker attractions between the smaller beads, which makes it more difficult for them to hold their positions during transfer. The Group B samples shows stronger mechanical strength, and the film is easily lifted up from the interface with no broken parts found. This is because the "gluing" effect between beads is enhanced by SDS. For the 1000 nm beads samples, both groups display similar mechanical strength and both are easily lifted up, proving that a strong interaction exists among larger beads even without the aid of a surfactant. It can therefore be concluded that for smaller beads, using a surfactant is necessary in order to achieve high HCP coverage.

Bilayers, voids, and non-HCP structures are considered defects and are not added to HCP percentage. The optimized maxima for each recipe is summarized in Table 1. This selection of method and optimization depending on nanosphere size will help facilitate the process and production of contamination-free samples for fabrication and research.

Table 2.4.1. HCP coverage percentage for each optimized coating recipe.

HCP%	500nm spin coating	1000nm spin coating	500nm interface coating (SDS)	1000nm interface coating (SDS)	500nm interface coating (no SDS)	1000nm interface coating (no SDS)
	98	72	90	91	54	89

2.3. Conclusion

In this chapter, novel approaches have been demonstrated to fabricating large colloidal HCP structures using polystyrene beads. Spin coating was found to be the more favorable way of implement coating for smaller (500 nm) beads, while for larger beads there is insufficient water flux compensation during spin coating such that beads stick, preventing large scale monolayer formation. The opposite is true for interface coating; larger beads can be used to attain a monolayer more easily, and even without the help of surfactant, than smaller beads, which are fragile at boundary hence have a reduced HCP yield. This difference can be attributed to the surface forces that arise from surface curvature, drawing in nearby beads as the amount of beads increases. Spin coating the 500nm beads, and interface coating the 1000 nm beads without SDS reach around 90% coverage. These optimized recipes will be applied in cell fabrication in later chapter.

3. Leveraging plasmonic enhancement in amorphous silicon solar cell via hexagonal array[1]

3.1. Motivation

Hydrogenated amorphous silicon (a-Si:H) solar photovoltaic (PV) cells provide an inexpensive alternative to bulk crystalline silicon (c-Si) cells[9,10]. Compared to c-Si cells, whose thickness ranges from ten to hundreds of microns, the high absorption coefficient of amorphous silicon enables a-Si:H PV to absorb sufficient solar radiation at submicron level[9,10]. Although material costs are reduced, a-Si:H cell efficiencies are lower as the material suffers from high defect density and short minority carrier diffusion length[95]. Additionally, a-Si:H has light induced degradation known as the Staebler-Wronski Effect (SWE)[8,96,97], which is dependent on the thickness of the absorber material (i-layer) in an a-Si:H device. Light trapping mechanisms are necessary to assist in alleviating both of these challenges and several forms of optical enhancement have been used in the past[5,98].

One common approach is to introduce a textured anti-reflection surface, which inevitably increases the amount of surface defects, hence increasing recombination sites[20,22]. In order to avoid this deficiency, surface plasmonic nanostructures provide a promising approach to enhancing optical absorption in thin film solar cells and have therefore been investigated[99,100]. Top contact optical enhancement methods have an advantage in terms of fabrication simplicity and avoidance of the substrate effect from the protocrystalline nature of Si:H[101,102], that introduces defects in the i-layer. Many studies have shown the benefits of the light trapping effect through top metallic scatterers[37,103,104]. In addition, if the metal is made up of nanoparticles, they not only behave as light scatterers but also enable light trapping

[1] This chapter is submitted as "C. Zhang, D. O. Guney and J. M. Pearce, "Leveraging plasmonic enhancement on amorphous silicon solar photovoltaic with hexagonal silver arrays" to *Solar Energy Materials & Solar Cells*

through high order diffraction[41,105], Fabry-Perot resonance[31], and decrease the top contact sheet resistance.

Although the advantages of plasmonic structures have been well investigated, no plasmonic–based a-Si:H solar cell has been commercialized due to two primary reasons: 1) the effect was demonstrated on unrealistically thin solar cells[77] that if scaled demanded an ultra-thin transparent conducting oxide[106,107] and 2) current fabrication constraints. Recently, work on ultra-thin TCOs has been successful[106] , which provides the potential to use this approach on full solar cells. However, traditional fabrication techniques, such as e-beam lithography and focused ion beam, are cumbersome, expensive and difficult to scale up, therefore making them improbable for industry level fabrication. Nanosphere lithography (NSL), however, provides a low-cost scalable technique: by self-assembly, NSL creates size- and shape-controllable colloidal masks, which ease the fabrication of plasmonic patterns via common evaporation or sputtering tools. Depending on the techniques and procedures, patterns like triangle[108], rod[73], cylinder[109,110], ring[73,111] or dot[73,108] are developed and their size and spacing can be tuned by selecting appropriately sized spheres.

Previous work provides an opportunity to use NSL for light management on the front surface of a commercial a-Si:H PV cell. Van Duyne et al. completed extensive research on the optical properties of NSL-fabricated plasmonic arrays[108] and Morarescu et al. studied the localized surface plasmon in gold triangular array for sensing applications[112]. For PV application, NSL is widely used in rear contact scenarios to excite SPP and/or high order diffractions[58,61,75,113]. However, the top contact scenarios using NSL are rarely found in literature. Giulia et al. report on a conceptual cells with the capability of 88% absorption using a tapered triangle nanoarray for a metal-insulator-metal structure[114]. The discovery, although using a conceptual solar cell, inspired the study of using NSL in top contact scenarios for thin film solar cells. Here a systematic simulation study is conducted to determine the capability of achieving efficiency enhancement in a-Si:H solar cells using NSL as a top contact

plasmonic optical enhancer. The study focuses on triangle and sphere arrays as they are the most commonly and easily acquired through direct deposition or low-temperature annealing, respectively. Other patterns such as cylinders, rings or bowls require additional processing and/or equipment that is cost efficient for commercialization. The reference cell to be employed has the same structure without the presence of the plasmonic nanoparticles. For optical enhancement, a characteristic absorption profile is generated and analyzed to determine the effects of size, shape and spacing of plasmonic structures. Conclusions are drawn to validate the feasibility of fabricating commercial cells with this low-cost, widely-accessible, and easily-scalable method.

For top contact plasmonic-enhanced PV, the mechanism that contributes to the optical enhancement is forward scattering where the electric field of the incoming plane wave excites a collective oscillation of free electrons in the conduction band in a metal particle, causing re-radiation of light from the metal particle's surface. For particles of subwavelength dimension, the solutions to Maxwell's equation transits from the Rayleigh model to the Mie model[34]. According to Mie's theory, two important physical quantities can be obtained: the scattering and absorption cross-sections, which are defined as the net energy rate of scattering radiation and absorption divided by the incident irradiance. For the scattering field emitted from a dipole moment, the scattering and absorption cross-sections can be expressed as:

$$\sigma_{sc} = \frac{8}{3}\pi a^2 q^4 \left| \frac{\frac{\varepsilon_p}{\epsilon_m} - 1}{\frac{\varepsilon_p}{\epsilon_m} + 2} \right|^2 \tag{3.1.1}$$

$$\sigma_{abs} = 4\pi a^2 q \mathrm{Im}\left[\frac{\frac{\varepsilon_p}{\epsilon_m} - 1}{\frac{\varepsilon_p}{\epsilon_m} + 2} \right] \tag{3.1.2}$$

where ε_p and ε_m are the relative dielectric functions of a metal particle and the medium respectively, a is the radius of the particle and q is a dimensionless quantity equaling ka^2, where k is the wave vector in the medium. From the equation it can be seen that surface plasmon resonance occurs when $\varepsilon_p = -2\varepsilon_m$, at which both the scattering and

absorption cross-sections exceed the geometrical cross section. Thus, full extinction of the incoming light can be achieved with a fraction of surface coverage. A typical silver nanoparticle with a diameter of 90nm creates a scattering cross-section 10 times larger than that of the geometry cross-section. In addition to dipole modes, radiation damping and dynamic depolarization in large particles break down the quasi-static approximation and enable higher order modes to exist[16,115]. Akimov et al. discovered the separation of scattering and absorption induced by high order modes, which makes them advantageous in thin-film solar cell applications[116].

Surface plasmon resonance is significantly influenced by particle size, shape and the surrounding environment. For PV applications, the ideal resonance covers a broad range of the spectrum where the photo-active material absorbs most of the radiation (in a-Si:H based PV this is the i-layer). In addition to the scattering cross-section, the corresponding absorption cross-section should be attenuated to avoid absorption competition with the photo-active material. Those are the two principles in designing a plasmonic-enhanced cell. However, NSL has its limitations in pattern creation. With nanospheres of a fixed size, the close packed hexagonal array pattern is the only pattern available. Efforts have been made to extend the diversity of geometric patterns through NSL using multilayers[108], non-close packed arrays[117,118], and non-hexagonal symmetries[118]. However, literature rarely reports applications of these novel structures, largely due to the difficulty in uniformly replicating these structures, particularly over large areas.

In this study, two of the most common structures from NSL are investigated and the results compared for the 1) nano-triangle array by direct deposition through a colloidal mask and 2) the nanosphere array following the gentle annealing of the nano-triangles. These approaches do not require sophisticated equipment or processing. They are both stable, provide high yield products and are straight forward to scale up at low-cost, meeting the industrial requirements for commercial solar cells.

3.2. Methodology

The simulation is carried out using COMSOL Multiphysics 5.1 with the RF module package, which is based on finite element methods (FEM). The scattering cross-section study and solar cell performance analysis are performed separately with different setups, as described below.

3.2.1. Cross section model

Simulation work for cross-section analysis is based on a single scatterer where the interaction with scattered fields from other scatterers are neglected. The isolation is necessary in order to obtain an accurate calculation of the cross-sections. The interactions between the scatterers are included in the cell simulation in which the array of scatterers is taken into account. Models for the triangle and sphere cross-section analysis are shown in Figure 3.2.1 a) and b), respectively. Silver nano-triangles/spheres sit at a square center, the top and bottom half of the model are air and ITO, each with a thickness of 750nm to provide a far enough space for the scattered and incident fields to propagate. To represent a real cell environment, the ITO used in the simulation has the same optical parameters as the one used in the reference cell. The definition of triangle dimensions is shown in Figure 3.2.2. The three enclosing nanospheres of radius R specify the triangle geometry. The tips of the triangles are filleted to avoid numerical errors around the sharp tips. The spheres are annealed triangles whose volume is assumed to be constant during the shape transformation, therefore the spheres are specified by and compared with their triangle counterparts. The whole structure is enclosed by a 150nm thick, perfectly matching layer to absorb all propagating and evanescent waves. Incident plane waves of intensity I_0 and polarization in the y-direction are excited through the port setup. The scattering and absorption cross-sections are derived from the following equations:

$$\sigma_{sc} = \frac{\oiint \boldsymbol{P_{sc}} \cdot \boldsymbol{n} dS}{I_0} \tag{3.2.1}$$

$$\sigma_{abs} = \frac{\iiint Q_{loss} dV}{I_0} \tag{3.2.2}$$

where dS and dV are the differential surface area and differential volume of the nanoparticle, respectively. P_{sc} is the Poynting vector of the scattered field, $\mathbb{n}$ is the unit vector normal to the particle surface, and Q_{loss} is the power density lost in nanoparticle.

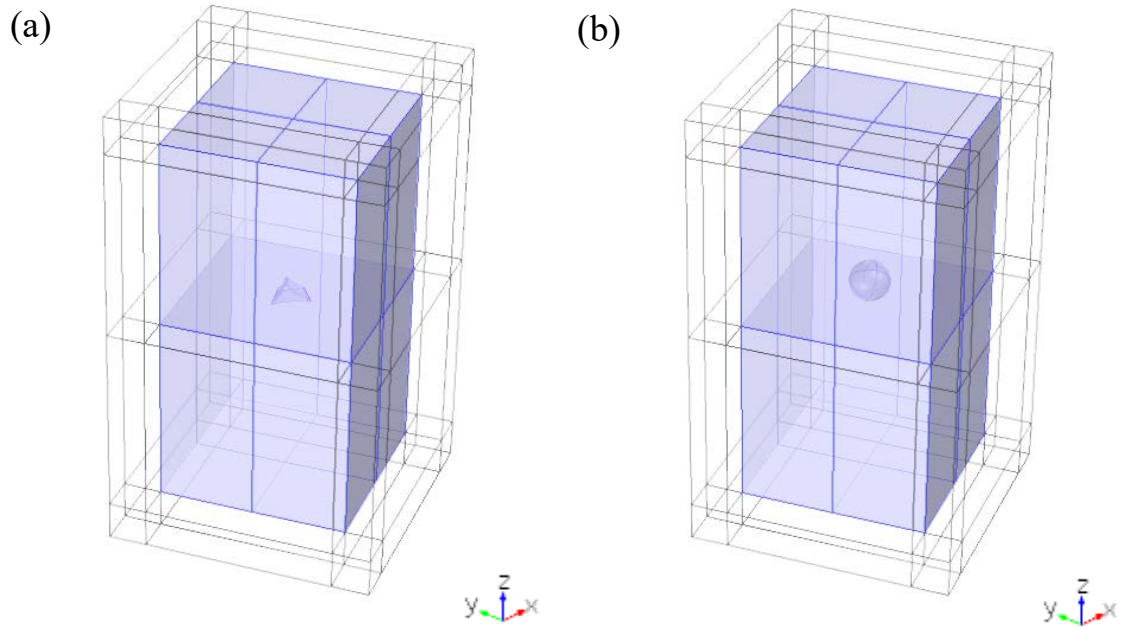

Figure 3.2.1. Models of a single scatterer: silver triangle (a) and silver sphere (b), shaded domains are physical entities, transparent domains are perfectly matching layers (PMLs).

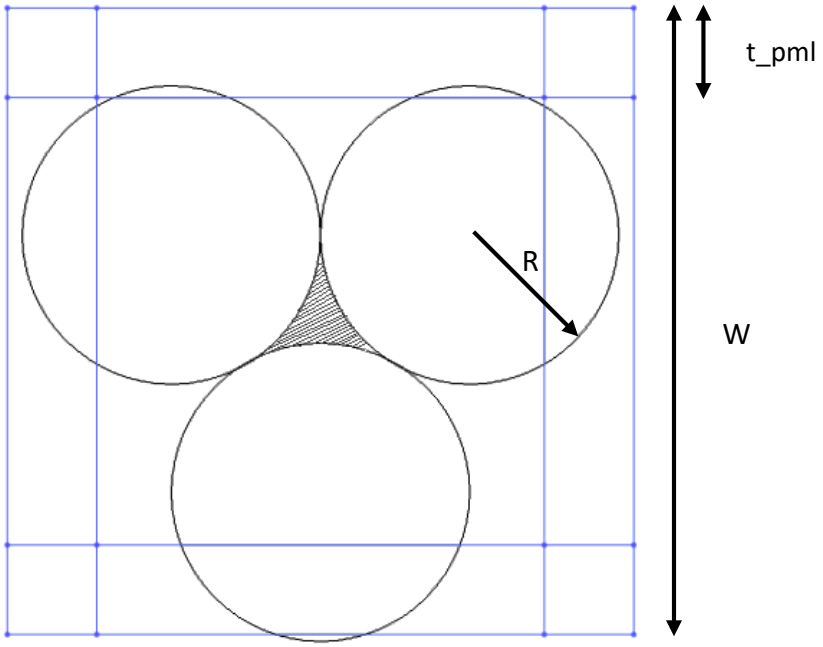

Figure 3.2.2. 2D top view of triangle model, silver triangle dimension is defined by the grey shaded area surrounded by three masking nanospheres with radius *R*. *W* is the length of the unit cell, *t_pml* is the thickness of the PMLs. The triangle tips are tapered to reflect the real triangles produced in fabrication, as well as to avoid numerical errors around the narrow regions in simulation.

3.2.2. Solar cell model

The reference cell employed, shown in Figure 3.2.3, consists of 200nm silver and 100nm aluminum doped zinc oxide (AZO) as the back contact, followed by n-, i-, and p-type hydrogenated amorphous silicon (a-Si:H) photo-active layers with thicknesses of 22.4nm, 350.5nm, and 17.5nm, respectively. A 36nm optimized indium tin oxide layer[106] serves as the top contact. Dielectric functions of the p-, i-, and n-type a-Si:H, AZO and ITO are measured in J.A. Woolam's variable-angle spectroscopic ellipsometer, and the silver data is acquired from S. Babar[119].

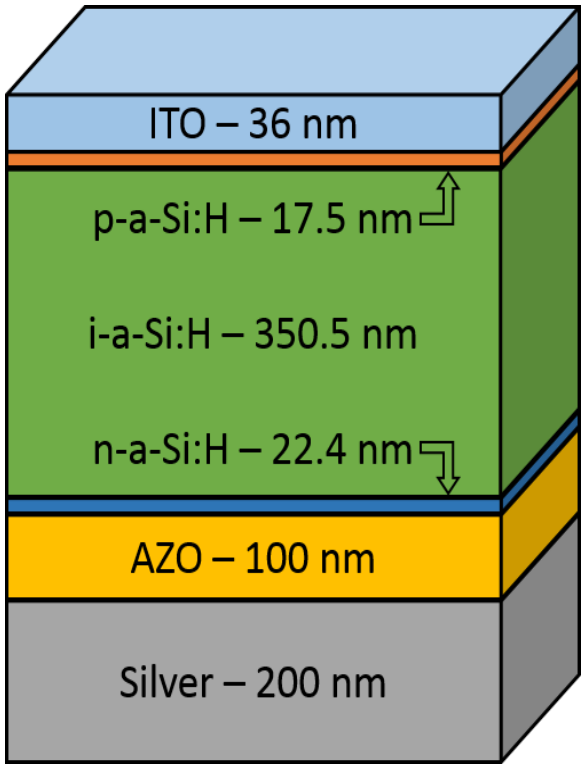

Figure 3.2.3. Reference solar cell structure.

Given the dielectric functions and geometry constants of each layer, the method solves for the full Maxwellian equations in a constrained range of the solar spectrum where a-Si:H is active (300nm to 750nm). Periodic boundary conditions are applied to include interactions between nanoparticles as an array, and also to help reduce the computation resource usage due to lattice symmetry. Electromagnetic waves polarized in the y-direction are sent through a port on top of the structure. PML layers sandwich the cell to absorb escaping waves. The model has included all major optical processes occurring in the structure and is hence very close to real situation. The simulation models are described in Figure 3.2.4.

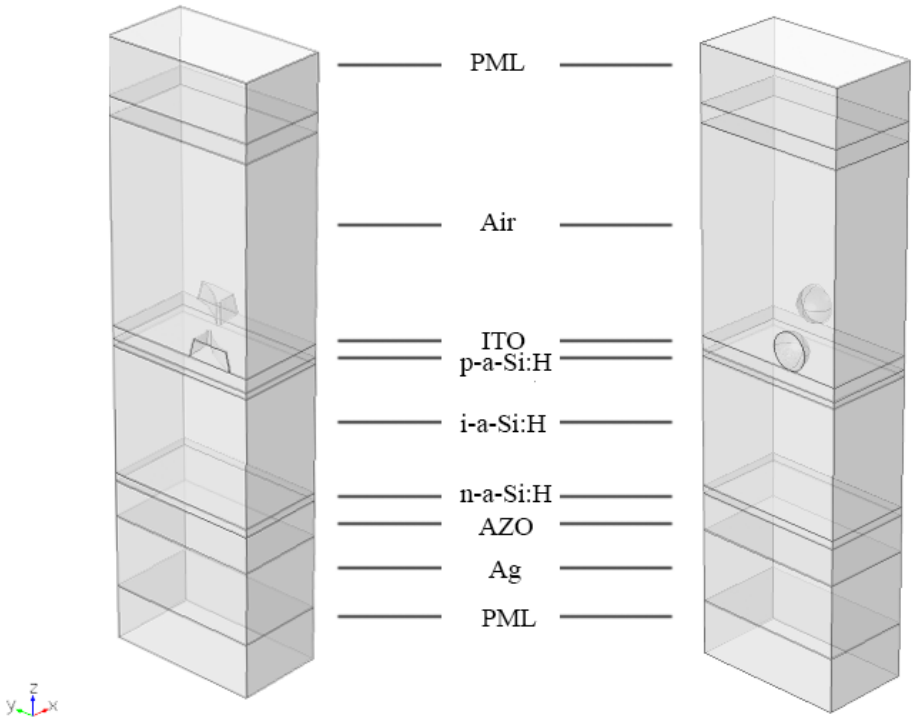

Figure 3.2.4. Models of a-Si:H solar cell with a silver triangle (left) and a silver sphere (right), layers from bottom to top are PML (150nm), silver (200nm), AZO (100nm), n-a-Si:H (22.4nm), i-a-Si:H (350.5nm), p-a-Si:H (17.5nm), ITO (36nm), silver particles (various sizes) and air (thickness = 2x wavelength). PEM and PMC boundary conditions are applied on four sides to reduce the computation domain to its ¼.

The power loss densities in each layer are integrated over their volumes to obtain a global absorption profile. The integrated absorption in the i-layer over the AM 1.5 solar spectrum is employed as the standard in the study for cell performance measurement and comparison, as seen in the equation below:

$$OE = \int A(\lambda) Q_{AM1.5}(\lambda) d\lambda \tag{3.2.3}$$

OE is the absorbed power density, $A(\lambda)$ is the ratio of absorbed power to incident power, $Q_{AM1.5}$ is the solar irradiance spectrum, and air mass = 1.5, obtained from the National Renewable Energy Laboratory (NREL)[120].

3.3. Results and discussion

Scattering cross-sections of single triangle and sphere scatterers are illustrated in Figure 3.3.1 (a-d). The shaded area is the photo-active region of a-Si:H and the scattering falling in this region will be advantageous in plasmonic enhancement. The triangle spectrums show two well-separated peaks. The two peaks are associated with two localized surface plasmonic resonance (LSPR) modes – the first order dipole mode (l=1) at longer wavelengths, and the second order quadrupole mode (l=2) at shorter wavelengths. The simulations agree with previously established experimental results[112]. Both peaks are subjected to broadening and red-shifts as the nanosphere size increases. Dipole peaks are more sensitive to size changes and move faster towards infrared, leading to scattering outside the a-Si:H photo-active region (Figure 3.3.1. a). The quadrupole peak is weak in shadow triangles and grows fast as the thickness increases. In Figure 3.3.1 b), a weak peak occurs at 380nm and red-shifts slightly with the triangle thickness, which can be attributed to resonance at higher (l>2). The peak overlaps and merges with its quadrupole neighbor in thicker triangles. High order modes are considered a result of inhomogeneous polarization and are normally seen in larger particles[121]. When the tringle height increases to be comparable to the incident light wavelength, the incident light cannot polarize the triangle within constant phase, this inhomogeneous polarization leads to an electric field gradient in the triangle and consequently, significant retardation of the resonance allows high order modes to arise and even dominate the dipolar resonance when h=200nm in R=350nm. In Fig. 5b there is a tendency for the quadrupolar and dipolar mode resonance peaks to overlap each other as the thickness of the triangle increases. The interferences between the quadrupole and dipole may give rise to Fano resonance, which can be tuned to maximize forward light scattering and benefit a-Si:H absorption[122].

Cross-section profiles of sphere silver scatterer have been widely studied and discussed[121–123]. For PV applications, sphere particles are preferred over triangles due to the larger, broad-spectrum scattering cross-sections of the sphere. More importantly, for a-Si:H, scattering cross-sections stemmed from spheres have better

spectral coverage in the photo-active region. Unlike triangles, spheres are geometrically isotropic and therefore do not have well-separated resonance peaks. Dipole resonance overlaps with high order peaks to provide broader peaks from 340nm to 800nm for larger particles (Figure 3.3.1 c) and d). As the sphere size increases, the separation of the resonance peaks becomes noticeable; for example, in Figure 3.3.1 d), in the h = 200nm group, the dipole, quadrupole, and octupole peaks are at 520nm, 460nm and 400nm respectively. As with the triangles, the scattering cross-section red-shifts and becomes stronger with the particle sizes. As pointed by Akimov, higher order modes can contribute significantly to thin-film cells by maximizing the scattering within while leaving the absorption peak outside the photo-active region[116]. Theoretically, NSL allows the creation of sphere particles of any size. This makes the method extremely useful in PV applications as one can tune the scattering peak to be within the spectrum where absorption is weak due to poorly trapped light.

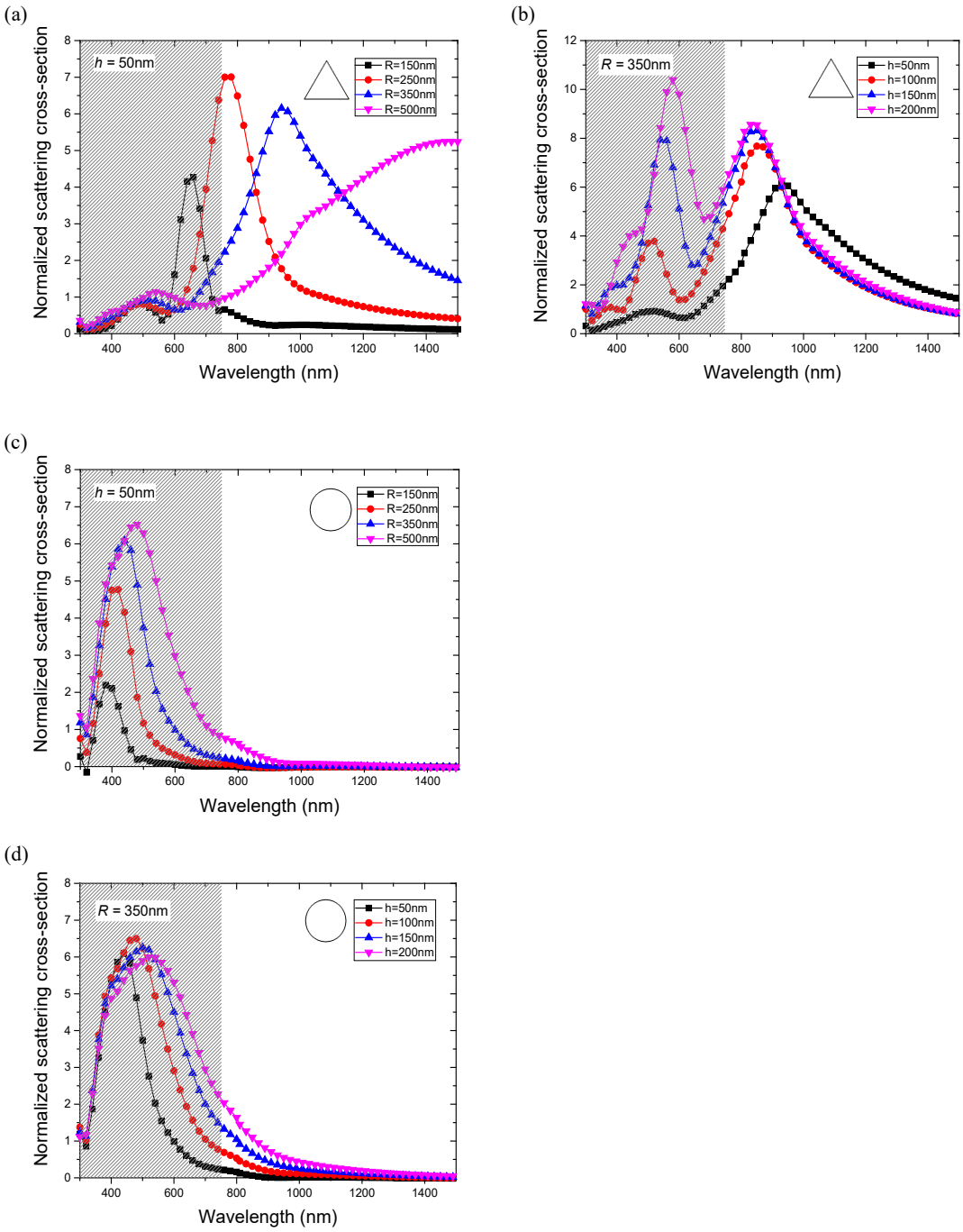

Figure 3.3.1 Scattering cross-sections of silver triangles (a and b) and spheres (c and d) scatterer. *R* is the radius of nanospheres in NSL and *h* is the deposited silver thickness. The metrics apply to the sphere array under the assumption that the volume of the plasmonic nanoparticles is not changed during annealing.

The optical absorption rates of the i-layers of the modeled nanoparticle enhanced plasmonic cells are shown in Figure 3.3.2 (R=250nm, h=50nm). The reference cell's i-layer absorption rate is also shown for comparison. The interaction between the incident light and silver nanoparticles on top of the cell is complicated, and therefore the absorption in silver nanoparticles is also shown in Figure 3.3.2 to better illustrate this interaction.

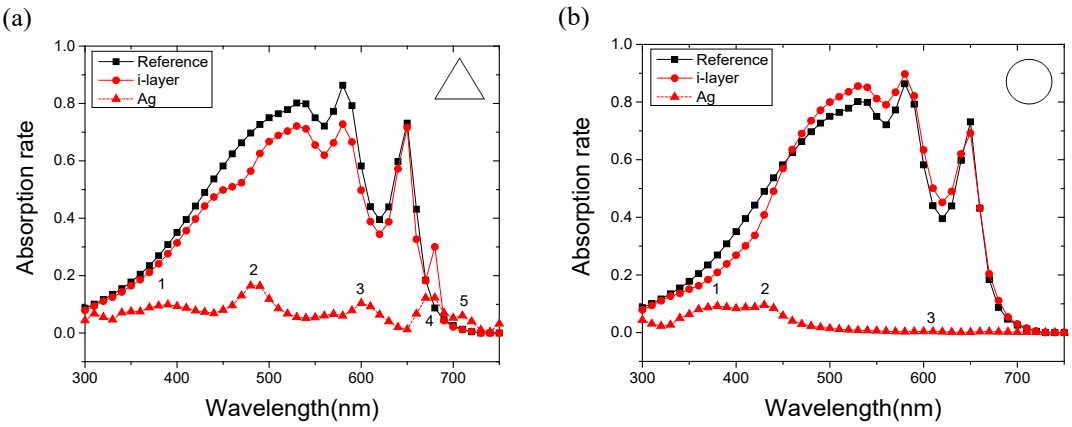

Figure 3.3.2 Absorption profile of the i-layer and silver particles for the triangle (a) silver nanoparticles array and sphere (b) silver nanoparticles array, assembled by NSL (R=250nm, h=50nm)

The absorption profile in the i-layer for the triangle array shows an overall scaling-down compared to the reference profile, clearly indicating that a triangle array of this geometry damages cell performance. A triangle array of this size and geometry is not able to provide a strong scattered field into the i-layer because the dipole scattering cross-section peak is out of the active wavelength range, hence there is not a significant scattering effect to increase absorption in the i-layer at relevant wavelengths for PV. While high order scattering falls in the active spectral regions, however, the scattering that stems from high order resonance is weak (Figure 3.3.2 a) and b) and not well-separated from the corresponding absorption, which competes with the i-layer and hence negatively contributes to optical enhancement. The high absorption rate in

triangle nanoparticles can be attributed to their anisotropic geometry, which concentrates and dissipates energy at the triangle tips. To characterize the near field effect and explore the room for optimization, the absorption profiles of the triangle nanoparticles was studied. Five absorption peaks are identified at 390nm 490nm, 600nm, 680nm and 710nm (Figure 3.3.2 a), with the plotted field distribution in the xy- and yz-planes corresponding to each peak, as shown in Figure 3.3.3.

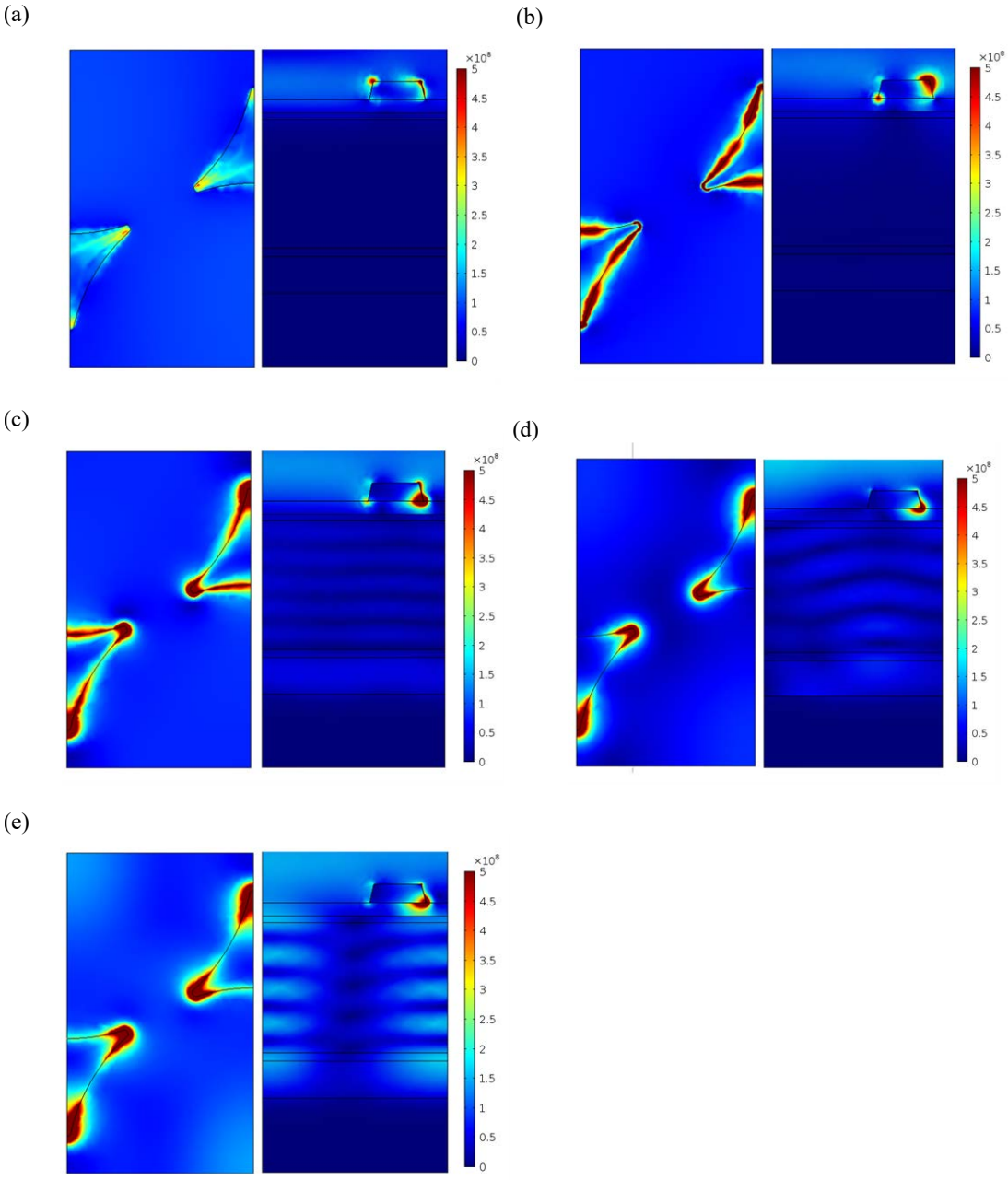

Figure 3.3.3 Silver triangle array electric field normal mapping at 390nm, 490nm, 600nm, 680nm, 710nm (a-e). The mapping is drawn at the xy-plane ($z=z_{triangle\_base}$) and the yz-plane (x=0), on the left and right respectively for each subset. Incident wave polarization in the y-direction

In Figure 3.3.3 a) and b), the field distribution across the triangles is found to be along the edges of the particle, whereas the distribution in c), d) and e) is mainly concentrated

on the tips. This concentration process becomes more prominent with different wavelengths. According to a recent study by Herr et al. the near-field enhancement (E/E_0) can reach up to 80 times at the triangle bowtie gaps[124]. In the yz-plane mapping, the distribution of the enhanced electric field is highly discrete, with multiple hot spots arising around the corners of the triangle. As previously discussed, the dipolar mode of triangles of this size occurs at 800nm, which is out of the spectrum being considered. The emergence of multiple absorption peaks comes from the high order modes and the interactions between them. Due to broken symmetry and the excitation of high order modes, a non-linear optical process and a second harmonious emission can occur at lower wavelengths[125]. Figure 3.3.3 a) and b) show that the enhancement of the near field tends to selectively reside on the edges, a typical sign of retardation, in which only a fraction of the triangle experiences the polarization[126]. In the red region of the electromagnetic spectrum, the enhanced near field is concentrated at the tips, which is more dipolar-like. Due to the blocking ITO layer and low carrier life time in the p-layer, the i-layer does not benefit from the near field enhancement; on the contrary, the excitation of those modes causes strong energy dissipation within the triangle. Consequently the triangle array is not an ideal scatterer for a-Si:H cells. It is worth noticing that in Figure 3.3.3, d) and e), the plasmonic resonance, coupled into the waveguide mode, leads to high order diffraction modes propagating within the i-layer. The small peak at 680nm confirms this analysis. The diffraction that occurs at 710nm is close to the absorption limit of a-Si:H, and the contribution to the enhancement is therefore negligible.

For sphere hexagonal arrays (R=250nm, h=50nm), three silver absorption peaks are identified at 380nm, 430nm 610nm, corresponding to octupole, quadrupole and dipole resonances respectively. Absorption in dipolar resonance contributes less than 1% of the total absorption, from Equation 3.1.1 and 3.1.2, and its corresponding scattering cross-section can be many fold greater than the absorption cross-section, which boosts a-Si:H absorption at longer wavelengths. The increase in i-layer absorption around 610nm supports this analysis. With the high order modes, resonance can be both

beneficial and detrimental. The field distribution snapshot at the xy-plane ($z=z_{sphere\_center}$) and the yz-plane (x=0) were taken and shown in Figure 3.3.4(a-d).

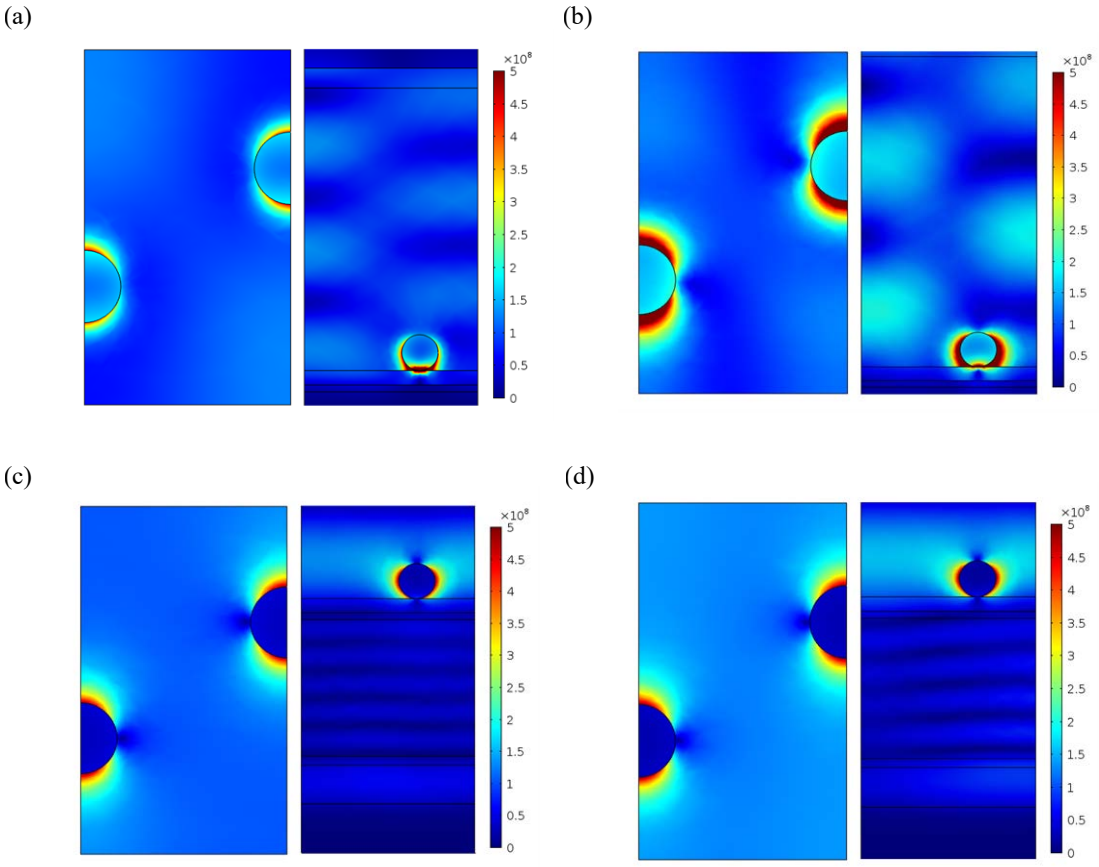

Figure 3.3.4 Silver sphere array electric field normal mapping at 380nm, 430nm, 610nm and 680nm (a-d). The mapping is drawn at xy-plane ($z=z_{sphere\_center}$) and yz-plane (x=0), shown to the left and right respectively for each subset. Incident wave polarization in y-direction. Sphere array fabricated by NSL using a nanosphere radius of R = 250nm, with deposited silver thickness h = 50nm.

As previously discussed, the separation of absorption and scattering in multiresonance modes can be beneficial if they are engineered to be absorptive outside the a-Si:H active region while scattering inside that region. However, to achieve this with NSL is difficult since the latter offers limited options in engineering the inter-particle spacing. In this case, the enhancement from 450nm to 580nm is gained from the useful

scattering originated from both dipolar and higher order modes resonance. The drawback at <450nm region is a consequence of high order modes absorption, where the enhancement becomes negative. Field distribution shows that the backward scattering/diffraction also causes the losses. Plasmonic coupling of incident light results in strong backward diffraction at both 380nm and 430nm (Figure 3.3.5 a) and b). Useful diffraction found at 680nm gives rise to a small bump in the i-layer absorption profile (Figure 3.3.5 d), but this is not as strong as the diffraction caused by triangle array at the same wavelength.

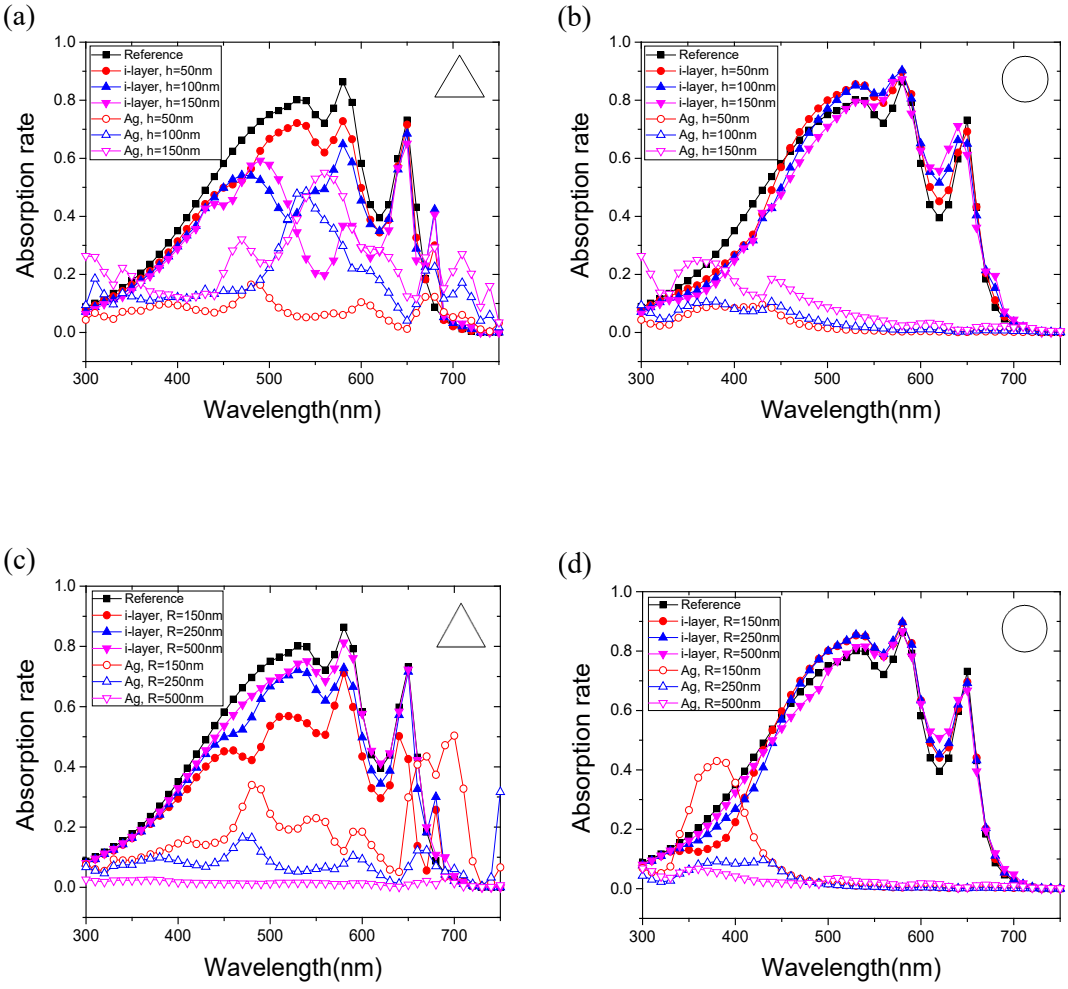

Figure 3.3.5 Absorption profile of the i-layer and silver nanoparticles for triangle (a,c) and sphere (b,d) arrays at *R* (150nm – 500nm) (a,b) and *h* (50nm – 150nm)(c,d)

Figure 3.3.5 shows the changes in the absorption profile as *R* and *h* vary. The behavior in the triangle array case is complicated and none of the results so far show a promising enhancement, compromising the cell performance rather than boosting it. Figure 3.3.5 a) shows the spectral sensitivity of the silver particle absorption. As can be seen in Figure 3.3.5 a), there are three major high order absorption peaks that red-shift with the increasing thickness as they all grow in strength. A greater thickness appears to require longer wavelengths of the incident wave to interact with the entire triangle structure, and the chances of creating an electric field gradient along the triangle pillar also increases, hence increasing the retardation effect. This explains the stronger, red-shifted higher order absorption peaks. The scattered field induced by high order resonance, though showing a significant increase from previous analysis, still cannot compete with the absorption. In addition to thickness, increases in *R* have the opposite effect: absorption peaks are pushed slightly towards red and the fraction of energy absorbed by particles is reduced significantly. For instance, the absorption profile of the triangle with *R*=500nm, *h*=50nm is nearly a flat line, with only weakly observable peaks. Although the corresponding i-layer absorption increases, this increase is not sufficiently significant to show enhancement when compared to the reference cell. The reason for this could be the increased reflection caused by larger triangles, which behave more like mirrors that reflect light out of the cell rather than scatter light into it. A closer analysis of the absorption rate shows the complementary characteristics between the i-layer and the nanoparticles, indicating that the absorption of nanoparticles is the main source of performance degradation. In the worst case scenario, the triangle array delivers an enhancement of -43% at *R*=250nm, *h*=150nm. The diffraction peak is subject to system symmetry and is hence located at 680nm regardless of triangle dimensions. The intensity of this peak, however, relies on the coupling of the plasmonic resonance in the nanoparticle, and it can therefore fluctuate with geometry, as observed in Figure 3.3.5 a) and c). In this series, the diffraction peaks are generally not strong enough to compensate the losses from the parasitic absorption in the triangles. More importantly, both solar irradiance and a-Si:H absorption are weaker at 680nm, therefore limiting the benefit from diffraction .

The sphere arrays show similar profiles as discussed for the R=250nm, h=50nm case. The sphere size is expressed in R and h for fabrication convenience, bearing in mind that the R and h themselves do not directly represent the sphere size, which is a result from annealing a triangle fabricated using R and h metrics. In the sphere cases, both R and h control the size, with R additionally also governing inter-particle spacing. The previous discussion has shown that large particles deliver more scattered light by supporting the excitation in high order modes. It is also observed that larger sphere sizes generally result in better overall optical enhancement (Figure 3.3.5 b). The sphere sizes should not be too large, however, or they will shield the a-Si:H underneath from sunlight. The sphere spacing is also important, as can be seen in Figure 3.3.5 d), where the absorption peak is significantly raised when the spheres are close to each other. The consequence of this is a decrease in the i-layer absorption at the same wavelength range. A well-separated sphere array shows mild absorption in high order absorption profiles despite an increased radius (Figure 3.3.5 d). Nevertheless, the overall influence of the nanoparticles is complicated, and trade-offs occur between better scattering and a lower shielding effects, leading to the optimization for R and h. It should also be noted that the diffraction peak in the sphere array is much weaker compared to its equivalent triangle array. One explanation of this phenomenon is that the support from surface plasmon polariton (SPP) spheres as the contact surface is far less when compared to the triangles, resulting in less coupling of the diffraction modes.

NSL-based solar cells allow for two degrees of freedom for optimization: the nanosphere radius R and the silver film thickness h. Smaller spheres are created by reducing the silver deposition time while keeping the R constant. Therefore, in the triangle array, the ratio of shaded area to the entire surface is constant and independent of R, while it can fluctuate with sphere arrays, whose coverage changes with both R and h. The optimization is performed to tune both h and R to maximize the performance of the solar cell. The absorption rate is integrated into the solar irradiance spectrum (air mass = 1.5) to obtain the optical enhancement, OE. Table. 3.3.1 shows the OE of modeled a-Si:H plasmonic-enhanced solar cells.

Table 3.3.1 AM1.5 solar irradiance spectra integrated optical enhancement (OE) for triangle and sphere arrays fabricated by various *R* and *h* combos.

R (nm)	*h* (nm)	OE_triangle (%)	OE_sphere (%)
150	25	-13.34	4.30
	50	-26.73	6.62
	100	-43.56	3.48
	150	-54.76	-8.75
	200	-60.24	-26.35
200	25	-10.10	4.80
	50	-18.38	7.22
	100	-35.00	3.09
	150	-48.05	-10.34
	200	-57.72	-27.37
250	25	-7.87	4.73
	50	-11.40	7.40
	100	-23.08	4.40
	150	-34.24	-4.86
	200	-43.61	-15.79
300	25	-7.32	4.19
	50	-9.12	3.46
	100	-15.86	-4.12
	150	-23.68	-11.51
	200	-27.19	-17.77
350	25	-6.43	4.71
	50	-7.09	2.88
	100	-11.24	-7.26
	150	-15.02	-14.37
	200	-16.93	-19.52
400	25	-5.73	4.85
	50	-5.76	3.94
	100	-8.00	-6.14
	150	-13.95	-15.47
	200	-17.36	-22.15
450	25	-5.48	4.30
	50	-4.51	4.42
	100	-4.89	-1.00
	150	-10.07	-6.26
	200	-13.96	-10.25
500	25	-5.47	1.88
	50	-4.98	1.50
	100	-4.72	-0.45
	150	-9.01	-2.51
	200	-11.41	-4.57

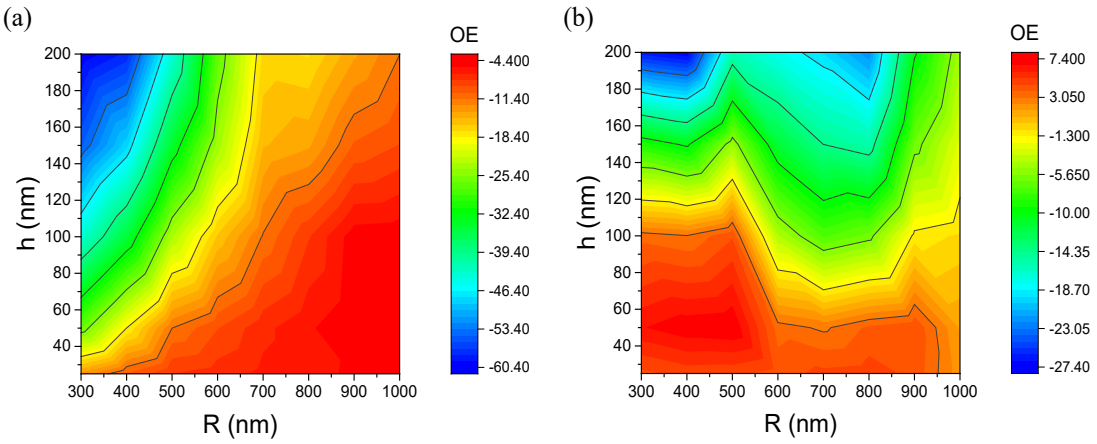

Figure 3.3.6 AM1.5 solar irradiance spectra integrated optical enhancement (OE) contours plot against *R* and *h* for triangle (a) and sphere (b) arrays.

As can be seen in Table 3.3.1, there is no positive OE observed for triangle arrays with any of the investigated parameters. From previous near field analysis it is clear to see that enhanced field is strongly localized at triangle hot spots like edges and tips. The absorption profiles indicate the energy is absorbed and dissipated as heat rather than causing useful diffraction or scattering. The greater the thickness, the larger the surface area that creates hot spots, as can be seen from Figure 3.3.6 a) As such, given the nanosphere radius *R,* OE losses increase with the silver film thickness, *h.* Simultaneously, at a constant *h,* larger nanospheres improve the OE but do not elevate it to above zero. Absorption is drastically reduced when the nanoparticle size becomes comparable to the half-wavelength of light, with resonance peaks moving far to the infrared region and the useful scattering within the photo-active spectral range also being reduced. The large triangle array on top of ITO serves as a mirror, shading the cell from incoming sunlight. Hence, even when absorption is not a limiting factor in cell performance, the shading effect still cuts the cell performance. Figure 3.3.6 a) additionally shows that the effective shading is less harmful than the parasitic absorption in nanoparticles, as can be seen in the much more negative OE with the smaller nanospheres. For the sphere array, a useful enhancement of ~ 7% is crowded in the bottom-left corner in Figure 3.3.6 b), suggesting that smaller nanospheres with a

moderate silver thickness could produce the best results. Silver sphere particles that are too closely packed reduce the OE. This phenomenon could possibly be explained by large shading areas. For R = 150nm, h = 200nm, the effective coverage of silver particles reaches 20%, where useful scattering cannot compensate the shading losses. The absorption of the silver spheres rises significantly with larger particles, with R = 150nm, h = 200nm the absorption peaks, showing 60% of the incident energy are absorbed by the particles. Destructive interference between scattered fields is another reason for reduced enhancement. In Figure 3.3.4 b), a distorted near field is observed, indicating the excited near fields at the sphere gaps are repelling each other. Although using larger nanospheres lessens this parasitic absorption, the overall enhancement is not as prominent as with smaller nanospheres. To sum it up, the highest OE obtained in this series simulation is 7.4 %, with R = 250nm, h = 50nm.

Although there is enhancement with the nano sphere patterned array on a realistic i-layer thickness, it is limited and not as great as the percent increase observed in artificially thin plasmonic cells reported in the literature[56,61]. The cell performance here is plagued by the triangle absorption, as have been discussed by Sherry et al[127]. Radiative damping grows significantly with the particle size. For the nano triangle arrays with heights smaller than 25nm, the radiative damping is low and not able to compete with scattering, thus the emission dominates over absorption. With increases in particle sizes the absorption rate is comparable to the light emitting rate. As Morarescu added, the aspect ratio of the triangles also plays an important role that affects the localized surface plasmon modes[112]. A good agreement with this observation can be found in Figure 3.3.5 c). Clearly for the given spectrum range, the absorption is drastically diminished by increasing the aspect ratio. For R=500nm, h=50nm, the nano triangle absorption profile is flattened to be less than 5 percent throughout the spectrum. The sphere arrays, on the other hand, demonstrate greater capability to scatter light than the triangles. More importantly, the scattering cross-section of sphere spectrally overlaps the a-Si:H absorbing region, the scattered light is more effectively contributes to a-Si:H absorption.

Surface patterning is a balance of art and also the key to access plasmonic enhancement. Although NSL offers scalable and inexpensive fabrication, it comes at the cost that the flexibility of patterning are limited. Hexagonal arrays are the only possible outcome from a naturally close-pack structure, leaving little room to the variation in symmetry. Despite the fact that non-closed packed structures are made available through NSL [74,128,129], they are not the naturally occurring configuration and thus require additional techniques to assist fabrication, such as employing a template[129]. Those add-on techniques challenges the motivation to keep the low-cost production possible via NSL. Because of the limitation, the enhancement that can be extracted from the structure is not as good as the state-of-art plasmonic a-Si:H cell[61]. However, it does open a gate for plasmonic a-Si:H to be commercialized.

In this study the two conceptual geometries that can be easily accessed from NSL template are modeled to prove the concept of plasmonic enhancement from hexagonal array scatterer. The result shows clearly how geometry difference can influence plasmonic enhancement, and prove that with the same symmetry, particles with irregular shapes are not ideal scatterer for plasmonic application. Nevertheless, NSL is a versatile method supports a variety of other geometries and patterns that is not covered in this research. It is necessary to continue the work with other possible geometries or patterns such as nanocone, nanodots, nanorings, nanopillars which are proved to be NSL-compatible. Moreover, selective etching by RIE is commonly implemented to adjust the nanosphere sizes. By reducing nanosphere sizes, the silver nanoparticles are able to form a connected silver network that greatly improves the top contact conductivity. This could be extremely useful to compensate the poor conductivity in ultra-thin ITO. A thinner ITO with silver nano network that delivers equivalent conductivity can in turn benefit plasmonic scatterer by narrow down the distance to the active layer. Last, the exact anneal geometry of silver nano triangle is related to the surface wettability and surface tension of silver on ITO, which can vary with the ITO quality. Experimental work is required to validates the geometry and prove the enhancement.

3.4. Conclusion

In this study, the plasmonic effect of triangle and sphere silver nano arrays fabricated using NSL techniques have been studied in detail on a-Si:H solar cells. Scattering from the silver triangle and sphere arrays deposited on top of conducting ITO layer produce completely different cross-section profiles. Well-separated resonant modes are identified in triangle arrays, with substantial red-shifts found as the triangle spacing increases. At the same time, the thickness of the silver film tends to overlap two primary resonance peaks into a broad peak when increased to above 200nm. Scattering from higher order modes increases substantially with greater silver thickness, whereas dipole peaks are less affected. Cross-sections in sphere arrays show a continuous, broad peak across the main absorbing spectrum from 300nm to 700nm, and the peaks further extend to infrared as the spheres become larger. The broad scattering cross-section peak observed is a combination of multiple resonance modes that are not well-separated at the UV-visible range. For solar photovoltaic applications, the sphere arrays are more beneficial when generating broad scattering peaks than their simulated triangle array counterparts.

Plasmonic-assisted cell performance has been investigated in numerous simulations. The factors affecting cell performance include absorption, the shielding effect, diffraction, and scattering. In the triangle array, the parasitic absorption of the silver particles proves to be problematic, and although it can be alleviated by increasing the particle spacing, no useful enhancement was observed in the triangle arrays that were simulated. Sphere arrays, on the other hand, can be engineered to be advantageous to PV performance. Broad scattering cross-sections from the spherical particles create useful scattering fields at certain sizes and spacing. For the simulated sphere arrays the highest enhancement found was 7.4%, which was fabricated with a 250nm radius nanosphere and a 50nm silver thickness, followed by annealing in inert gas. These results are promising and provide a path towards the commercialization of plasmonic a-Si:H solar cells using cheap and scalable NSL fabrication techniques.

4. Hexagonal plasmonic array enhanced a-Si:H solar cell[1]

4.1. Introduction

Light trapping in thin film hydrogenated amorphous silicon (a-Si:H) solar photovoltaic (PV) cells is necessary to compensate the reflectance caused by reduced cell thickness, especially in the red region of the spectrum where the cell generally has poor absorption [8,130]. Light trapping is commonly obtained with antireflection coatings or top/back electrode texturing [23,131–133]. Light is scattered at a distribution of angles, increasing the optical path length and thus the probability of absorption in the i-layer generating electron hole pairs. Unfortunately, random texturing increases roughness in the contact surface area, which consequently increases the surface defects and the concomitant recombination sites. The highest conversion efficiency achieved by a random textured surface a-Si:H cell is 10.1% [134,135]. Recently, plasmonic nanostructures have offered a potential to improve optical enhancement [53,77,136,137]. Nanopatterning at top contact or back reflectors create a periodic structure that can couple the light into guided modes [32,54,77]. Tan et al. implemented a plasmonic back reflector with self-assembled Ag nanoparticles onto the back-contact/a-Si:H interface. They compared the cell with the state-of-art random textured cell and observed 2 mA/cm^2 gain in photocurrent and the open circuit voltage has been kept at the same level. The high efficiency can be attributed to dramatic light trapping by strong scattering at the interface[55]. For periodic structures, other metallic structures are possible. For example a nanodome resonator used as back reflector can absorb 94% of the light with wavelengths of 400-800nm, which is significantly higher than the 65% absorption of flat film devices [138]. However, the back reflector scheme inevitably creates a texture/pattern base, which the rest of the cell has to be built upon. Therefore, all interface above are patterned or textured, and the contact area at interfaces are well-enlarged compared to flat surface, which can contribute to surface

[1] This chapter is submitted as "C. Zhang, Jephias Gwamuri, Sandra Cvetanovic, J. D. O. Guney , J. M. Pearce."Enhancement of Hydrogenated Amorphous Silicon Solar Cells with Front-Surface Hexagonal Plasmonic Arrays from Nanoscale Lithography" to *Solar Energy Materials & Solar Cells*

recombination. This creates a tradeoff between optical gain and electrical degradation, which is difficult to remove with back contact cell designs [139–141], however it can be easily overcome with front contact plasmonic geometry[31,33,37,105,142,143].

To exploit useful scattering and diffractions while keeping the parasitic absorption low, plasmonic nano patterning must be carefully controlled by tuning the morphology. Techniques suitable for wafer-scale fabrication (e.g. UV-lithography[144], e-beam lithography[145,146] and focus ion beam[147–149] are too expensive for commercial use of large scale PV areas. Nanosphere lithography (NSL) has progressed significantly is promising to overcome this cost challenge[108]. NSL in combination with vertical evaporation tools creates a hexagonal array made of curved triangles, the dimension and spacing of the triangle can be controlled continuously by the nanosphere used in NSL. Specially,

$$a = D/2 \tag{4.1.1}$$

$$d_{ip} = D/\sqrt{3} \tag{4.1.2}$$

where D is the diameter of NSL bead, a is the edge length of nano triangle and d_{ip} is the interparticle spacing defined by the distance between the centers of two neighbor triangles.

To achieve a uniformly patterned nanosphere monolayer with less defects, spin coating and interface coating the two common approaches that has high yield and produce colloidal mask of high mechanical strength. In Chapter 2. The details of each methods have been discussed and each has the advantage for a specific beads type and size. In this study the interface coating serves as the main fabrication techniques to create nanosphere monolayer. Amorphous silicon thin film cells are fabricated on a glass substrate with 3mm thickness. Such thick substrate will not be attached firmly to the spinner's sample holder via vacuum during high speed rotation, thereby the infeasibility to use spin coating for smaller nanospheres. Interface coating, on the other hand, allows all kinds of substrate regardless of type or thickness, enabling plasmonic structure to be deposited on cell based on glass, silicon or plastic materials. As

described in Chapter 2, for smaller nanosphere, monolayer uniformity highly relies on the introduction of anion surfactant, sodium dodecyl sulfate (SDS), which releases the surface tension and glue together the nanospheres. The surfactant residuals can be effectively purged from coated wafer by gentle ultrasonication in toluene.

In Chapter 3, a systematic study has been complete in searching for the fabrication parameters that maximize the enhancement using triangle or sphere hexagonal array. The results show that the sphere array yield up to 7.5% optical enhancement using nanosphere radius of 250nm and silver film thickness of 50nm. In this chapter, the detailed fabrication will be present step by step to complete the plasmonic nanostructure patterned a-Si:H cell. Upon completion, the cell is tested using solar simulator to obtain characteristic quantum efficiency (QE) and current-voltage (I-V) profiles. Comparison of both triangle and sphere array based cells, as well as the uncoated reference cell will be analyzed and discussed in detail to map the enhancement to its physical origin. The conclusion will be made on the discovery and future work will be outlined for continuous study in this field.

4.2. Methodology and implementation

4.2.1. Preparation of reference a-Si:H cell

Si:H cell samples were deposited using a load-locked RF (13.56 MHz) PECVD cluster tool reactor (MVSystems.Inc) onto 6” × 6” borosilicate glass substrates. The glass substrates were pre-cleaned in an ultrasonic bath and air dried in nitrogen gas before being sputter coated with a back reflector (BR). The BR and subsequent device layer were deposited following a recipe described in reference [150] to obtain a device structure shown in the Fig 3.2.3. The device fabrication was done using the same equipment and the processing parameters detailed in the same reference above.

4.2.2. Top side plasmonic hexagonal array fabrication

1. Complete reference a-Si:H cell is rinsed in ultrasonic bath with deionized (DI) water for 40 minutes, followed by drying in nitrogen flow. The cell is then stored in a desiccator before any further processing operations.
2. Nanosphere lithography is implemented using polystyrene nanosphere with interface coating as described in detail in Chapter 2. Two types of nanosphere with radius of 250nm and 500nm are employed to provide contrast according to simulation results in Chapter 3. Coated samples are allowed to dry naturally in room temperature and stored in desiccator.
3. Silver film evaporation is processed in Frederick e-beam evaporation system. The coated samples are attached to a metal plate which is mounts on the e-beam tool sample holder. Film deposition can be controlled by electron beam current. Here a small current of 0.075 A is used for good film quality, leading to an evaporation rate of approximately 12 nm/min. The film thickness is monitored in a calibrated thickness monitor. For testing, the sampled film thickness are 25nm, 50nm and 150nm, and for each thickness three cells are processed in parallel with one additional cell covered by copper foil. The covered cell will go through the evaporation but not receive any silver, it only uses as a reference. The process is carried out under base pressure at about 1.6×10^{-7} Torr.
4. After the cell is unmounted from the e-beam holder, they are immediately rinsed in toluene in an ultrasonic bath for 5 minutes. The process removes the bead as well as other organic residuals. The silver coated on top of nanospheres is also removed with the beads.
5. Annealing of the sample are carried out in a tubed furnace under Ar flow. The temperature is set to be 150 ˚C, which has been tested not to harm the cell. Annealing takes 3 hour. The time is optimized to have reasonable throughput yet not to be too long to degrade the cell. A surface thermometer

is inserted with the cells to collect the real temperature. Ar flow prevents all oxidization for nitrification from happening during the process.

6. For transmission spectroscopy analysis, the same triangular and annealed triangular array are deposited on top of soda lime glass. NSL nanospheres are removed by ultrasonic rinse in toluene for 5 minutes.

4.2.3. Plasmonic hexagonal array characterization

1. All samples are imaged for morphology analysis and film quality using a Hitachi S4700 field emission scanning electron microscope (FE-SEM) and a Veeco Dimension 3000 Atomic force microscopy (AFM) with cantilever tips (Tap300Al-G) on a 1:1 acquisition aspect ratio. For FE-SEM, the accelerating voltage is set to be 5 kilovolts and images are taken using lowest scan rate for quality concerns. For AFM, the field view was 2.5μm for R=250nm bead and 5μm for R=500nm bead respectively at 512 pixel width and scans performed at a speed of 0.5 Hz.
2. In addition to morphology characterization, localized surface plasmon resonance (LSPR) modes are identified using transmission spectroscopy. Specifically, silver nanoparticles are deposited on soda lime glass substrate with a refractive index of 1.55 and is scanned using a elliptical spectrometer (J.A Wollam Co UV-VIS V-VASE with control module VB-400) in transmission modes. The same is scanned from 300nm to 1500nm in a dark room. For each sample the scan is taken at three different places. Transmission spectrum is obtain for plasmonic peak identification.
3. The images are analyzed with ImageJ v1.48 for size distribution, perimeter and area measurement as well as circularity calculation

4.2.4. Device characterization

1. Solar cell external quantum efficiency (EQE) is measured in a PV Measurements QEX10 without bias in the range 300-800nm using a light source that is calibrated by a standard silicon photodiode. The beam is cast through a 5 x 5mm^2 hole that is well-defined to cover the circular a-Si:H solar cells A reference standard photodiode is used to calibrate the system and the QE is taken with two probes placed at the edge of the cell to minimize shading.
2. The I-V characterization is implemented in a Keithley 4200-SCS Semiconductor characterization system with solar simulator calibrated to deliver one sun power with AM1.5 solar irradiance spectrum. The cell is set in forward bias diode configuration. The light shutter is closed immediately after the measurement to prevent any induced cell degradation, i.e. the Staebler-Wronski Effects (SWE)[8,96,151].
3. For both QE and I-V measurement, each cell is measured three time to obtain an average performance.

4.3. Result and discussion

4.3.1. Plasmonic triangle and sphere hexagonal array validation

The SEM image of triangular silver nanoparticle patterned on top of ITO are shown in Figure 4.3.1. The images shows clearly the well-separated Triangular silver nanoparticle assembled into a particle array with C_6 symmetry. No observable agglomerates or oversized nanoparticle is found throughout the entire surface. The averaged surface coverage of nanoparticles is calculated by taking the ratio of nanoparticle area to the area enclosed by the red triangle mark in Figure 4.3.1 a) at five different place. Calculated average coverage is 7.1%, which is 23% smaller than theoretical coverage (9.3%). The nanoparticles preserve the hexagonal pattern with great uniformity, no distorted or damaged particles are found from SEM images.

However, there's about 5% connected triangle bowties. As pointed by Herr et al, the near field can be altered drastically by changing the distance between two bowtied triangles[124]. The effected of connected triangles are remains to be examined in cell characterization. Figure 4.3.1 c) shows the three major defect types: interstitials, vacancies and grain boundaries (marked on Figure 4.3.1c)). Interstitials are rarely seen in the image and can be removed completely by a prolonged ultrasonic washing period. The interstitials comprise less than 0.4% through of the surface. There are about 2% vacancies coverage, most of the vacancies come from the beads triplets as shown in Figure 2.4.5 as a result of surface tension during the coating process, which can be reduced by adjusting the surfactant concentration. Grain boundaries has the largest coverage over other defects and they are hard to remove. Grains size are subjected to the engaging speed, beads concentration and surface tension which is difficult to improve. The largest defect free domain achieved is around 200μm^2, which is rarely reported by other groups.

Figure 4.3.2 shows the silver triangular nanoparticle array with silver thickness of 25nm and 150nm. There are more isolated nano triangles in D = 500nm group (a and b), while in D = 1000nm group, the fraction of connected triangles become larger and the tip to tip distance narrows, supporting a stronger near field under illumination. For thicker silver film, a bright contour shows up in each triangle, it appears to be the top surface of the triangle prism. However, due to the increased film thickness and the curvature of NSL beads, the growth of the triangle prism subjects to some sort of obliquities (c, d). In D = 500nm group the brighter contour are even narrower, indicating the structure is transforming from prism to a triangular pyramid, such transformation is not as prominent as it in D = 1000nm group. Using image analysis software, the area of the top of the prism is 81% for D = 1000nm and 57% for D = 500nm. In simulation the sloped and curved prism is modeled according to the observation.

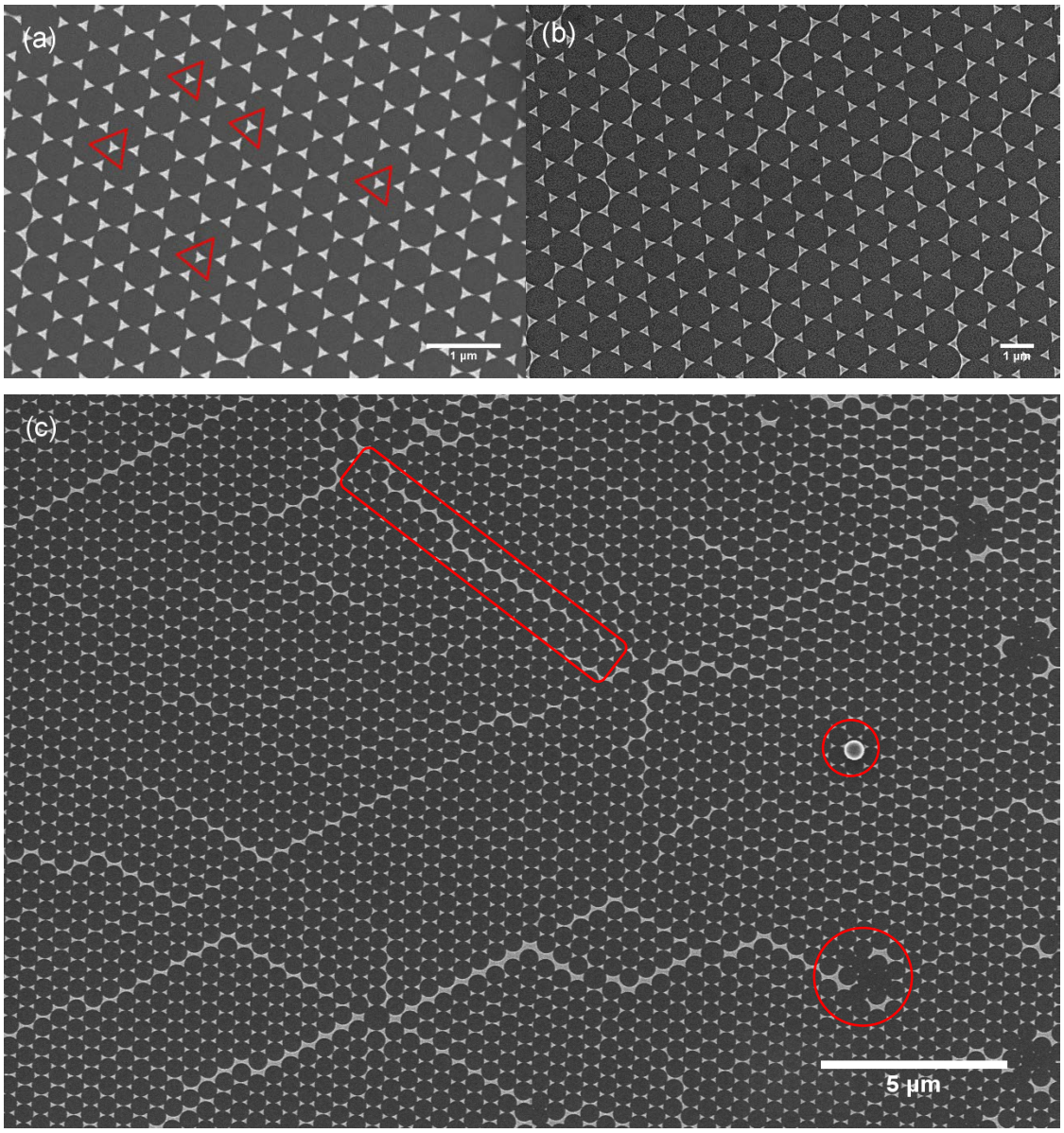

Figure 4.3.1. Triangular silver nanoparticle array with thickness of 50nm on top of ITO, fabricated by NSL using polystyrene nanosphere with diameter (D) of 500nm (a) and 1µm (b). (c) The same array as (a) in lower magnification.

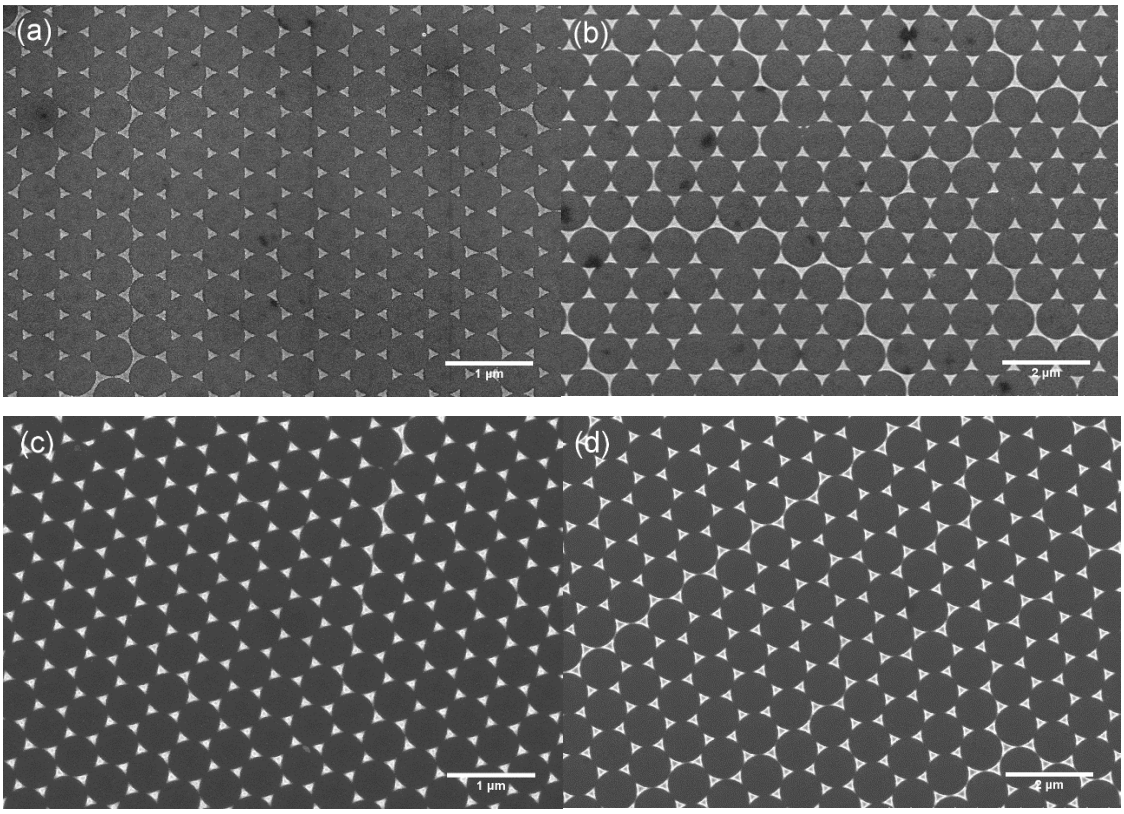

Figure 4.3.2. Triangular silver nanoparticle array with silver thickness of 25nm (a,c) and 150nm(b,d) on top of ITO. NSL nanosphere diameter of 500nm (a, b) and 1µm (c, d) are used in mask preparation

Annealed silver nanoparticle array are presented in Figure 4.3.3 and Figure 4.3.4. The annealing is carried out in a vacuum oven at roughly 150 ˚C. Temperature is monitored in real time using a surface thermometer. It can be seen that the shape of the triangular nanoparticle is altered completely. In the entire structure being examined no remaining nano triangles survived the annealing. They transformed to pseudo-spherical array while preserving the symmetry. Each annealed particle is fixed at the same position where the center of original triangular nanoparticle is, so that the inter-particle spacing and the C_6 symmetry are preserved. It should be noted that the transformation is not perfect, as one can distinguish that the annealed particle are not perfect sphere. Increasing the annealing time will increase the circularity, nevertheless the time must be kept as short as the cell can sustain. Size of the annealed particles also remain

constant as the triangle particle and there's a little variation due to the connected bowtie triangles, which give two slightly larger particle after annealing. The average in-plane diameter is 91nm with standard deviation of 10.4nm for silver thickness of 50nm using D=500nm NSL beads. Detailed size distribution of annealed particles are presented in Figure 4.3.5. For NSL beads diameter of 500nm, there are about 3% triangular nanoparticles split into two or three smaller nanoparticle during annealing in 1μm beads case. It can be understood that the splitting happens when the atoms in a nano triangle with a long and sharp tip starts to vigorously move to find new equilibrium positions. In Figure 4.3.4, the split of triangles become more prominent in D = 1μm, h = 25nm setup. Figure 4.3.4. b) inset shows a zoomed honeycomb unit, the annealing breaks down the relatively large triangular nanoparticle into smaller particles, three different types of break-down can be identified. First, the exterior of the triangle segregates from the triangle body and remains to be at the border, those particles are extremely small with typical average diameter less than 10nm, and they outline the border of original triangular nanoparticle in its place. In addition to the triangle border, the honeycomb unit border is also outlined by a group of larger particles, those particles can be considered as a result of triangle tip break down during annealing, hence they are distributed along the edge of the honeycomb. The largest particle is at the center of the original triangle, this is where most of the triangle's silver is after annealing. The interparticle spacing and symmetry of the array do not change after annealing, indicating the particles are in the same position before and after annealing. The split particle does not present in D = 1μm, h = 150nm case, which, however, shows rounded triangular shaped particles, a sign of incomplete annealing. Insufficient annealing time and temperature can cause the remaining triangles. Also when the particles become larger, longer time and temperature it demands for shape transformation. However, further increasing temperature will inevitably cause cell degradation. The effort remains to have a prolonged annealing time to better shift the triangle into spheres. For D = 500nm, the split and insufficient annealing is not as server as in D = 1μm cases, the annealed particles have overall good circularity and distribute normally.

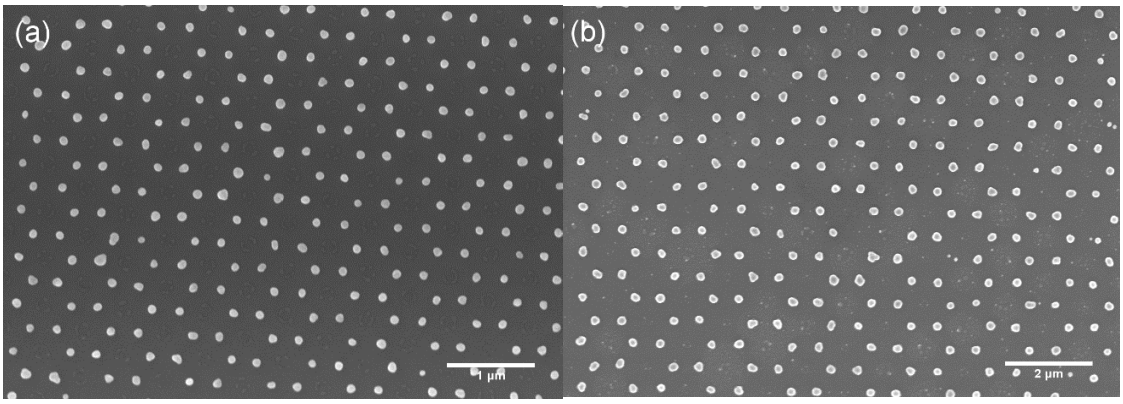

Figure 4.3.3 Annealed silver nanoparticle array on top of ITO fabricated by NSL using polystyrene nanosphere D = 500nm (a) and 1µm (b), silver thickness before annealing is 50nm. Annealing completed at 150 ˚C in vacuum for 3 hours.

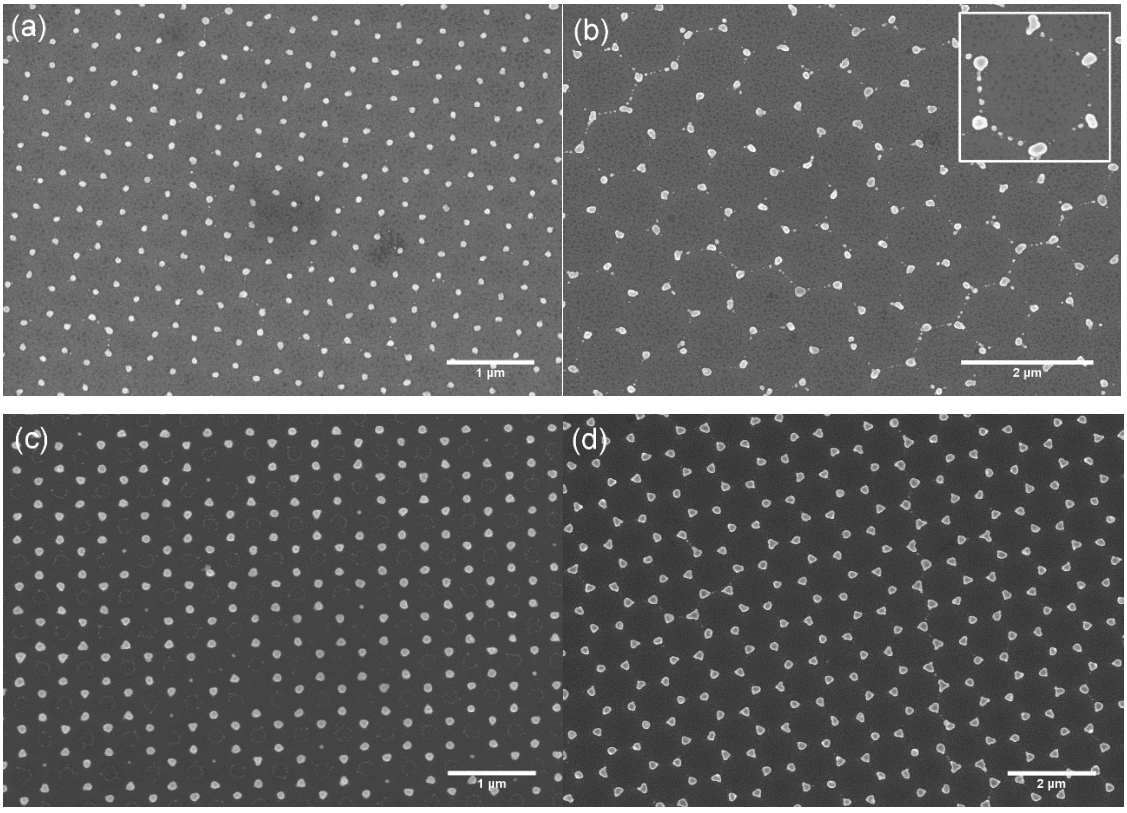

Figure 4.3.4. Annealed silver nanoparticle array on top of ITO fabricated by NSL using polystyrene nanosphere D = 500nm (a, b) and 1µm (c, d), silver thickness before annealing is 25nm (a, c) and 150nm (b, d) respectively. Annealing completed at 150 ˚C

in vacuum for 3 hours. Inset in (b): zoomed hexagonal array showing a honeycomb unit.

Annealed particles size distribution is plotted in Figure 4.3.5. For D = 500nm cases, regardless of the silver thickness, most of the particles follow a normal distribution pattern. Averaged particle diameter increase with silver thickness. For D = 1μm cases, the h = 50nm and 150nm cases has normal distribution with median at 190nm and 208nm. The h = 25nm is not normally distributed. Particle split and insufficient annealing time could be the two reasons that causing the abnormities in size distribution and deviation from spherical geometry.

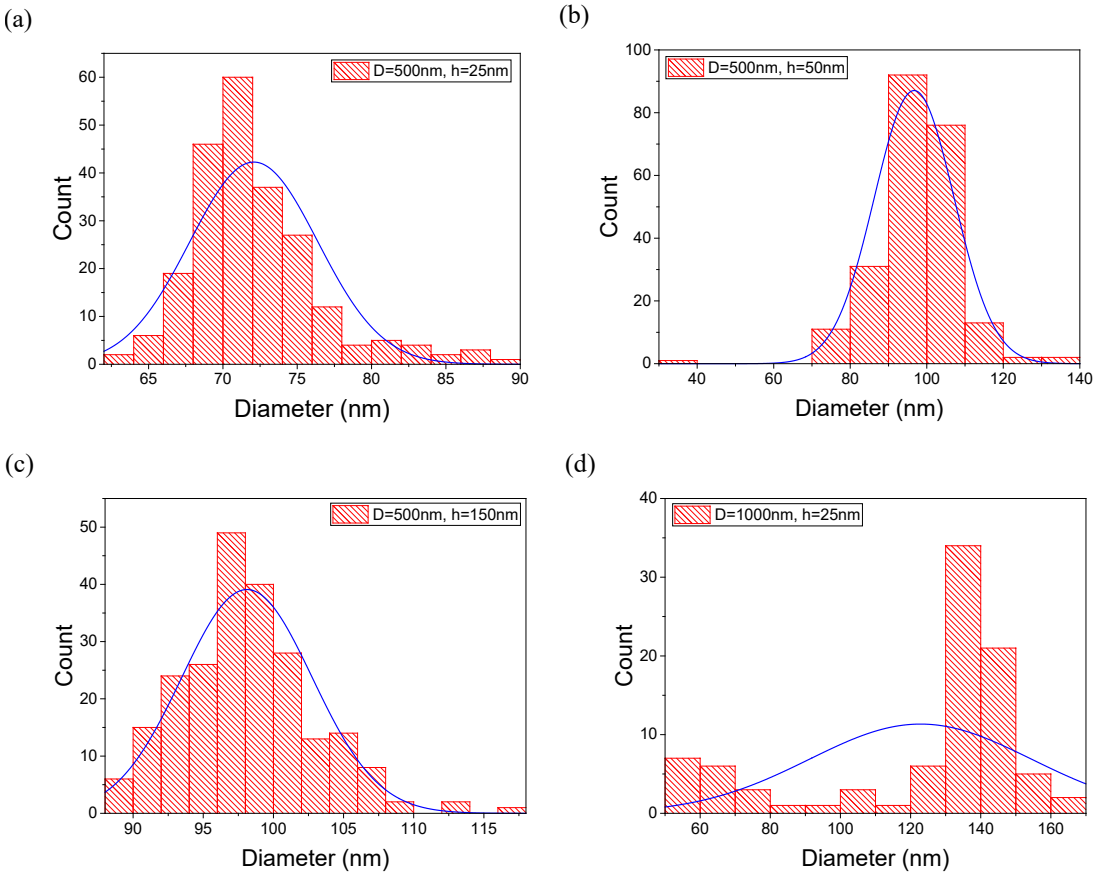

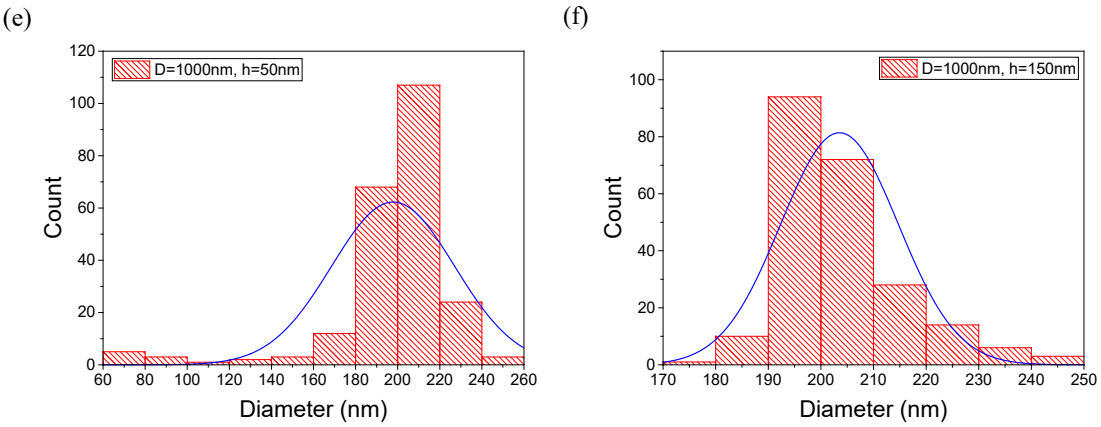

Figure 4.3.5 size distribution of triangular particles and annealed particle using NSL bead D = 500nm (a, b and c) and 1μm (d, e and f), deposited silver thickness of 25nm (a, d) 50nm (b, e) and 150nm (c, f).

To better understand the similarity between annealed particle and spherical particle and to anticipate the possible discrepancies between theoretical simulation and experimental results. The particle circularity is calculated using the following equation [152]

$$circularity = \frac{4\pi \times particle\ area}{particle\ perimeter^2} \tag{4.2}$$

Calculated circularity are summarized in Table 4.3.1.

In addition to circularity, the vertical thickness is also important to validate the spherical structure. AFM images are taken for a vertical section analysis to obtain particle vertical thickness. Figure 4.3.6 shows a section analysis configuration example. The distance secured by the two red marker on the image is sampled in the analysis. For each annealed particle array the sampling are taken at five different places in order to get averaged result.

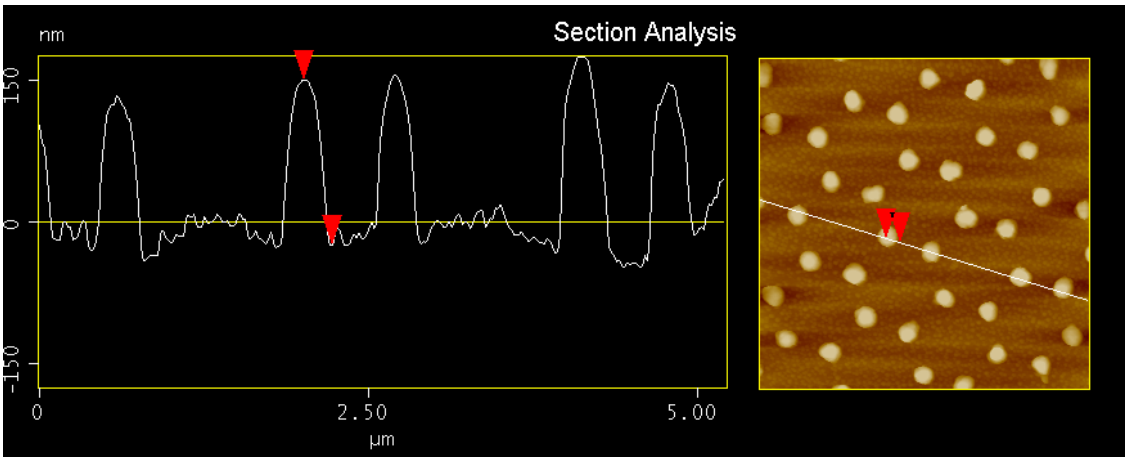

Figure 4.3.6 Annealed silver nanoparticle array section analysis configuration

Table 4.3.1 Average diameter, height and circularity of annealed silver nanoparticle. D and h are the diameter of NSL masking beads and thickness of deposited silver respectively.

D (nm)	h (nm)	Ave. diameter (nm)	Ave. height (nm)	Ave. Circularity
500	25	78.22	71.95	0.86
	50	95.57	86.66	0.86
	150	105.04	92.82	0.88
1000	25	134.84	68.73	0.79
	50	187.66	117.01	0.91
	150	219.30	174.46	0.76

Figure 4.3.7 shows the compared calculated and measured diameter of annealed silver particle. For both D = 500nm and D = 1000nm cases, the measured diameters fall in between the diameters of calculated perfect sphere and hemispheres. It can be inferred from the figures that the annealed nanoparticle is a bell-shape hemisphere. For h = 25nm and 50nm cases, the annealed nanoparticle is close to sphere for D = 500nm and

to hemisphere for D = 1000nm. The thicker silver triangle tends to have a much smaller diameter after annealing. For both D = 500nm and 1000nm, with h = 150nm the annealed particles gives an average diameter of 93nm and 174nm respectively. Insufficient annealing may cause the shortened diameters of the annealed nanoparticles. The resultant particle is a tall bell-shaped trapezoidal prism with rounded tips.

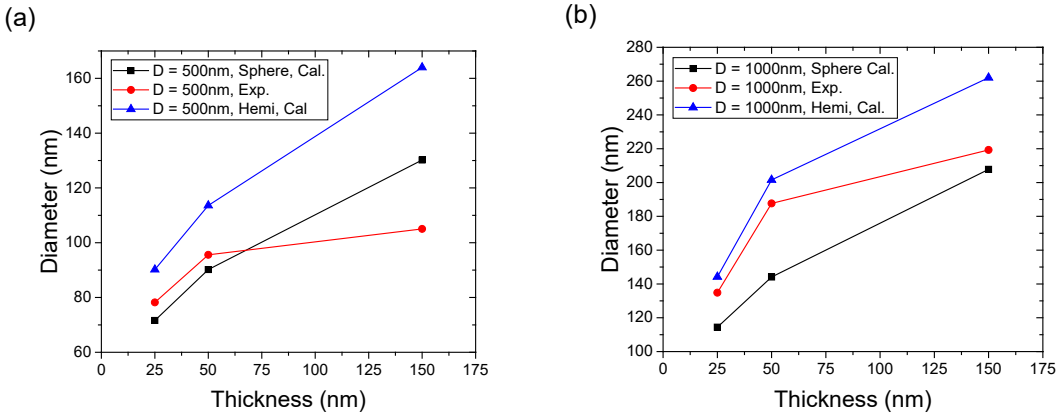

Figure 4.3.7. Calculated sphere (square), hemisphere (triangle) and measured (diamond) annealed silver nanoparticle diameter. Silver nanoparticle fabricated with NSL bead of diameter D = 500nm (a) and 1000nm (b).

Localized surface plasmon resonance (LSPR) can be visualized by the materials transmission spectrum. Each resonance mode is represented as a dip in the transmission spectrum. In order to obtain the spectrum, plasmonic array is deposited on a soda lime glass with refractive index of 1.55. One should notice that due to the difference in substrate permittivities, the dip position of LSPR observed in the transmission spectrum will not be as the same as the LSPR actually present on top of ITO in real solar cell. Nevertheless, transmission spectrum serves as an intermediate proof-of-concept approach, allowing directly identification of LSPR and approximate their behavior in real solar cell. Figure 4.3.8 shows the transmission spectrum obtained from a spectroscopy ellipsometer (J.A Wollam Co UV-VIS V-VASE with control module VB-400). In each case the scan ranges from 300nm to 1500nm to cover possible dips from UV to near-IR. Plasmonic triangular and annealed triangular array, fabricated

with NSL using parameters listed in Table 4.3.1 are deposited on soda lime glass substrate with a refractive index of 1.55. Molecular vibration absorption at near-IR are mitigated using Savitzky-Golay method with polynomial order of 2. It should be noted that the drop at <350nm is caused by the absorption of soda lime glass, not by the any type of resonance of the silver particles.

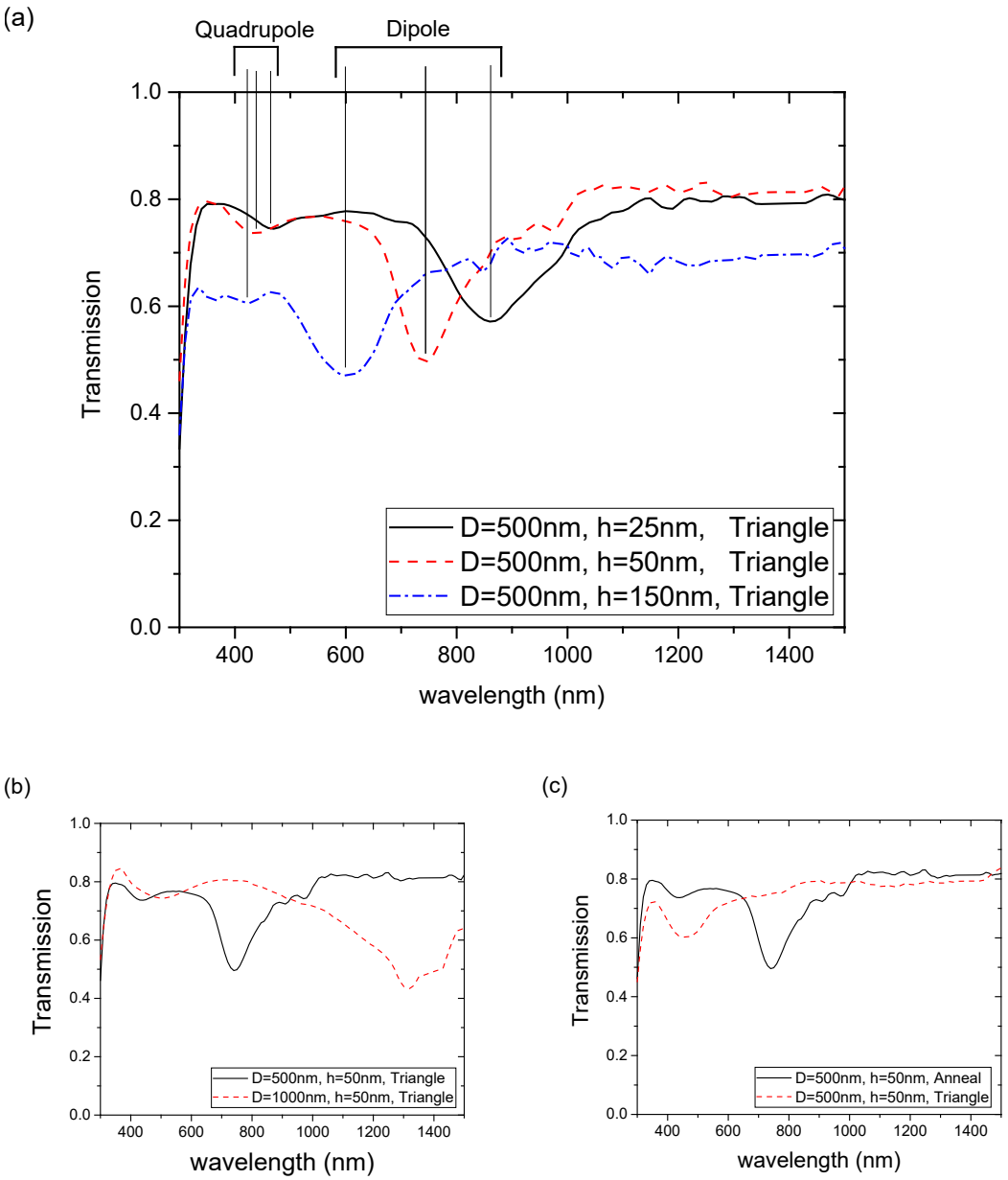

4.3.8 Transmission spectra of plasmonic array patterned on top of soda lime glass by NSL. (a) Triangular silver nanoparticles patterned using D = 500nm, h = 25nm (solid), 50nm (dash) and 100nm (dash-dot). (b) Triangular silver nanoparticles patterned using D = 500nm (solid), 1000nm (dash) and h = 50nm. (c) Patterned silver triangular (solid) and annealed (dash) array using D = 500nm and h = 50nm. D and h are NSL polystyrene bead diameter and silver thickness respectively.

For most of the transmission spectrums there are at least two dips showing in each of them. The dipolar resonance at longer wavelengths is caused by oscillation of electrons driven by light induced polarization, the origin of Rayleigh scattering. A dip with less strength and width can be observed at shorter wavelength, which is attributed to be the quadrupole resonance type. Quadrupole resonance is the next higher order resonance from dipole resonance. The origin of quadrupole and other high order modes can be understood by studying the inhomogenouly distributed field across a large particle, where incoming light can only partially polarize the particle[153]. Quadrupole and other high order modes can induced strong scattering and absorption, as have been discussed in Chapter 3. Proper engineering over the particle size can separate the parasitic absorption and scattering, letting the useful scattering to happen at the main absorbing spectral range while leaving the absorption outside.

Thickness effect. It is well known that the thickness of nanoparticles affect their plasmonic resonance. From Figure 4.3.8 a) it can be clearly seen that the both dipole and quadrupole resonance are subjected to a blue-shift as the silver thickness increases. As the silver thickness goes from 25nm up to 150nm, dipole resonance moves from 870nm to 600nm, quadrupole resonance, is relative insensitive to the thickness change, moves 480nm to 430nm. In 150nm case, aside the quadrupole resonance dip there's another dip at 390nm. We consider this dip as even higher order resonance which can only be seen with larger particles. This coincides with the discussion in Chapter 3. In fact, simulation shows more than 5 dips show up in the absorption spectrum, however, it is done on real cell structure where resonance by coupling back reflected light is considered. In this simple setup, the valleys in transmission spectrum mainly caused by angular distribution of scattered field and parasitic absorption. And many of the weak resonance dips are merged into a broader and stronger dip thus they didn't show up in the spectrum.

Spacing effect. Spacing between nanoparticle can be adjusted by using NSL bead of different sizes. Figure 4.3.8 b) shows two type of triangular array fabricated using D = 500nm and 1000nm NSL beads, all have the same silver thickness. The result is as

predicted in simulation: larger spacing results in larger particles hence the red-shift of the dips. Dipole resonance dips moves 560nm from 750nm to 1310nm, quadrupole moves 110nm, from 430nm to 540nm. The result is anticipated through simulation and discussed in Chapter 3 (Figure 3.3.5).

Shape effect. Through annealing, most of the triangular nanoparticles are transformed into spherical or pseudo-spherical nanoparticles. The sizes and distributions are analyzed and summarized in Table 4.3.1. Through the annealed particles are not completely spherical, they behaves significantly different from triangle particles and close to the sphere array simulation result. In Chpater 3 the scattering cross-section is of both types of array are discussed. The sphere array has the advantage over triangle array because of the merge of dipole and high order resonance modes, which gives a broad scattering cross-section overlaps with a-Si:H absorption range. The experiment confirms the overlapping of multi-order resonance dips, as only one dip from 360nm to 620nm is observed from the spectrum. This is similar to the scattering cross-section profile shown in Figure 3.3.1 with the same fabrication parameters. This also indicates the particle are sphere-like rather than hemisphere or cylinder, which have completely different scattering cross-section profile. On the other hand, the dipole resonance dip for triangular array occurs at 740nm, which is almost the end of a-Si:H absorbing range. The quadrupolar scattering could be useful, however, judging from the weak quadrupole dip in transmission spectrum, there's little scattered light propagating in the forward direction. In addition, the parasitic absorption of high order modes in triangular array also increases with thickness. Therefore it's hard to conclude the quadrupolar resonance of triangular array is beneficial.

In sum. The transmission spectrum gives an insight into the plasmonic resonance behaviors for each individual particle size. The plasmonic resonance is highly dependent on the thickness, spacing as well as the shape of nanoparticles. The analysis briefly shows that dipolar resonance of triangular nanoparticles are beyond 600nm, which is less useful in terms of a-Si:H PV applications, quadrupolar resonances remains to be examined in real cell as they induce both scattering and absorption, both

grows faster with the thickness of silver film. The promising candidate is the annealed array, which is proved to be more spherical than other shape or type. The observed dip positions are in agreement with the simulated result. Broad merged resonance is essential to useful scattering in a-Si:H absorbing region. The following cell construction and characterization will provide more detailed analysis on the triangular and annealed plasmonic structure.

4.3.2. Plasmonic hexagonal top contact cell performance

To better evaluate the light trapping of plasmonic hexagonal array, the external quantum efficiency (EQE) is measured without bias in the range from 300nm to 800nm using a light source that is calibrated by a standard silicon photodiode. The beam is casted through a 5 x 5mm^2 hole that is well-defined to cover the circular a-Si:H solar cells. Figure 4.3.9 shows the EQE profile of triangular and annealed nanoparticle array enhanced solar cells. Each figure shows three EQE curves for the same cell before metallic deposition, after the deposition but before annealing and after annealing. The cell without silver particle are employed as references cell. For the same cell the two electrodes are placed at roughly the same position for each measurement to minimize the discrepancies between individual measurements. It should be noted that due to the fabrication variations the quality of reference cells are not guaranteed (as can be observed from the figures). Comparing result in different groups or to the result from other labs are meaningless. The validation of the enhancement can only be done with the same cell before or after the implementation of plasmonic deposition/transformation.

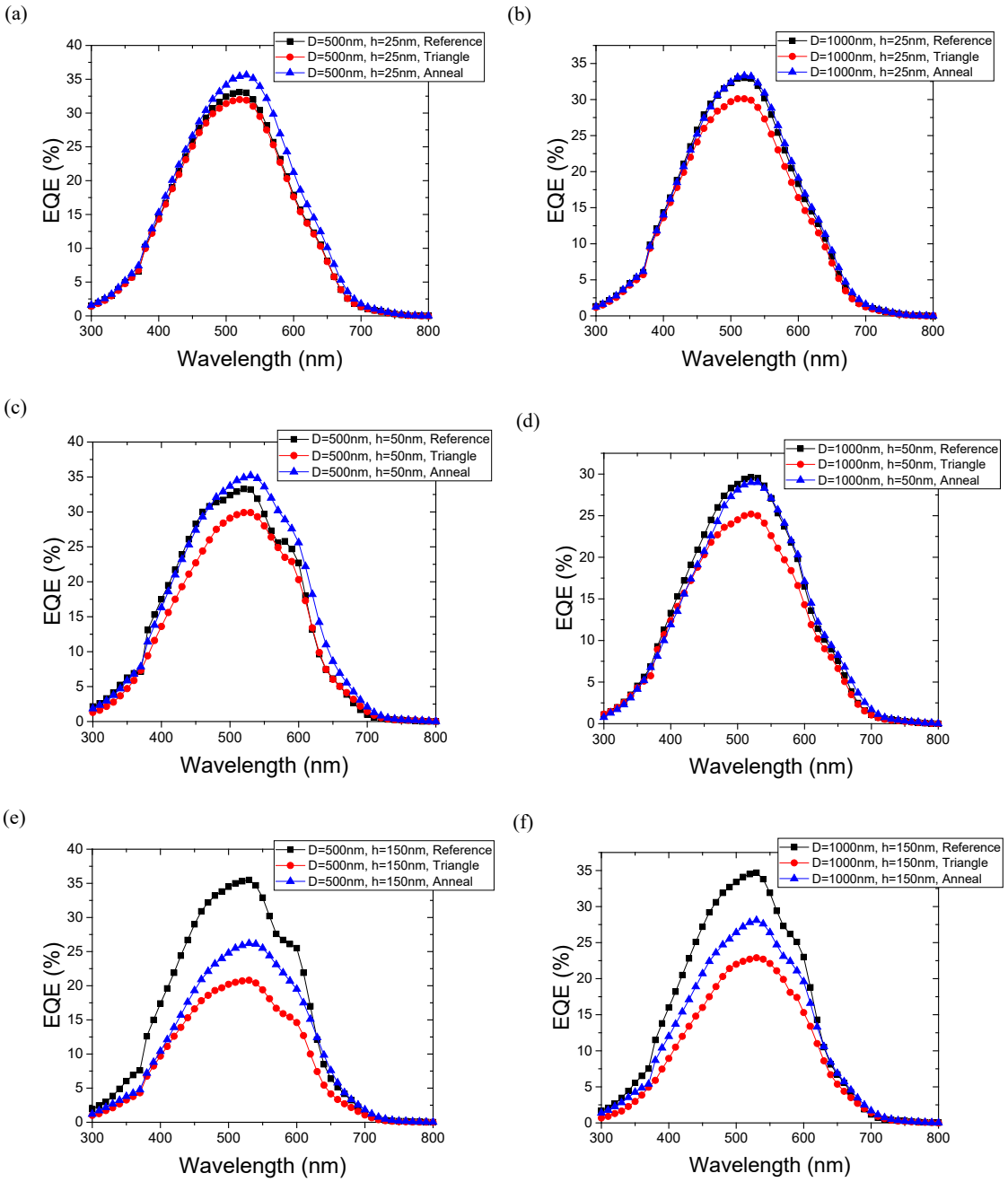

Figure 4.3.9. The measured EQE curves of reference (square), triangular (triangle) and annealed (sphere) nanoparticle enhanced a-Si:H solar cell fabricated by NSL mask with beads diameters of 500nm (a, c, e) and 1000nm (b, d, f), deposited silver thickness varies from 25nm to 1000nm as label in legend in each figure.

Starting from the 25nm group, just as predicted by the simulation, it is clearly observed a significant overall scale down of the curve in triangular nanoparticles for both D = 500nm and 1000nm cells. The parasitic absorption caused by hot spots in triangular nanoparticles is the major reason for the scale-down. For annealed arrays there's a scale-up from 450nm to 700nm in D = 500nm. This can be attributed to the scattering cross-section coverage over this spectral range. Although the calculated cross-section covers from 350nm to 700nm, the absorption and scattering is not well-separated at wavelength below 450nm, hence no significant scaling up or down at the shorter wavelength. With larger NSL bead, spacing between nanoparticles increases, the effective scattering albedo is not as large as it in D = 500nm cases, the result is less covered surface area by plasmonic induced scattering. The trade-off between forward scattering and absorptions causing the EQE curve is roughly unchanged compared to the reference. The same physics can be used to explain the h = 50nm groups. As can be seen in the field distribution in Figure 3.3.3, the energy dissipated at tips contributes a considerable loss in i-layer absorption. A larger spacing can reduce the absorption by lessening the near field, hence a measured increased EQE. The annealed arrays for both particle spacing benefit the cell by scattering from 450nm to 750nm, which is the source of the overall enhancement. No noticeable diffraction is observed from the curves. Further increasing the silver film thickness will cause problem to the cell. Figure 4.3.9 e) and f) shows both negative effect of triangular and annealed plasmonic array in D = 500nm and 1000nm. As discussed in Chapter 3, the larger particle absorbs consideration amount of energy to support high order modes resonance, and only a fraction of the energy is radiated through scattering. In addition, for larger particles, the light trapped by which has a larger change bouncing between the nanoparticles instead of being absorbed by the active layer. Absorption and shielding are both amplified with larger particles, therefore more negative result is expected. Throughout the tested cells there's no observation on diffractions peaks from 650nm to 700nm, which could be resulted from the weak coupling and broken symmetry in triangular and annealed films.

To better understand the EQE curve, the variation of reference cell before and after annealing should also be taken into consideration. Figure 4.3.10 shows the EQE curve of two sets of annealed reference cell. The cell is annealed in a vacuum oven for 6 hours to prevent any possible oxidation or nitration processes. It's obvious there's substantial influence of annealing temperature to the cell performance. Figure 4.3.10 a shows the before- and after-annealing line are overlapping, indicating no or less performance loss during annealing at 150 ˚C. However, in Figure 4.3.10 b), it is found significant decreased EQE over the entire spectra, with a maximum degradation of 30.4% at 520nm. Annealing at 200 ˚C may possibly cause the nucleation process in the ultrathin ITO layer, hence raise the sheet resistance at front contact. The 150 ˚C annealing that is used for EQE and I-V measurement causes only 1.1% discrepancy, which can be considered to be safe for such type of measurement.

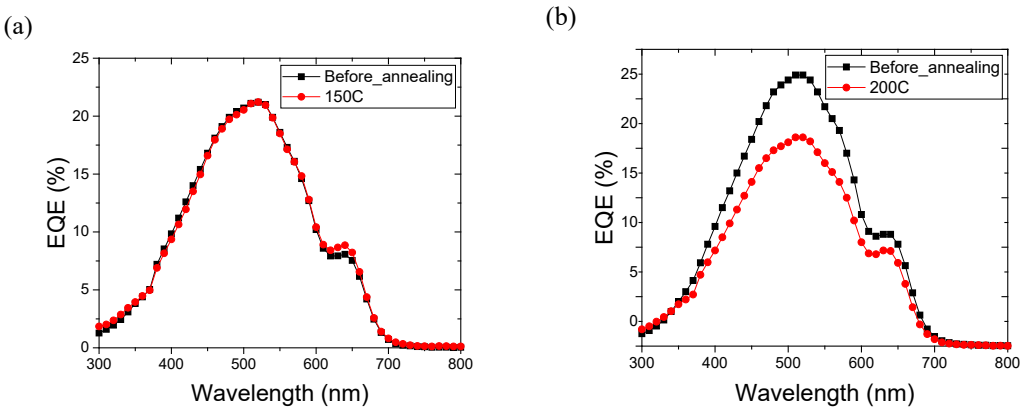

Figure 4.3.10 EQE curves of fabricated reference a-Si:H solar cell before (square) and after (sphere) annealing at 150 ˚C (a) and 200 ˚C (b)

From the EQE curve the optical enhancement (OE) is calculated via Equation 3.2.3 and compared to the simulation result. The result is summarized in Table 4.3.2.

Table 4.3.2. Optical enhancement of measured and simulated plasmonic array enhanced a-Si:H solar cells.

R (nm)	h (nm)	OE (%) Triangular Array Measured	OE (%) Triangular Array Simulated	OE (%) Annealed Array Measured	OE (%) Annealed Array Simulated
500	25	-2.40	-7.87	9.81	4.72
	50	-10.07	-11.40	8.23	7.39
	150	-41.10	-34.24	-24.88	-4.85
1000	25	-8.33	-5.47	1.48	1.88
	50	-13.32	-4.97	-1.51	1.50
	150	-33.72	-9.00	-18.11	-2.51

In general, the measured OE follows the simulated trend: 1) for triangular array, no enhancement is observed and with the increasing of silver thickness the more degradation of the cell; 2) for annealed array, both measured and simulated OE reveal that the enhancement is with the thinner silver thickness. The difference resides in the intensity of the measured OE which is considerably greater than those simulated results. For R = 1000, h = 50nm annealed array, the simulated result shows about 1.5% enhancement, whereas the measured array denies the enhancement. It could possibly because of the degradation during fabrication, which can hardly be removed and may cause fluctuation of the measured OE. In sum, the simulated result will not precisely predict the enhancement, but it will forecast the trend and can be used to guide fabrication.

It is important to compare the electrical performance of the cell in addition to the optical EQE measurement. The characteristic I-V curves are taken for this type of

evaluation. A solar simulator with a calibrated light source is employed to stimulate the AM1.5 irradiance spectrum. Two electrode probes are placed at front and back contact of the cell to form a forward diode configuration. For each measurement the probes are roughly placed at the same place to minimize the discrepancies. Photo current density (J_{sc}), open-circuit voltage (V_{oc}) and fill factor (FF) are determined from the result. I-V characteristic curves for investigated cells are summarized in Figure 4.3.11.

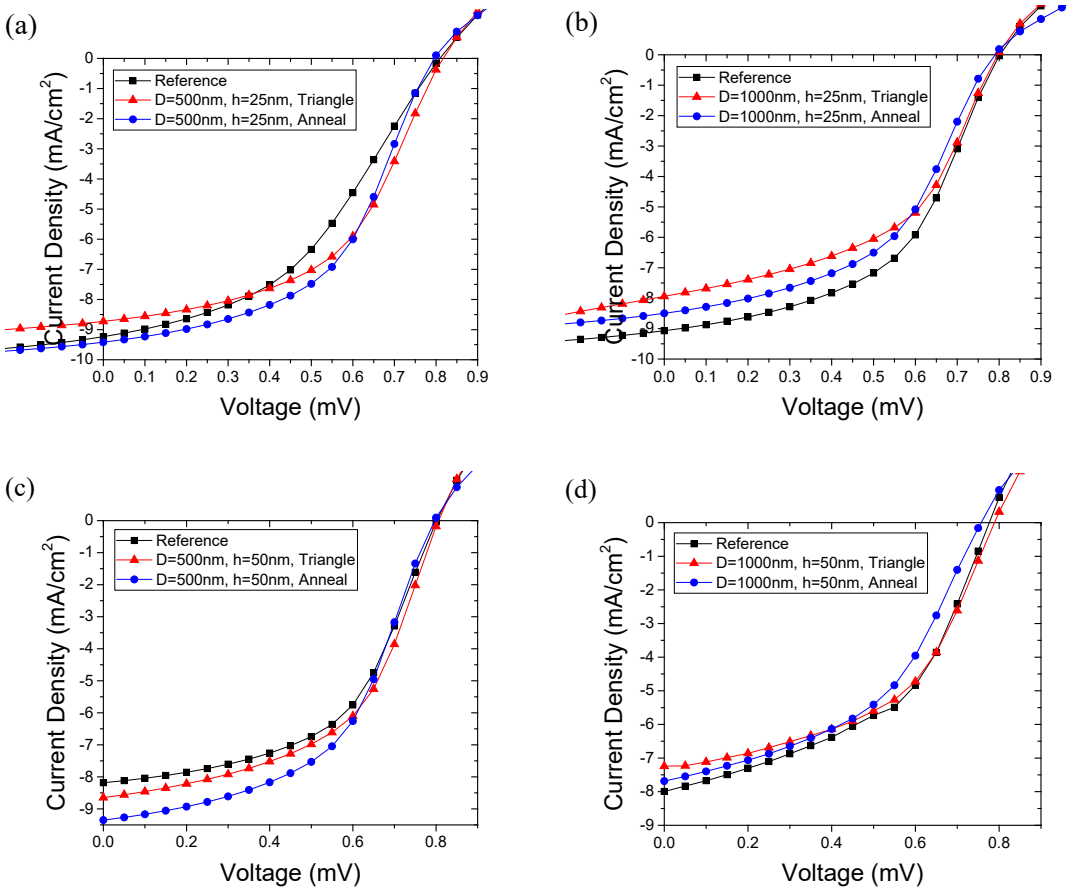

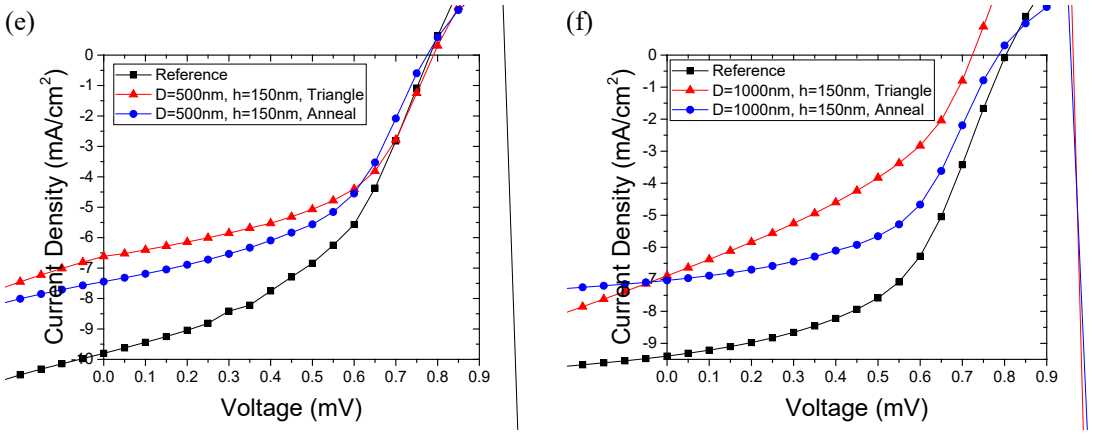

Figure 4.3.11. Characteristic I-V curves of reference (square), triangular (triangle) and annealed (sphere) nanoparticle enhanced a-Si:H solar cell fabricated by NSL mask with beads diameters of 500nm (a, c, e) and 1000nm (b, d, f), deposited silver thickness varies from 25nm to 1000nm as label in legend in each figure.

From Figure 4.3.11, the enhancement in photo-current density is the light trapping indicator. Successfully implemented light trapping scheme should increase the photo-current due to the enhanced absorption rate. Such enhancement can be identified in R = 500nm, h = 25nm and h = 50nm annealed plasmonic array, which goes consistent with the simulation result. More importantly, just as predicted by simulation, the largest photo-current enhancement is with the R = 500nm, h = 50nm annealed sample, J_{sc} enjoys 14.5% enhancement from 8.18 mA/cm^2 to 9.35 mA/cm^2. For h = 25nm annealed array, J_{sc} enhanced 2.05 % compared to the reference cell. For the rest tested sample no observed enhancement in J_{sc}. It is in agreement to the simulation result where the enhancement is observed for annealed array with R = 500, h = 25 and 50nm. Nevertheless, for annealed array with R = 1000nm, h = 25nm and 50nm that are predicted to have enhancement, however the observation disagrees. It can be attributed to the fabrication loss as those enhancement, even in simulation prediction, are not as strong as the R = 500nm cases (only 1% optical enhancement). In addition to fabrication loss, illumination under 1 sun irradiance during the characterization can to some extend deteriorate the performance. This has also been confirmed by the I-V curve of a reference cell sampled

at different illumination period. All h = 150nm samples show significant degradation, it is also in agreement with the simulation and EQE results.

To achieve the successful light trapping in plasmonic enhanced solar cell, the open circuit voltage should preserve in addition to the increased photo-current. The decreasing in V_{oc} after implementing plasmonic nanoparticles are frequently reported[154–156]. In this study no significant deduction of V_{oc} is observed for D = 500nm groups. The cell preserves a constant open circuit voltage at 0.80 V before and after deposition or annealing, same for D = 1000nm, h = 25nm and 50nm groups with the 50nm suffers a slight deterioration after annealing from 0.76 V to 0.71 V. The result indicates no deterioration in electrical performance of the plasmonic cell. Among h = 25nm and 50nm groups, it is also found that the triangle arrays have even slight better V_{oc} in comparison to the annealed ones, which can be attributed to the larger contact area between triangle and ITO, hence better conductivity can be expected. For thicker silver films with large inter-particle spacing the degradation takes place. However there's no foreseen reason for that because thicker silver does not hinder the resistivity, it can possibly be understood that the silver film is too thick that the probe is not actually getting in touch to the ITO, instead it touches the silver nanopillars and hence experience a larger resistance. In sum, except the h = 150nm, R = 1000nm case, overall the V_{oc} is preserved for all tested plasmonic cell sample irrelative to the spacing, thickness or the geometry of the particle, the observation suggests the success in implementing the light trapping using front contact silver nanoparticles.

Table 4.3.3 summarizes the obtained enhancement of *Voc, Jsc* and *FF* of measured a-Si:H cells, and provides a comparison to the simulated result as well. Be noted that the table only summarize the data from cells have been proved to have positive enhancement. Cells that are not giving enhancement are not considered to be useful hence are excluded from the table. The conversion efficiency is computed using the following equation.

$$\eta = \frac{V_{oc} \times J_{sc} \times FF}{P_{inc}} \times 100\% \tag{4.4}$$

Table 4.3.3 Characteristics of two a-Si:H candidates that shows enhancement.

Devices	Voc (V)	Jsc (mA/cm^2)	FF (%)	η (%)	Efficiency Enhancement (%)
Reference	0.81	9.23	61.9	3.17	/
Annealed (D=500nm, h=25nm, measured)	0.8	9.34	67.8	3.81	20.19
Reference	0.8	8.18	68.9	3.5	/
Annealed (D=500nm, h=50nm, measured)	0.8	9.41	68.5	3.88	10.86

The measured overall efficiency is for D = 500nm, h = 25nm is 3.81 in comparison to its reference of 3.17% obtaining 20.2% enhancement in efficiency through the annealed silver particle array, while the D = 500nm, h = 50nm cell has the largest photo-current of 7.69 mA/cm^2 and an overall efficiency of 3.88% in comparison to the its reference of 3.5%, the enhancement it has through the annealed silver particle array is 10.7%. In both cases, the measured optical enhancement is much greater than the predicted enhancement. In the simulation, only scattering and diffraction enhancement is considered. However, in real cell there might be other mechanism that causes the enhancement. For optical enhancement like Febry-Perot effect[31], whispering-gallery wave[157] and waveguide modes[61,109,158] are not identified by the model, hence their contribution is neglected. Besides, non-optical process can also enhance the cell performance, for instance, the deposition of silver particles can result in sheet resistance reduction. Therefore, the enhancement is caused by but not restricted to scattering or diffraction. The other discrepancy is the larger enhancement observed with thinner silver, which is contrary in simulation. Our guess is the deviation of the actual particle shape from sphere and the inaccuracy of the deposition tool thickness monitor, both can result in discrepancies in the measured and simulated result. From

the morphology analysis it could also be inferred that the split smaller particles during annealing yield additional scattering albedos to better cover the cell, therefore the thinner film that produces more split particle can actually have better performance. Nevertheless, experimental analysis is needed to resolve the origin of the observed enhancement.

4.4. Conclusion

In this chapter, the experimental demonstration of validation of the optical enhancement of plasmonic silver nanoparticle array based a-Si:H solar cell is carried out. The fabricated plasmonic silver nanoparticle array and the subsequent annealed array are analysis using a series microscope. Uniform, well-ordered particle array with less defects is obtained and coated onto the cell's front contact. The morphology analysis shows a pseudo-spherical structure in the annealed array, which is more like a bell-shaped hemisphere. Cell performance characterization is completed by EQE and I-V measurement to optically resolve the enhancement and overall device characteristics respectively. In EQE measurement, cell with thinner film thickness and smaller inter-particle spacing shows high performance in the wavelength range of 450-700nm, which is in agreement with the simulated scattering cross-section analysis. This indicates that the excitation of scattered field and guided modes through periodic array are the main source for enhancement. Larger particles, triangular particles are plagued by parasitic absorption hence no observable enhancement ever found. For most of the measured cell the results is consistent with the simulation. Two candidates that show promising enhancement are analyzed in detail. The measured enhancement reach 20.2% and 10.7% for R = 500nm, h = 25nm and 50nm respectively, well-beyond the simulated result. However, the overall cell efficiency is not as good as state-of-art a-Si:H. This is because the quality of fabricated reference cells is not as good as expected. To better understand the discrepancies between measured and simulated result, more experiment validation is required. Nethertheless, our approach is promising to open a route to fabricate plasmonic front contact enhanced a-Si:H solar

cell using inexpensive NSL method, enabling large-scale fabrication that could be possible for commercialization of plasmonic solar devices.

5. Conclusion and future work

This thesis is set out to explore an applicable technique to assist thin-film amorphous silicon (a-Si:H) solar cells to achieve higher energy conversion efficiency and to enable inexpensive, scalable and robust fabrication. With a systematic investigation on a-Si:H solar cell device characteristics, existing light trapping techniques and fabrication methods, the thesis outlines the research to use nanosphere lithography (NSL) as a cheap fabrication technology for plasmonic nanoparticle arrays as the foundation of light trapping in a-Si:H solar cells. Two hypothesis were set up to guide the research for high quality plasmonic structure that delivers maximum enhancement. In the preceding ing Chapters, the over 90% uniform monolayer coating by NSL was implemented on top of silicon, glass and ITO, which addresses the first hypothesis to make quality colloidal mask, the key to access inexpensive plasmonic array, successful. The light trapping mechanism from silver nanoparticle array on top of front contact is investigated and analyzed in detail. Forward scattering and guided modes diffraction provide efficient light trapping within a-Si:H cell's active layers. Finally, the cell is complete using optimized NSL approach and proved to be plasmonic enhanced through characterization. The following paragraph states each of the discovery and recommended future work in detail.

In Chapter 2, two methods of fabricating ordered 2D nanosphere colloidal films are presented: spin coating and interface coating. The novel approaches have been demonstrated to fabricating large colloidal HCP structures using polystyrene beads. Spin coating was found to be the more favorable way of implement coating for smaller (500 nm) beads, while for larger beads there is insufficient water flux compensation during spin coating such that beads stick, preventing large scale monolayer formation. The opposite is true for interface coating; larger beads can be used to attain a monolayer more easily, and even without the help of surfactant, than smaller beads, which are fragile at boundary and have a reduced HCP yield. This difference can be attributed to the surface forces that arise from surface curvature, drawing in nearby beads as the amount of beads increases. Spin coating the 500nm beads, and interface

coating the 1000 nm beads without SDS each reach around 90% coverage. The success of implemented spin coating and interface coating are based on polystyrene beads with diameter of 500nm and 1000nm, at the time of completion no other types of beads have been tested. In order to demonstrate the extensibility and versatility of the method, beads made of various material such as silica, and of different sizes should also be considered as a necessary supplement to the method.

In Chapter 3. Plasmonic induced light trapping through triangle and sphere silver nano arrays fabricated using NSL techniques have been studied for a-Si:H solar cells. Scattering from the silver triangle and sphere arrays deposited on top of conducting ITO layer produce completely different cross-section profiles. Well-separated resonant modes are identified in triangle arrays, with substantial red-shifts found as the triangle spacing increases. At the same time, the thickness of the silver film tends to overlap two primary resonance peaks into a broad peak when increased to above 200nm. Scattering from higher order modes increases drastically with greater silver thickness, whereas dipole peaks are less affected. Cross-sections in sphere arrays show a continuous, broad peak across the main absorbing spectrum from 300nm to 700nm, and the peaks further extend to infrared as the spheres become larger. The broad scattering cross-section peak observed is a combination of multiple resonance modes that are not well-separated at the UV-visible range. For solar photovoltaic applications, the sphere arrays are more beneficial when generating broad scattering peaks than their simulated triangle array counterparts. The sphere array are found to be advantageous for a-Si:H PV applications for its broad overlapping scattering cross-section to the spectral response a-Si:H cell. The parameters of NSL beads size and silver thickness are optimized to support higher optical enhancement. The best candidates shows a enhancement of 7.4% which has not yet been reported using front contact array. For future works it is worth trying new geometry using similar approach, namely, the NSL. NSL enables creating nanodots, nanopillars and nanorings hexagonal array at low-cost. By changing the substrate or making a stacked mask, one can create non-close packed with different symmetry other than hexagonal. Simulation has shown that a cubic

symmetry favors the plasmonic enhancement more than a hexagonal array[31]. The result of these new structure is interesting enough to be examined as a simulation practice. Moreover, the plasmonic material should not be limited to silver. Gold is generally more absorptive than scattering, however, gold has a flat dielectric function around -2 at long wavelength, and it might be a source of even higher scattering. Aluminum is also shown to have better plasmonic response than silver[159] and it has not been tried with NSL supported arrays. Last, there are other enhancing mechanism that need to be tested in the future, scattering and near field effect may not be the most efficient way to help harvesting energy, nanoparticle diffraction and surface plasmon polariton delivers consideration redirected irradiation back to the cell[63]. How should one engineering the structure to extract more energy within the cell is attractive to researchers. Implementing the NSL at back will at the same time, creates a textured surface in the front contact, which in turns helps the light trapping. There is no doubt the NSL can contribute more through back contact, the question is how it should be implemented to maximize the absorption in i-layer. This needs input and optimization from simulation.

In Chapter 4, the experimental proof-of-concept is implemented and characterized. The enhancement is quantified with external quantum efficiency (EQE) and I-V characterization which resolve the light trapping mechanism in optical and electrical domain. Both EQE measurement and I-V characterization goes compliance with the simulation result: the triangular nanoparticle array and thicker silver film show degradation of cell performance while the annealed particle with smaller thickness and inter-particle spacing obtain certain amount of enhancement. The discrepancies between fabrication and simulated result can be attributed to the difference between the perfect spherical nanoparticle and the real deposited and annealed nanoparticle, as well as the losses during fabrication. The maximum optical enhancement by observation is 9.81% obtained from annealed array with NSL beads diameter of 500nm and silver thickness of 25nm, and the cell efficiency obtained from the I-V curve shows more than 20% enhancement compared to the reference cell. This is also the first time that

the success of implementing a plasmonic front contact with more than 20% efficiency enhancement is reported.

The thesis covers two experiment based studies and one theoretical study that addresses the two hypothesis proposed at the beginning of the thesis. 1) Uniform monolayer coverage over 90% of the surface is achieved by spin coating and interface coating of polystyrene beads on glass, silicon and ITO. 2) Improved photo current density of 9.34 mA/cm^2 is acquired from annealed silver nanoparticle array by extraordinary scattering from 450nm to 700nm via silver nanoparticles, the J_{sc} enhanced from reference's 8.18 mA/cm^2 by a factor of 14.2%. It is believed the front contact plasmonic array enhanced a-Si:H solar cell, fabricated by inexpensive and scalable NSL approach, promises the future a valuable candidate to approach global sustainability.

References

[1] This Month in Physics History, (n.d.). http://www.aps.org/publications/apsnews/200904/physicshistory.cfm (accessed June 16, 2016).

[2] With Asian and U.S. Deployments Rising, IHS Raises Global 2015 Solar PV Forecast to 59 GW | IHS Online Newsroom, (n.d.). http://press.ihs.com/press-release/technology/asian-and-us-deployments-rising-ihs-raises-global-2015-solar-pv-forecast-59 (accessed May 22, 2016).

[3] Data and Statistics - IRENA REsource, (n.d.). http://resourceirena.irena.org/gateway/dashboard/?topic=4&subTopic=18 (accessed June 16, 2016).

[4] Solar PV Market Installed Capacity Will Reach 489.8 GW By 2020: New Report By Grand View Research, Inc., MarketWatch. (n.d.). http://www.marketwatch.com/story/solar-pv-market-installed-capacity-will-reach-4898-gw-by-2020-new-report-by-grand-view-research-inc-2015-03-07 (accessed June 16, 2016).

[5] R.E.I. Schropp, M. Zeman, Amorphous and microcrystalline silicon solar cells: modeling, materials, and device technology, Kluwer Academic, Boston, 1998.

[6] A. Shah, P. Torres, R. Tscharner, N. Wyrsch, H. Keppner, Photovoltaic Technology: The Case for Thin-Film Solar Cells, Science. 285 (1999) 692–698. doi:10.1126/science.285.5428.692.

[7] P. Lechner, H. Schade, Photovoltaic thin-film technology based on hydrogenated amorphous silicon, Prog. Photovolt. Res. Appl. 10 (2002) 85–97. doi:10.1002/pip.412.

[8] D.L. Staebler, C.R. Wronski, Reversible conductivity changes in discharge-produced amorphous Si, Appl. Phys. Lett. 31 (1977) 292–294. doi:10.1063/1.89674.

[9] D.E. Carlson, C.R. Wronski, Amorphous silicon solar cell, Appl. Phys. Lett. 28 (1976) 671. doi:10.1063/1.88617.

[10] Amorphous silicon solar cells, in: Clean Electr. Photovolt., n.d.

[11] C.R. Wronski, J.M. Pearce, R.J. Koval, X. Niu, A.S. Ferlauto, J. Koh, R.W. Collins, Light Induced Defect Creation Kinetics in Thin Film Protocrystalline Silicon Materials and Their Solar Cells, in: Symp. – Amorph. Heterog. Silicon-Based Films-2002, 2002: p. A13.4 (12 pages). doi:10.1557/PROC-715-A13.4.

[12] C.R. Wronski, J.M. Pearce, J. Deng, V. Vlahos, R.W. Collins, Intrinsic and light induced gap states in a-Si:H materials and solar cells—effects of microstructure, Thin Solid Films. 451–452 (2004) 470–475. doi:10.1016/j.tsf.2003.10.129.

[13] J. Deng, J.M. Pearce, R.J. Koval, V. Vlahos, R.W. Collins, C.R. Wronski, Absence of carrier recombination associated with the defect pool model in intrinsic amorphous silicon layers: Evidence from current–voltage characteristics on p–i–n and n–i–p solar cells, Appl. Phys. Lett. 82 (2003) 3023. doi:10.1063/1.1571985.

[14] J.M. Pearce, Photovoltaics — a path to sustainable futures, Futures. 34 (2002) 663–674. doi:10.1016/S0016-3287(02)00008-3.

[15] D.V.P. McLaughlin, J.M. Pearce, Analytical model for the optical functions of indium gallium nitride with application to thin film solar photovoltaic cells, Mater. Sci. Eng. B. 177 (2012) 239–244. doi:10.1016/j.mseb.2011.12.008.

[16] H. Mertens, A.F. Koenderink, A. Polman, Plasmon-enhanced luminescence near noble-metal nanospheres: Comparison of exact theory and an improved Gersten and Nitzan model, Phys. Rev. B. 76 (2007). doi:10.1103/PhysRevB.76.115123.

[17] V. Jovanov, U. Palanchoke, P. Magnus, H. Stiebig, J. Hüpkes, P. Sichanugrist, M. Konagai, S. Wiesendanger, C. Rockstuhl, D. Knipp, Light trapping in periodically textured amorphous silicon thin film solar cells using realistic interface morphologies, Opt. Express. 21 (2013) A595. doi:10.1364/OE.21.00A595.

[18] M. Konagai, Present Status and Future Prospects of Silicon Thin-Film Solar Cells, Jpn. J. Appl. Phys. 50 (2011) 030001. doi:10.1143/JJAP.50.030001.

[19] M. Zeman, R.A.C.M.M. van Swaaij, J.W. Metselaar, R.E.I. Schropp, Optical modeling of a-Si:H solar cells with rough interfaces: Effect of back contact and interface roughness, J. Appl. Phys. 88 (2000) 6436. doi:10.1063/1.1324690.

[20] J. Müller, B. Rech, J. Springer, M. Vanecek, TCO and light trapping in silicon thin film solar cells, Sol. Energy. 77 (2004) 917–930. doi:10.1016/j.solener.2004.03.015.

[21] A. Hongsingthong, T. Krajangsang, B. Janthong, P. Sichanugrist, M. Konagai, Effect of high-haze zinc oxide films fabricated on soda-lime glass substrate for thin-film silicon solar cells, in: IEEE, 2011: pp. 000791–000794. doi:10.1109/PVSC.2011.6186073.

[22] M.A. Green, Solar cells: operating principles, technology, and system applications, Prentice-Hall, 1982.

[23] E. Yablonovitch, G.D. Cody, Intensity enhancement in textured optical sheets for solar cells, IEEE Trans. Electron Devices. 29 (1982) 300–305. doi:10.1109/T-ED.1982.20700.

[24] E. Yablonovitch, Statistical ray optics, J. Opt. Soc. Am. 72 (1982) 899. doi:10.1364/JOSA.72.000899.

[25] S. Nie, Probing Single Molecules and Single Nanoparticles by Surface-Enhanced Raman Scattering, Science. 275 (1997) 1102–1106. doi:10.1126/science.275.5303.1102.

[26] M. Moskovits, Surface-enhanced spectroscopy, Rev. Mod. Phys. 57 (1985) 783–826. doi:10.1103/RevModPhys.57.783.

[27] C.L. Haynes, A.D. McFarland, R.P.V. Duyne, Surface-Enhanced Raman Spectroscopy, Anal. Chem. 77 (2005) 338 A–346 A. doi:10.1021/ac053456d.

[28] C. Li, C. Wu, J. Zheng, J. Lai, C. Zhang, Y. Zhao, LSPR Sensing of Molecular Biothiols Based on Noncoupled Gold Nanorods, Langmuir. 26 (2010) 9130–9135. doi:10.1021/la101285r.

[29] M. Chen, X. Fang, S. Tang, N. Zheng, Polypyrrole nanoparticles for high-performance in vivo near-infrared photothermal cancer therapy, Chem. Commun. 48 (2012) 8934. doi:10.1039/c2cc34463g.

[30] J. Lai, X. Mu, Y. Xu, X. Wu, C. Wu, C. Li, J. Chen, Y. Zhao, Light-responsive nanogated ensemble based on polymer grafted mesoporous silica hybrid nanoparticles, Chem. Commun. 46 (2010) 7370. doi:10.1039/c0cc02914a.

[31] A. Vora, J. Gwamuri, J.M. Pearce, P.L. Bergstrom, D.Ö. Güney, Multi-resonant silver nano-disk patterned thin film hydrogenated amorphous silicon solar cells for Staebler-Wronski effect compensation, J. Appl. Phys. 116 (2014) 093103. doi:10.1063/1.4895099.

[32] J. Gwamuri, D.Ö. Güney, J.M. Pearce, Advances in Plasmonic Light Trapping in Thin-Film Solar Photovoltaic Devices, in: A. Tiwari, R. Boukherroub, heshwar Sharon (Eds.), Sol. Cell Nanotechnol., John Wiley & Sons, Inc., 2013: pp. 241–269. http://onlinelibrary.wiley.com/doi/10.1002/9781118845721.ch10/summary (accessed April 10, 2016).

[33] A. Vora, J. Gwamuri, N. Pala, A. Kulkarni, J.M. Pearce, D.Ö. Güney, Exchanging Ohmic Losses in Metamaterial Absorbers with Useful Optical Absorption for Photovoltaics, Sci. Rep. 4 (2014). doi:10.1038/srep04901.

[34] X. Fan, W. Zheng, D.J. Singh, Light scattering and surface plasmons on small spherical particles, Light Sci. Appl. 3 (2014) e179. doi:10.1038/lsa.2014.60.

[35] M. Born, E. Wolf, Principles of optics: electromagnetic theory of propagation, interference and diffraction of light, 7th expanded ed, Cambridge University Press, Cambridge ; New York, 1999.

[36] P. Matheu, S.H. Lim, D. Derkacs, C. McPheeters, E.T. Yu, Metal and dielectric nanoparticle scattering for improved optical absorption in photovoltaic devices, Appl. Phys. Lett. 93 (2008) 113108. doi:10.1063/1.2957980.

[37] D. Derkacs, S.H. Lim, P. Matheu, W. Mar, E.T. Yu, Improved performance of amorphous silicon solar cells via scattering from surface plasmon polaritons in nearby metallic nanoparticles, Appl. Phys. Lett. 89 (2006) 093103. doi:10.1063/1.2336629.

[38] J. Mertz, Radiative absorption, fluorescence, and scattering of a classical dipole near a lossless interface: a unified description, J. Opt. Soc. Am. B. 17 (2000) 1906. doi:10.1364/JOSAB.17.001906.

[39] K.R. Catchpole, A. Polman, Design principles for particle plasmon enhanced solar cells, Appl. Phys. Lett. 93 (2008) 191113. doi:10.1063/1.3021072.

[40] P.B. Johnson, R.W. Christy, Optical Constants of the Noble Metals, Phys. Rev. B. 6 (1972) 4370–4379. doi:10.1103/PhysRevB.6.4370.

[41] S. Mokkapati, F.J. Beck, A. Polman, K.R. Catchpole, Designing periodic arrays of metal nanoparticles for light-trapping applications in solar cells, Appl. Phys. Lett. 95 (2009) 053115. doi:10.1063/1.3200948.

[42] H.R. Stuart, D.G. Hall, Thermodynamic limit to light trapping in thin planar structures, J. Opt. Soc. Am. A. 14 (1997) 3001. doi:10.1364/JOSAA.14.003001.

[43] H.R. Stuart, D.G. Hall, Enhanced Dipole-Dipole Interaction between Elementary Radiators Near a Surface, Phys. Rev. Lett. 80 (1998) 5663–5666. doi:10.1103/PhysRevLett.80.5663.

[44] A.F. Oskooi, D. Roundy, M. Ibanescu, P. Bermel, J.D. Joannopoulos, S.G. Johnson, Meep: A flexible free-software package for electromagnetic simulations by the FDTD method, Comput. Phys. Commun. 181 (2010) 687–702. doi:10.1016/j.cpc.2009.11.008.

[45] M.R. Gonçalves, Plasmonic nanoparticles: fabrication, simulation and experiments, J. Phys. Appl. Phys. 47 (2014) 213001. doi:10.1088/0022-3727/47/21/213001.

[46] R.A. Pala, J. White, E. Barnard, J. Liu, M.L. Brongersma, Design of Plasmonic Thin-Film Solar Cells with Broadband Absorption Enhancements, Adv. Mater. 21 (2009) 3504–3509. doi:10.1002/adma.200900331.

[47] H. Raether, Surface plasmons: on smooth and rough surfaces and on gratings, Springer, Berlin, 1988.

[48] M.G. Cottam, D.R. Tilley, Introduction to surface and superlattice excitations, 2nd ed, Institute of Physics Pub, Bristol ; Philadelphia, 2005.

[49] P. Berini, Plasmon-polariton waves guided by thin lossy metal films of finite width: Bound modes of symmetric structures, Phys. Rev. B. 61 (2000) 10484–10503. doi:10.1103/PhysRevB.61.10484.

[50] P. Berini, Plasmon-polariton waves guided by thin lossy metal films of finite width: Bound modes of asymmetric structures, Phys. Rev. B. 63 (2001). doi:10.1103/PhysRevB.63.125417.

[51] J. Chen, G.A. Smolyakov, S.R. Brueck, K.J. Malloy, Surface plasmon modes of finite, planar, metal-insulator-metal plasmonic waveguides, Opt. Express. 16 (2008) 14902. doi:10.1364/OE.16.014902.

[52] J.A. Dionne, L.A. Sweatlock, H.A. Atwater, A. Polman, Plasmon slot waveguides: Towards chip-scale propagation with subwavelength-scale localization, Phys. Rev. B. 73 (2006). doi:10.1103/PhysRevB.73.035407.

[53] V.E. Ferry, L.A. Sweatlock, D. Pacifici, H.A. Atwater, Plasmonic Nanostructure Design for Efficient Light Coupling into Solar Cells, Nano Lett. 8 (2008) 4391–4397. doi:10.1021/nl8022548.

[54] V.E. Ferry, M.A. Verschuuren, H.B.T. Li, R.E.I. Schropp, H.A. Atwater, A. Polman, Improved red-response in thin film a-Si:H solar cells with soft-imprinted plasmonic back reflectors, Appl. Phys. Lett. 95 (2009) 183503. doi:10.1063/1.3256187.

[55] H. Tan, R. Santbergen, A.H.M. Smets, M. Zeman, Plasmonic Light Trapping in Thin-film Silicon Solar Cells with Improved Self-Assembled Silver Nanoparticles, Nano Lett. 12 (2012) 4070–4076. doi:10.1021/nl301521z.

[56] X. Chen, B. Jia, J.K. Saha, B. Cai, N. Stokes, Q. Qiao, Y. Wang, Z. Shi, M. Gu, Broadband Enhancement in Thin-Film Amorphous Silicon Solar Cells Enabled by Nucleated Silver Nanoparticles, Nano Lett. 12 (2012) 2187–2192. doi:10.1021/nl203463z.

[57] Z. Yu, A. Raman, S. Fan, Fundamental limit of nanophotonic light trapping in solar cells, Proc. Natl. Acad. Sci. 107 (2010) 17491–17496. doi:10.1073/pnas.1008296107.

[58] J. Bhattacharya, N. Chakravarty, S. Pattnaik, W.D. Slafer, R. Biswas, V.L. Dalal, A photonic-plasmonic structure for enhancing light absorption in thin film solar cells, Appl. Phys. Lett. 99 (2011) 131114. doi:10.1063/1.3641469.

[59] B. Curtin, R. Biswas, V. Dalal, Photonic crystal based back reflectors for light management and enhanced absorption in amorphous silicon solar cells, Appl. Phys. Lett. 95 (2009) 231102. doi:10.1063/1.3269593.

[60] D. Zhou, R. Biswas, Photonic crystal enhanced light-trapping in thin film solar cells, J. Appl. Phys. 103 (2008) 093102. doi:10.1063/1.2908212.

[61] C. Battaglia, C.-M. Hsu, K. Söderström, J. Escarré, F.-J. Haug, M. Charrière, M. Boccard, M. Despeisse, D.T.L. Alexander, M. Cantoni, Y. Cui, C. Ballif, Light Trapping in Solar Cells: Can Periodic Beat Random?, ACS Nano. 6 (2012) 2790–2797. doi:10.1021/nn300287j.

[62] B.P. Rand, P. Peumans, S.R. Forrest, Long-range absorption enhancement in organic tandem thin-film solar cells containing silver nanoclusters, J. Appl. Phys. 96 (2004) 7519. doi:10.1063/1.1812589.

[63] R.B. Konda, R. Mundle, H. Mustafa, O. Bamiduro, A.K. Pradhan, U.N. Roy, Y. Cui, A. Burger, Surface plasmon excitation via Au nanoparticles in n-CdSe⁄p-Si heterojunction diodes, Appl. Phys. Lett. 91 (2007) 191111. doi:10.1063/1.2807277.

[64] C. Hägglund, M. Zäch, G. Petersson, B. Kasemo, Electromagnetic coupling of light into a silicon solar cell by nanodisk plasmons, Appl. Phys. Lett. 92 (2008) 053110. doi:10.1063/1.2840676.

[65] M. Kirkengen, J. Bergli, Y.M. Galperin, Direct generation of charge carriers in c-Si solar cells due to embedded nanoparticles, J. Appl. Phys. 102 (2007) 093713. doi:10.1063/1.2809368.

[66] J.C. Hulteen, R.P.V. Duyne, Nanosphere lithography: A materials general fabrication process for periodic particle array surfaces, J. Vac. Sci. Technol. A. 13 (1995) 1553–1558. doi:10.1116/1.579726.

[67] J.C. Hulteen, D.A. Treichel, M.T. Smith, M.L. Duval, T.R. Jensen, R.P. Van Duyne, Nanosphere Lithography: Size-Tunable Silver Nanoparticle and Surface Cluster Arrays, J. Phys. Chem. B. 103 (1999) 3854–3863. doi:10.1021/jp9904771.

[68] R. Micheletto, H. Fukuda, M. Ohtsu, A Simple Method for the Production of a Two-Dimensional, Ordered Array of Small Latex Particles, Langmuir. 11 (1995) 3333–3336. doi:10.1021/la00009a012.

[69] P. Colson, R. Cloots, C. Henrist, Experimental Design Applied to Spin Coating of 2D Colloidal Crystal Masks: A Relevant Method?, Langmuir. 27 (2011) 12800–12806. doi:10.1021/la202284a.

[70] J. Chen, P. Dong, D. Di, C. Wang, H. Wang, J. Wang, X. Wu, Controllable fabrication of 2D colloidal-crystal films with polystyrene nanospheres of various diameters by spin-coating, Appl. Surf. Sci. 270 (2013) 6–15. doi:10.1016/j.apsusc.2012.11.165.

[71] Y. Zhao, J.S. Marshall, Spin coating of a colloidal suspension, Phys. Fluids 1994-Present. 20 (2008) 043302. doi:10.1063/1.2896601.

[72] N. Denkov, O. Velev, P. Kralchevski, I. Ivanov, H. Yoshimura, K. Nagayama, Mechanism of formation of two-dimensional crystals from latex particles on substrates, Langmuir. 8 (1992) 3183–3190. doi:10.1021/la00048a054.

[73] A. Kosiorek, W. Kandulski, H. Glaczynska, M. Giersig, Fabrication of Nanoscale Rings, Dots, and Rods by Combining Shadow Nanosphere Lithography and Annealed Polystyrene Nanosphere Masks, Small. 1 (2005) 439–444. doi:10.1002/smll.200400099.

[74] A. Mihi, M. Ocaña, H. Míguez, Oriented Colloidal-Crystal Thin Films by Spin-Coating Microspheres Dispersed in Volatile Media, Adv. Mater. 18 (2006) 2244–2249. doi:10.1002/adma.200600555.

[75] P.-Y. Chen, H.-H. Hsiao, C.-I. Ho, C.-C. Ho, W.-L. Lee, H.-C. Chang, S.-C. Lee, J.-Z. Chen, I.-C. Cheng, Periodic anti-ring back reflectors for hydrogenated amorphous silicon thin-film solar cells, Opt. Express. 22 (2014) A1128. doi:10.1364/OE.22.0A1128.

[76] A. Horrer, C. Schäfer, K. Broch, D.A. Gollmer, J. Rogalski, J. Fulmes, D. Zhang, A.J. Meixner, F. Schreiber, D.P. Kern, M. Fleischer, Parallel Fabrication of Plasmonic Nanocone Sensing Arrays, Small. 9 (2013) 3987–3992. doi:10.1002/smll.201300449.

[77] H.A. Atwater, A. Polman, Plasmonics for improved photovoltaic devices, Nat. Mater. 9 (2010) 205–213. doi:10.1038/nmat2629.

[78] L. Johnson, D.A. Walsh, Deposition of silver nanobowl arrays using polystyrene nanospheres both as reagents and as the templating material, J. Mater. Chem. 21 (2011) 7555–7558. doi:10.1039/C1JM00043H.

[79] C.L. Cheung, R.J. Nikolić, C.E. Reinhardt, T.F. Wang, Fabrication of nanopillars by nanosphere lithography, Nanotechnology. 17 (2006) 1339–1343. doi:10.1088/0957-4484/17/5/028.

[80] T. Ogi, L.B. Modesto-Lopez, F. Iskandar, K. Okuyama, Fabrication of a large area monolayer of silica particles on a sapphire substrate by a spin coating method, Colloids Surf. Physicochem. Eng. Asp. 297 (2007) 71–78. doi:10.1016/j.colsurfa.2006.10.027.

[81] C.-W. Kuo, J.-Y. Shiu, Y.-H. Cho, P. Chen, Fabrication of Large-Area Periodic Nanopillar Arrays for Nanoimprint Lithography Using Polymer Colloid Masks, Adv. Mater. 15 (2003) 1065–1068. doi:10.1002/adma.200304824.

[82] C.-W. Kuo, J.-Y. Shiu, P. Chen, Size- and Shape-Controlled Fabrication of Large-Area Periodic Nanopillar Arrays, Chem. Mater. 15 (2003) 2917–2920. doi:10.1021/cm0343249.

[83] N. Vogel, L. de Viguerie, U. Jonas, C.K. Weiss, K. Landfester, Wafer-Scale Fabrication of Ordered Binary Colloidal Monolayers with Adjustable Stoichiometries, Adv. Funct. Mater. 21 (2011) 3064–3073. doi:10.1002/adfm.201100414.

[84] P. Jiang, M.J. McFarland, Wafer-Scale Periodic Nanohole Arrays Templated from Two-Dimensional Nonclose-Packed Colloidal Crystals, J. Am. Chem. Soc. 127 (2005) 3710–3711. doi:10.1021/ja042789+.

[85] N. Vogel, S. Goerres, K. Landfester, C.K. Weiss, A Convenient Method to Produce Close- and Non-close-Packed Monolayers using Direct Assembly at the Air–Water Interface and Subsequent Plasma-Induced Size Reduction, Macromol. Chem. Phys. 212 (2011) 1719–1734. doi:10.1002/macp.201100187.

[86] W. RUAN, Z. LÜ, N. JI, C. WANG, B. ZHAO, J. ZHANG, Facile Fabrication of Large Area Polystyrene Colloidal Crystal Monolayer via Surfactant-free Langmuir-Blodgett Technique, Chem. Res. Chin. Univ. 23 (2007) 712–714. doi:10.1016/S1005-9040(07)60155-X.

[87] P. Colson, C. Henrist, R. Cloots, Nanosphere Lithography: A Powerful Method for the Controlled Manufacturing of Nanomaterials, J. Nanomater. 2013 (2013) e948510. doi:10.1155/2013/948510.

[88] S. Middleman, The effect of induced air-flow on the spin coating of viscous liquids, J. Appl. Phys. 62 (1987) 2530–2532. doi:10.1063/1.339465.

[89] M. Retsch, Z. Zhou, S. Rivera, M. Kappl, X.S. Zhao, U. Jonas, Q. Li, Fabrication of Large-Area, Transferable Colloidal Monolayers Utilizing Self-Assembly at the Air/Water Interface, Macromol. Chem. Phys. 210 (2009) 230–241. doi:10.1002/macp.200800484.

[90] P.I. Stavroulakis, N. Christou, D. Bagnall, Improved deposition of large scale ordered nanosphere monolayers via liquid surface self-assembly, Mater. Sci. Eng. B. 165 (2009) 186–189. doi:10.1016/j.mseb.2009.09.005.

[91] S. Reynaert, P. Moldenaers, J. Vermant, Control over Colloidal Aggregation in Monolayers of Latex Particles at the Oil−Water Interface, Langmuir. 22 (2006) 4936–4945. doi:10.1021/la060052n.

[92] B. Wijnen, E.J. Hunt, G.C. Anzalone, J.M. Pearce, Open-Source Syringe Pump Library, PLoS ONE. 9 (2014) e107216. doi:10.1371/journal.pone.0107216.

[93] J.M. Pearce, Building Research Equipment with Free, Open-Source Hardware, Science. 337 (2012) 1303–1304. doi:10.1126/science.1228183.

[94] J. Pearce, Open-source lab: how to build your own hardware and reduce research costs, Elsevier, Amsterdam ; Boston, 2013.

[95] A.V. Shah, H. Schade, M. Vanecek, J. Meier, E. Vallat-Sauvain, N. Wyrsch, U. Kroll, C. Droz, J. Bailat, Thin-film silicon solar cell technology, Prog. Photovolt. Res. Appl. 12 (2004) 113–142. doi:10.1002/pip.533.

[96] D.E. Carlson, Hydrogenated microvoids and light-induced degradation of amorphous-silicon solar cells, Appl. Phys. Solids Surf. 41 (1986) 305–309. doi:10.1007/BF00616053.

[97] R.S. Crandall, Defect relaxation in amorphous silicon: Stretched exponentials, the Meyer-Neldel rule, and the Staebler-Wronski effect, Phys. Rev. B. 43 (1991) 4057–4070. doi:10.1103/PhysRevB.43.4057.

[98] H.W. Deckman, Optically enhanced amorphous silicon solar cells, Appl. Phys. Lett. 42 (1983) 968. doi:10.1063/1.93817.

[99] V.E. Ferry, M.A. Verschuuren, H.B.T. Li, E. Verhagen, R.J. Walters, R.E.I. Schropp, H.A. Atwater, A. Polman, Plasmonic light trapping for thin film A-SI:H solar cells, in: 2010 35th IEEE Photovolt. Spec. Conf. PVSC, 2010: pp. 000760–000765. doi:10.1109/PVSC.2010.5617101.

[100] P. Spinelli, V.E. Ferry, J. van de Groep, M. van Lare, M.A. Verschuuren, R.E.I. Schropp, H.A. Atwater, A. Polman, Plasmonic light trapping in thin-film Si solar cells, J. Opt. 14 (2012) 024002. doi:10.1088/2040-8978/14/2/024002.

[101] R.W. Collins, A.S. Ferlauto, G.M. Ferreira, C. Chen, J. Koh, R.J. Koval, Y. Lee, J.M. Pearce, C.R. Wronski, Evolution of microstructure and phase in amorphous, protocrystalline, and microcrystalline silicon studied by real time spectroscopic ellipsometry, Sol. Energy Mater. Sol. Cells. 78 (2003) 143–180. doi:10.1016/S0927-0248(02)00436-1.

[102] R.J. Koval, J.M. Pearce, A.S. Ferlauto, R.W. Collins, C.R. Wronski, The role of phase transitions between amorphous and microcrystalline silicon on the performance of protocrystalline Si:H solar cells, in: IEEE, 2000: pp. 750–753. doi:10.1109/PVSC.2000.915992.

[103] H.R. Stuart, D.G. Hall, Island size effects in nanoparticle-enhanced photodetectors, Appl. Phys. Lett. 73 (1998) 3815. doi:10.1063/1.122903.

[104] D.M. Schaadt, B. Feng, E.T. Yu, Enhanced semiconductor optical absorption via surface plasmon excitation in metal nanoparticles, Appl. Phys. Lett. 86 (2005) 063106. doi:10.1063/1.1855423.

[105] K. Nakayama, K. Tanabe, H.A. Atwater, Plasmonic nanoparticle enhanced light absorption in GaAs solar cells, Appl. Phys. Lett. 93 (2008) 121904. doi:10.1063/1.2988288.

[106] J. Gwamuri, M. Marikkannan, J. Mayandi, P. Bowen, J. Pearce, Influence of Oxygen Concentration on the Performance of Ultra-Thin RF Magnetron Sputter Deposited Indium Tin Oxide Films as a Top Electrode for Photovoltaic Devices, Materials. 9 (2016) 63. doi:10.3390/ma9010063.

[107] J. Gwamuri, A. Vora, R.R. Khanal, A.B. Phillips, M.J. Heben, D.O. Guney, P. Bergstrom, A. Kulkarni, J.M. Pearce, Limitations of ultra-thin transparent conducting oxides for integration into plasmonic-enhanced thin-film solar photovoltaic devices, Mater. Renew. Sustain. Energy. 4 (2015). doi:10.1007/s40243-015-0055-8.

[108] C.L. Haynes, R.P. Van Duyne, Nanosphere Lithography: A Versatile Nanofabrication Tool for Studies of Size-Dependent Nanoparticle Optics, J. Phys. Chem. B. 105 (2001) 5599–5611. doi:10.1021/jp010657m.

[109] C. Langhammer, Z. Yuan, I. Zorić, B. Kasemo, Plasmonic Properties of Supported Pt and Pd Nanostructures, Nano Lett. 6 (2006) 833–838. doi:10.1021/nl060219x.

[110] C. Langhammer, M. Schwind, B. Kasemo, I. Zorić, Localized Surface Plasmon Resonances in Aluminum Nanodisks, Nano Lett. 8 (2008) 1461–1471. doi:10.1021/nl080453i.

[111] E.M. Larsson, J. Alegret, M. Käll, D.S. Sutherland, Sensing Characteristics of NIR Localized Surface Plasmon Resonances in Gold Nanorings for Application as Ultrasensitive Biosensors, Nano Lett. 7 (2007) 1256–1263. doi:10.1021/nl0701612.

[112] R. Morarescu, H. Shen, R.A.L. Vallée, B. Maes, B. Kolaric, P. Damman, Exploiting the localized surface plasmon modes in gold triangular nanoparticles for sensing applications, J. Mater. Chem. 22 (2012) 11537. doi:10.1039/c2jm30944k.

[113] C. Pahud, V. Savu, M. Klein, O. Vazquez-Mena, F. Haug, J. Brugger, C. Ballif, Stencil-Nanopatterned Back Reflectors for Thin-Film Amorphous Silicon n-i-p Solar Cells, IEEE J. Photovolt. 3 (2013) 22–26. doi:10.1109/JPHOTOV.2012.2213583.

[114] G. Tagliabue, H. Eghlidi, D. Poulikakos, Facile multifunctional plasmonic sunlight harvesting with tapered triangle nanopatterning of thin films, Nanoscale. 5 (2013) 9957–9962. doi:10.1039/C3NR03273F.

[115] C.F. Bohren, D.R. Huffman, eds., Absorption and Scattering of Light by Small Particles, Wiley-VCH Verlag GmbH, Weinheim, Germany, 1998. http://doi.wiley.com/10.1002/9783527618156 (accessed June 1, 2016).

[116] Y.A. Akimov, W.S. Koh, K. Ostrikov, Enhancement of optical absorption in thin-film solar cells through the excitation of higher-order nanoparticle plasmon modes, Opt. Express. 17 (2009) 10195. doi:10.1364/OE.17.010195.

[117] T.H. Besseling, M. Hermes, A. Fortini, M. Dijkstra, A. Imhof, A. van Blaaderen, Oscillatory shear-induced 3D crystalline order in colloidal hard-sphere fluids, Soft Matter. 8 (2012) 6931–6939. doi:10.1039/C2SM07156H.

[118] X. Yan, J. Yao, G. Lu, X. Li, J. Zhang, K. Han, B. Yang, Fabrication of Non-Close-Packed Arrays of Colloidal Spheres by Soft Lithography, J. Am. Chem. Soc. 127 (2005) 7688–7689. doi:10.1021/ja0428208.

[119] S. Babar, J.H. Weaver, Optical constants of Cu, Ag, and Au revisited, Appl. Opt. 54 (2015) 477. doi:10.1364/AO.54.000477.

[120] Daryl Myers, Keith Emery, Chris Gueymard, Revising and Validating Spectral Irradiance Standards for Photovoltaic Performance, (2002). doi:10.13140/2.1.3050.0487.

[121] C. Langhammer, B. Kasemo, I. Zorić, Absorption and scattering of light by Pt, Pd, Ag, and Au nanodisks: Absolute cross sections and branching ratios, J. Chem. Phys. 126 (2007) 194702. doi:10.1063/1.2734550.

[122] B. Luk'yanchuk, N.I. Zheludev, S.A. Maier, N.J. Halas, P. Nordlander, H. Giessen, C.T. Chong, The Fano resonance in plasmonic nanostructures and metamaterials, Nat. Mater. 9 (2010) 707–715. doi:10.1038/nmat2810.

[123] M. Futamata, Y. Maruyama, M. Ishikawa, Local Electric Field and Scattering Cross Section of Ag Nanoparticles under Surface Plasmon Resonance by Finite Difference Time Domain Method, J. Phys. Chem. B. 107 (2003) 7607–7617. doi:10.1021/jp022399e.

[124] U. Herr, B. Kuerbanjiang, C. Benel, G. Papageorgiou, M. Goncalves, J. Boneberg, P. Leiderer, P. Ziemann, P. Marek, H. Hahn, Near-field effects and energy transfer in hybrid metal-oxide nanostructures, Beilstein J. Nanotechnol. 4 (2013) 306–317. doi:10.3762/bjnano.4.34.

[125] J. Butet, P.-F. Brevet, O.J.F. Martin, Optical Second Harmonic Generation in Plasmonic Nanostructures: From Fundamental Principles to Advanced Applications, ACS Nano. 9 (2015) 10545–10562. doi:10.1021/acsnano.5b04373.

[126] M. A. van der Veen, G. Rosolen, T. Verbiest, M.K. Vanbel, B. Maes, B. Kolaric, Nonlinear optical enhancement caused by a higher order multipole mode of metallic triangles, J Mater Chem C. 3 (2015) 1576–1581. doi:10.1039/C4TC02427C.

[127] L.J. Sherry, R. Jin, C.A. Mirkin, G.C. Schatz, R.P. Van Duyne, Localized Surface Plasmon Resonance Spectroscopy of Single Silver Triangular Nanoprisms, Nano Lett. 6 (2006) 2060–2065. doi:10.1021/nl061286u.

[128] Y. Fang, B.M. Phillips, K. Askar, B. Choi, P. Jiang, B. Jiang, Scalable bottom-up fabrication of colloidal photonic crystals and periodic plasmonic nanostructures, J. Mater. Chem. C. 1 (2013) 6031. doi:10.1039/c3tc30740a.

[129] J.P. Hoogenboom, C. Rétif, E. de Bres, M. van de Boer, A.K. van Langen-Suurling, J. Romijn, A. van Blaaderen, Template-Induced Growth of Close-Packed and Non-Close-Packed Colloidal Crystals during Solvent Evaporation, Nano Lett. 4 (2004) 205–208. doi:10.1021/nl034867h.

[130] P. Campbell, M.A. Green, The limiting efficiency of silicon solar cells under concentrated sunlight, IEEE Trans. Electron Devices. 33 (1986) 234–239. doi:10.1109/T-ED.1986.22472.

[131] O. Kluth, B. Rech, L. Houben, S. Wieder, G. Schöpe, C. Beneking, H. Wagner, A. Löffl, H.. Schock, Texture etched ZnO:Al coated glass substrates for silicon based thin film solar cells, Thin Solid Films. 351 (1999) 247–253. doi:10.1016/S0040-6090(99)00085-1.

[132] S. Faÿ, J. Steinhauser, S. Nicolay, C. Ballif, Polycrystalline ZnO: B grown by LPCVD as TCO for thin film silicon solar cells, Thin Solid Films. 518 (2010) 2961–2966. doi:10.1016/j.tsf.2009.09.189.

[133] S. Guha, J. Yang, Progress in amorphous and nanocrystalline silicon solar cells, J. Non-Cryst. Solids. 352 (2006) 1917–1921. doi:10.1016/j.jnoncrysol.2006.01.048.

[134] M.A. Green, K. Emery, Y. Hishikawa, W. Warta, E.D. Dunlop, Solar cell efficiency tables (version 47): Solar cell efficiency tables, Prog. Photovolt. Res. Appl. 24 (2016) 3–11. doi:10.1002/pip.2728.

[135] Benagli, S., Borrello, D., Vallat-Sauvain, E., Meier, J., Kroll, U., Hötzel, J., Bailat, J., Steinhauser, J., Marmelo, M., Monteduro, G., Castens, L., High-Efficiency Amorphous Silicon Devices on LPCVD-ZnO TCO Prepared in Industrial KAI TM-M R&D Reactor, (2009). doi:10.4229/24thEUPVSEC2009-3BO.9.3.

[136] V.E. Ferry, J.N. Munday, H.A. Atwater, Design Considerations for Plasmonic Photovoltaics, Adv. Mater. 22 (2010) 4794–4808. doi:10.1002/adma.201000488.

[137] V.E. Ferry, M.A. Verschuuren, M.C. van Lare, R.E.I. Schropp, H.A. Atwater, A. Polman, Optimized Spatial Correlations for Broadband Light Trapping Nanopatterns in High Efficiency Ultrathin Film a-Si:H Solar Cells, Nano Lett. 11 (2011) 4239–4245. doi:10.1021/nl202226r.

[138] J. Zhu, C.-M. Hsu, Z. Yu, S. Fan, Y. Cui, Nanodome Solar Cells with Efficient Light Management and Self-Cleaning, Nano Lett. 10 (2010) 1979–1984. doi:10.1021/nl9034237.

[139] M.G. Deceglie, V.E. Ferry, A.P. Alivisatos, H.A. Atwater, Accounting for Localized Defects in the Optoelectronic Design of Thin-Film Solar Cells, IEEE J. Photovolt. 3 (2013) 599–604. doi:10.1109/JPHOTOV.2013.2240764.

[140] C.-M. Hsu, C. Battaglia, C. Pahud, Z. Ruan, F.-J. Haug, S. Fan, C. Ballif, Y. Cui, High-Efficiency Amorphous Silicon Solar Cell on a Periodic Nanocone Back Reflector, Adv. Energy Mater. 2 (2012) 628–633. doi:10.1002/aenm.201100514.

[141] H.B.T. Li, R.H. Franken, J.K. Rath, R.E.I. Schropp, Structural defects caused by a rough substrate and their influence on the performance of hydrogenated nano-crystalline silicon n–i–p solar cells, Sol. Energy Mater. Sol. Cells. 93 (2009) 338–349. doi:10.1016/j.solmat.2008.11.013.

[142] S.H. Lim, W. Mar, P. Matheu, D. Derkacs, E.T. Yu, Photocurrent spectroscopy of optical absorption enhancement in silicon photodiodes via scattering from surface plasmon polaritons in gold nanoparticles, J. Appl. Phys. 101 (2007) 104309. doi:10.1063/1.2733649.

[143] D. Wang, G. Su, New strategy to promote conversion efficiency using high-index nanostructures in thin-film solar cells, Sci. Rep. 4 (2014). doi:10.1038/srep07165.

[144] K. Söderström, J. Escarré, O. Cubero, F.-J. Haug, S. Perregaux, C. Ballif, UV-nano-imprint lithography technique for the replication of back reflectors for n-i-p thin film silicon solar cells, Prog. Photovolt. Res. Appl. 19 (2011) 202–210. doi:10.1002/pip.1003.

[145] A. Hohenau, H. Ditlbacher, B. Lamprecht, J.R. Krenn, A. Leitner, F.R. Aussenegg, Electron beam lithography, a helpful tool for nanooptics, Microelectron. Eng. 83 (2006) 1464–1467. doi:10.1016/j.mee.2006.01.085.

[146] W. Rechberger, A. Hohenau, A. Leitner, J.R. Krenn, B. Lamprecht, F.R. Aussenegg, Optical properties of two interacting gold nanoparticles, Opt. Commun. 220 (2003) 137–141. doi:10.1016/S0030-4018(03)01357-9.

[147] J.A. Veerman, A.M. Otter, L. Kuipers, N.F. van Hulst, High definition aperture probes for near-field optical microscopy fabricated by focused ion beam milling, Appl. Phys. Lett. 72 (1998) 3115. doi:10.1063/1.121564.

[148] H.J. Lezec, Beaming Light from a Subwavelength Aperture, Science. 297 (2002) 820–822. doi:10.1126/science.1071895.

[149] T.H. Taminiau, F.B. Segerink, R.J. Moerland, L. (Kobus) Kuipers, N.F. van Hulst, Near-field driving of a optical monopole antenna, J. Opt. Pure Appl. Opt. 9 (2007) S315–S321. doi:10.1088/1464-4258/9/9/S06.

[150] L. Karki Gautam, M. Junda, H. Haneef, R. Collins, N. Podraza, Spectroscopic Ellipsometry Studies of n-i-p Hydrogenated Amorphous Silicon Based Photovoltaic Devices, Materials. 9 (2016) 128. doi:10.3390/ma9030128.

[151] C.R. Wrongski, D.E. Carlson, Amorphous silicon solar cells, in: Clean Electr. Photovolt., Imperial College Press, 199, 2001.

[152] M. Berginski, J. Hüpkes, M. Schulte, G. Schöpe, H. Stiebig, B. Rech, M. Wuttig, The effect of front ZnO:Al surface texture and optical transparency on efficient light trapping in silicon thin-film solar cells, J. Appl. Phys. 101 (2007) 074903. doi:10.1063/1.2715554.

[153] S.J. Oldenburg, G.D. Hale, J.B. Jackson, N.J. Halas, Light scattering from dipole and quadrupole nanoshell antennas, Appl. Phys. Lett. 75 (1999) 1063. doi:10.1063/1.124597.

[154] E. Moulin, J. Sukmanowski, M. Schulte, A. Gordijn, F.X. Royer, H. Stiebig, Thin-film silicon solar cells with integrated silver nanoparticles, Thin Solid Films. 516 (2008) 6813–6817. doi:10.1016/j.tsf.2007.12.018.

[155] C. Eminian, F.-J. Haug, O. Cubero, X. Niquille, C. Ballif, Photocurrent enhancement in thin film amorphous silicon solar cells with silver nanoparticles, Prog. Photovolt. Res. Appl. 19 (2011) 260–265. doi:10.1002/pip.1015.

[156] J. Chantana, Y. Yang, Y. Sobajima, C. Sada, A. Matsuda, H. Okamoto, Localized surface plasmon enhanced microcrystalline–silicon solar cells, J. Non-Cryst. Solids. 358 (2012) 2319–2323. doi:10.1016/j.jnoncrysol.2011.12.038.

[157] J. Grandidier, D.M. Callahan, J.N. Munday, H.A. Atwater, Light Absorption Enhancement in Thin-Film Solar Cells Using Whispering Gallery Modes in Dielectric Nanospheres, Adv. Mater. 23 (2011) 1272–1276. doi:10.1002/adma.201004393.

[158] J. Trevino, C. Forestiere, G. Di Martino, S. Yerci, F. Priolo, L. Dal Negro, Plasmonic-photonic arrays with aperiodic spiral order for ultra-thin film solar cells, Opt. Express. 20 (2012) A418. doi:10.1364/OE.20.00A418.

[159] M.A. Green, S. Pillai, Harnessing plasmonics for solar cells, Nat. Photonics. 6 (2012) 130–132. doi:10.1038/nphoton.2012.30.